**Title**

Non-Diffusive Heat Conduction in Small Length and Short Time Scale



**Author**

Yang, Fan

**Publication Date**

2014

Peer reviewed|Thesis/dissertation

# Non-Diffusive Heat Conduction in Small Length and Short Time Scale

by

Fan Yang

A dissertation submitted in partial satisfaction of the

requirements for the degree of

Doctor of Philosophy

in

Engineering – Mechanical Engineering

in the

Graduate Division

of the

University of California, Berkeley

Committee in charge:

Professor Christopher Dames, Chair
Professor Xiang Zhang
Professor Andrew Minor

Fall 2014

Non-Diffusive Heat Conduction
in Small Length and Short Time Scale



by

Fan Yang

Abstract

Non-Diffusive Heat Conduction
in Small Length and Short Time Scale

by

Fan Yang

Doctor of Philosophy in Engineering – Mechanical Engineering

University of California, Berkeley

Professor Christopher Dames, Chair

With the evolution of semiconductor technology toward nanometer size and gigahertz frequency, the traditional diffusive Fourier's law of heat conduction can no longer be applied. To engineer new methods for chip cooling or thermoelectric power generation, understanding the non-diffusive heat transfer in both the length and time domains is important. In this dissertation, the phonon transport at nanometer lengths or gigahertz heating frequencies is investigated using the Boltzmann Transport Equation (BTE).

Regarding length scale effects, a systematic theory of the phonon thermal conductivity accumulation function was developed to show which phonon mean free paths are important for heat transfer. I show that the nanostructure thermal conductivity can be obtained with only the bulk mean free path spectrum and nanostructure geometry as independent inputs. This theory has been applied to nanowire and in-plane thin film systems. In addition, the length scale effect on the effective conductivity in randomly oriented superlattice polycrystals, which are potential thermoelectric materials, has also been investigated.

Regarding time scale effects, I derived an analytical solution to the BTE under the gray mean free time assumption, and extended the solution to the non-gray regime. With this theory, I can explain the experiments measuring a heating frequency dependent thermal conductivity of semiconductor alloys. I also build up a framework which can be used to extract a phonon accumulation function with respected to mean free time. The similarities and differences of both length and time effects have also been compared and discussed.

**Dedicated to Qianyi**

**For the past, present and future**

## Table of Contents

**List of Figures**

**List of Tables**

**Acknowledgements**

Today is the Thanksgiving day. I just close this dissertation and it is the right time giving thanks to advisers, cooperators, families, and all friends during this long journey of my Ph.D.

I was fortunate to work with my dissertation Chair, Prof. Chris Dames. His vision on research topics, critical thinking on the logics, and kindness on every aspects, not only strongly affect me on doing research, but also on my life. His encouragement helped me gained the confidence whenever I encounter difficulties. His saying of "There always has a distribution." and "What's new?" always inspired me to explore the unknown scientific world. I would like to thank his continuous support. Without it, it is impossible to get this dissertation done.

I am grateful for the guidance of other committees members of this dissertation Prof. Xiang Zhang and Prof. Andrew Minor, and also other members of my qualifying exam Prof. Costas Grigoropoulos and Prof. Liwei Lin. I also like to thank Prof. Kambiz Vafai, Prof. Javier Garay, Prof. Guanshui Xu, and Prof. Elaine Haberer in UCR for their help and guidance. These years in UCR was also fantastic.

The days in the nano-energy lab in Berkeley are full of fun, enjoyment, and insightful discussions. I'd like to thank all the group members for their help, including but not limit to Shannon Yee, Zhiyong Wei, Bastian Wagg, Zhen Chen, Christian Monachon, Wyatt Hodges, Imran Khan, Jake Kilbane, Sean Lubner, Vivek Mishra, Geoff Wehmeyer, and also other students, postdocs, and visitors. I also like the past members in UCR: John Miller, Zhaojie Wang, Anthony Fong, and Wan Young Jang *et al*. I especially like to thank visiting professor Yasuhiro Hasegawa for teaching me nanofabrication.

Berkeley is a community with a lot of cooperation. I like to thank the help of Dr. Jeff Urban from Molecular Foundry and also his group members including: Ayaskanta Sahu, Jason Forster, Woochul Lee, and Boris Russ in my last year. I'd like to thank Jonathan Pierce and Dr. Rama Venkatasubramanian *et al.* from RTI International providing us thin film samples and Prof. Jeffrey Snyder and Dr. Teruyuki Ikeda from Caltech on nano-grain superlattice project. I also like to thank a lot of other cooperators, such as the members in Junqiao Wu's group in MSE and Hongyun So from mechanical engineering (for porous Si thermal conductivity measurement.).

Most importantly, thank all my families, my parents, my grandparents, my brother, and Qianyi. Thank you all for your love, support, encouragement, and understanding.

# Chapter 1 Background

The energy problem becomes one of the most critical problems nowadays, as the world's population is expected to increase from 7 billion today to 10 billion by 2100[1, 2]. This increase and also the improvement of living standards demand more energy or new technology which has higher efficiency. Waste heat recovery is one very important research area. For instance, for a car only 21.5% of the energy is used to move the car, while more than 30-37% of the energy loss goes to the exhaust gas[2]. Thus, if even only 1% efficiency can be enhanced, the both economic and environmental effect would be enormous. There is a great potential we can harvest the wasted heat energy. Thermoelectrics is one of the most attractive technology nowadays.

With the rapid development of semiconductor technology in the past few decades, there are two main characteristics on both length and time scale. One is that its size become smaller and smaller, as shown in regime two in Fig. 1.1, thus more and more chips on the same area would increases the power density even though the manufacturing cost would decrease. On the other hand, when the clock becomes faster and faster, as shown in regime 3 in Fig. 1.1, more and more power would be consumed in a single transistor. Thus the chips would be hotter and hotter[3]. In addition, in regimes 2 and 3, when the length or time is shorter than the characteristic length or time, ballistic effect would further decrease the thermal transport and reduce the capability to dissipate heat. Thus, this dissertation will mainly focus on the regime of 2 and 3, to understand the fundamentals of how the size and time would affect the thermal transport in the non-diffusive (or ballistic) regime.

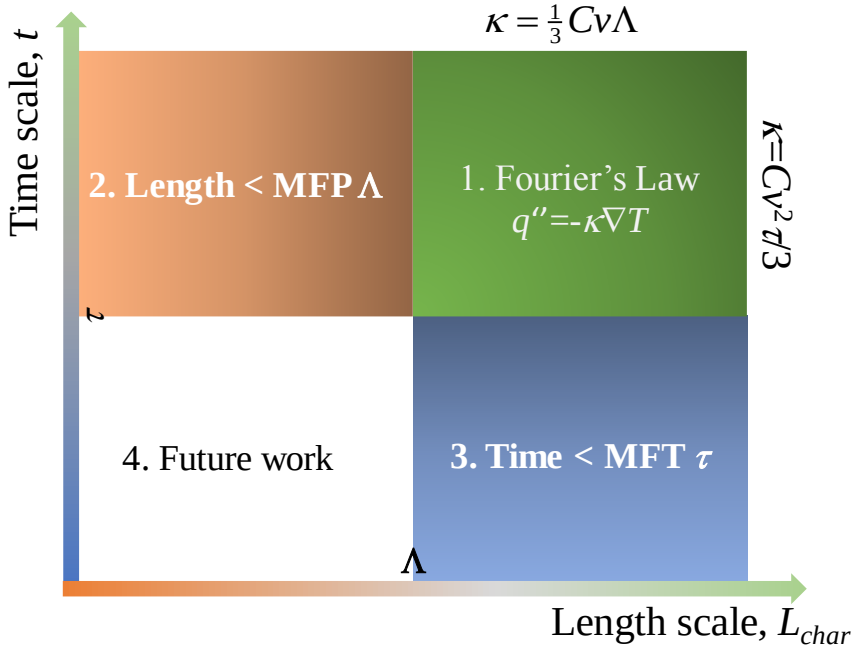


**Figure 1.1 Heat conduction regime map. Our investigation regimes are in 2 and 3.**

## 1.1 Thermoelectrics and the Applications

The thermoelectric power generation device, as shown in Fig. 1.2, has many advantages compared to traditional devices. It uses the thermoelectric effect to directly harvest the heat energy and convert it electricity. There are no mechanical moving parts, which lead to much lower noise and longer lifetime. Since it is a solid state device, there is no pump or compressor. Thus, the device can be made much smaller. In addition, it is made by semiconductor, which can be integrated into modern semiconductor technology naturally. Thus, it has the potential for massive production and cost reduction.

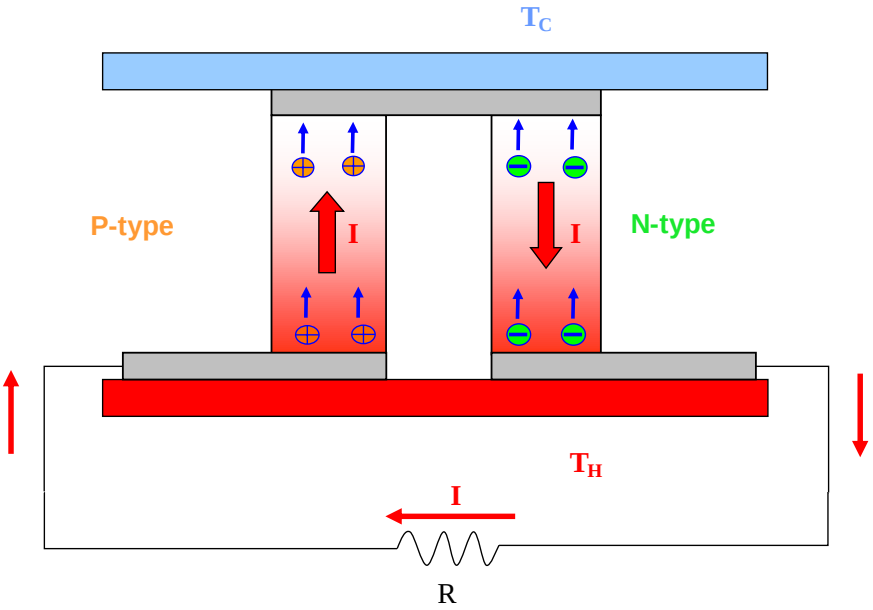


**Figure 1.2 Schematic of thermoelectric power generator. The temperature gradient provides the driving source.**

Even though the thermoelectric energy converter has many advantages, the applications are still not very broad at present. The major reason is the efficiency is still too low. The efficiency of a thermoelectric material, *n*- or *p*-type semiconductor as shown in Fig. 1.2, is determined by the figure of merit $zT$

$$zT = \frac{S^2\sigma}{\kappa_e + \kappa_{ph}} T \qquad (1.1)$$

where $S$ is the Seebeck coefficient, $\sigma$ is the electrical conductivity, $\kappa_e$ is the electrical thermal conductivity, and $\kappa_{ph}$ is the phonon thermal conductivity. The optimized efficiency for the thermoelectric module is[4]

$$\eta_{\max} = \eta_{Carnot} \frac{\sqrt{1+zT} - 1}{\sqrt{1+zT} + T_C / T_H} \qquad (1.2)$$

where $\eta_{Carnot} = \frac{T_H - T_C}{T_H}$ is the efficiency of the Carnot cycle, where $T_H$ is the high temperature and $T_c$ is the low temperature of the device. Figure 1.3 shows the

relationship between a $zT$ value and $\eta_{max}$ in Eq.(1.2). Usually, considering cost of other power generation technologies, it requires the $zT > 3$ to make thermoelectrics competitive with them.

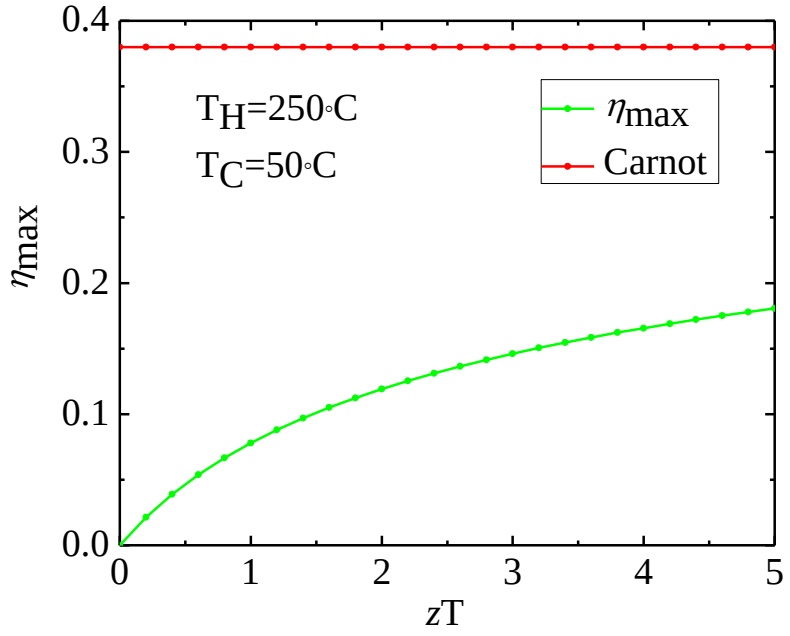


**Figure 1.3 Carnot efficiency and efficiency of thermoelectrics at different $zT$**

In the past two decades, the field of thermoelectrics gain much attention. In the early 1990s, Hicks and Dresselhaus[5-7] proposed that nanotechnology is one efficient way to enhance the $zT$. The proposal uses quantum confinement effects, which would provide a larger density of state gradient, thus improve the Seebeck coefficient to achieve high $zT$. A few years later, researchers found reducing the thermal conductivity is even more effective than enhancing the Seebeck effect. Thus, reducing thermal conductivity has gain a lot of attention.

Different methods have been used to reduce the lattice thermal conductivity. Venkatasubramanian *et al.*[8] use the superlattice made by *p*-type $Bi_2Te_3/Sb_2Te_3$ and achieved $zT$ = 2.2 in their device at room temperature. Doping with heavy rare earth materials, which provide extra impurity scattering is also an effective way to reduce the thermal conductivity in InGaAs. Kim *et al.*[9] use ErAs doping, and reduced the thermal conductivity a factor of 2 even below the alloy limit.

On the nanostructure side, nanowire provides very effective way to confine the phonon mean free path. It has been used on Si nanowire[10, 11], which reduce the thermal conductivity more than one order of magnitude with the reduction of the wire diameter. The phonon boundary scattering is the most important scattering mechanism in these nanowires. Hochbaum *et al.*[12] use the aqueous electroless etching method to make even rougher nanowire and reduce the thermal conductivity more than two order of

magnitude comparing to the bulk thermal conductivity at room temperature. Similar work on silicon nanowires has also been published at the same time by Boukai *et al.*[13]. To further reduce the thermal conductivity and understand the scattering mechanism of nanowire, especially the role of surface roughness, Kedar *et al.*[14, 15] made even rougher nanowires and investigated the relationship between the thermal conductivity and roughness power spectra.

For bulk and larger scale energy harvesting, bulk materials are more desirable. Poudel *et al.*[16] found the bismuth antimony telluride bulk alloy, which is made by ball milling and hot press method, can produce bulk materials with $zT$ = 1.2 at room temperature and 1.4 at 100°C, which showed the possibility of commercialization of high efficiency thermoelectrics. Very recently, Zhao *et al.* used layered SnSe to achieved very low lattice thermal conductivity at 0.23 W/m-K, and thus lead to achievement of the $zT$ = 2.6 ±0.3, which is the highest reported until now[17].

## 1.2 Thermal Transport in Small Length Scale

Since using nanostructures can reduce the lattice thermal conductivity, to fundamentally understand how the structure size affects the thermal conductivity becomes more and more important. The key factor to compare with the nanostructure size is the mean free path. Thus, investigating which phonon mean free paths are important for heat conduction become an interesting topic recently. Dames *et al.*[18] first proposed that there is a broad distribution of phonon mean free paths using the concept of thermal conductivity per mean free path.

On the experimental side, there also are several important works reported recently. Siemens *et al.*[19] did the first quantitative measurement on transition from diffusive to ballistic thermal transport by using soft x-ray beams. They create 65-2000 nm wide nickel lines, which covers the average mean free path in sapphire, to observe the ballistic effect. Because of these periodic metal lines, the light would interfere with each other after getting diffracted from different metal lines. Thus, they can detect the dynamic temperature and measure the breaking down of Fourier's law. However, the problem of this method is the measurement system is complicated and expensive.

On the thermal conductivity spectra measurement, Minnich *et al.*[20] first measured the mean free path accumulation function of natural Si using time domain thermoreflectance (TDTR). The basic idea of TDTR is to shine a high power laser on the sample to provide heat flux, and use another lower power laser beam to detect the reflected signal, which is related to the temperature. By analyzing the reflected probe signal, one can obtain the thermal conductivity. In their method, the modification is by controlling the laser beam size to recover the thermal conductivity accumulation function[20, 21]. They assume when the beam size is comparable to part of the long mean free path distribution, the phonons with mean free paths longer than the spot size would not be excited and would not contribute to heat conduction.

Very recently, Johnson *et al.*[22] using the thermal grating membrane measured the room temperature accumulation function of Si. The basic principle is two laser beams interfering with each other to create transient thermal grating on the suspended thin film structure. In regions where the beams interfere constructively the temperature will be high; while destructively the temperature will be low. By analyzing the diffracted probe beam on the other side of the membrane, the thermal conductivity accumulation function can also be obtained. The membrane method has several advantages. It is a thin freestanding layer, thus there is no interface or contact with other materials. In addition, the width of the heater (and grating period) is easy to tune by changing the incident angle of the laser. The thickness of the membrane is usually thin, which make the heat conduction one dimensional and easy to analyze.

These thermal conductivity accumulation measurement and also previous modeling[18] indicate there is a broad distribution. To understand this distribution, it is still necessary to do a systematic investigation on the mean free path spectra. For these different analytical bulk thermal conductivity models, which model is the most appropriate to extend to the nanoscale? How the accumulation function can be used? How the thermal conductivity is affected by the nanostructure? There questions in the length scale are discussed in Chapter 3. Comparison of different models has been made. A convenient method of using bulk mean free path spectra to calculate effective thermal conductivity of a nanostructure has been obtained[23].

## 1.3 Thermal Transport in Short Time Scale

For the phonon transport, in addition to the size effect at small length scale, there would also be time effect at short time scale. This effect in short time scale is also called ballistic effect. This effect becomes more and more important recently in the semiconductor industry with the increasing of the computer clock frequency, because it affects the heat dissipation. The heat dissipation problems for the computer or cell phone chips become one of the greatest challenges. For instance, the highest clock frequency is the IBM zEC12 at present (released in the middle of 2013) [24] [25], with the clock speed of 5.5 GHz, which corresponds to the time period of ~100 ps. This period is comparable to the major phonon MFTs in semiconductor at room temperature[25].

Similar to the size effect that decreasing the device size would decrease the apparent thermal conductivity, the faster clock would also decrease the apparent thermal conductivity. However, for better power dissipation, it is necessary to have materials with high thermal conductivity. Thus, it would be crucial to understand how heating frequency would affect the apparent thermal conductivity. The main physics of the apparent thermal conductivity reduction is that when the characteristic time (heating period) is comparable or smaller than the phonon mean free time, which is the time between a phonon's collisions, their contribution to the thermal conductivity would be greatly suppressed, because only part of the phonons can participate in the transport.

Experimentally, there are different works recently on how the heating frequency would affect the thermal transport. Koh and Cahill[25] did the first modulation heating frequency dependent thermal conductivity measurement on single crystal and alloy materials. They found semiconductor alloys, such as SiGe, InGaP, and InGaAs, have a frequency dependence. They also use the method of TDTR. Their interpretation of the data is based on the constraint of penetration depth[25] [26]. This penetration depth functions as a characteristic length scale which they compared to the phonon mean free paths. Using the penetration depth, the time domain concept, heating frequency, has been transferred to length scale. One of the greatest advantages of this method is that the penetration depth is tunable by modulating the heat source heating frequency. The higher the frequency, the shorter the penetration depth. When the penetration depth is comparable or smaller than some of the long mean free path phonons, the long mean free path phonons would get constrained. Their corresponding contribution to the total thermal conductivity would also be reduced. Thus, there would be a heating frequency dependent thermal conductivity.

There are also other methods used to measure the heating frequency dependent thermal conductivity. One of the examples is frequency domain thermoreflectance (FDTR)[27, 28], which has much lower cost comparing to time domain thermoreflectance (TDTR)[21]. In this setup, the continuous laser diode can be sufficient. The challenge of this method is to achieve high modulation frequency to make the penetration depth comparable to the mean free path. The electro-optic modulator in the literature has a maximum of 200 MHz[26], which corresponds to the mean free path in the order of ~100 nm. This is sufficient for some long mean free path materials, such as silicon or sapphire. But, for very low mean free path materials, such as amorphous $SiO_2$ or silicon, this method is not sensitive to its mean free path range[26].

The heating frequency dependent apparent thermal conductivities are explained by the non-diffusive effect. However, in the experiment discussed above, the apparent thermal conductivity is obtained by using the Fourier law based framework, which already fails when there has non-diffusive effect. It is necessary to develop data analysis tools to explain the non-diffusive heat conduction. It is also important to investigate how broad the phonon distributions are in the mean free time domain. These topics are covered in Chapter 4.

## 1.4 Thermal Transport at Cryogenic Temperature

When temperature decreases to cryogenic temperature, such as the thermoelectric power generator in outer space[29], the phonon mean free path and mean free time both would be longer. Thus, part of the phonons would possibly transport ballistically. Some criteria used to select thermoelectric materials may not be valid any more. For instance, in thermoelectrics, the high $zT$ requires materials with low thermal conductivity $\kappa$. The common rule at room temperature or above would be using heavy atom semiconductors

which usually have low sound velocity, such as PbTe or $Bi_2Te_3$. However, at cryogenic temperature, as shown in this work, this material selection rule would be opposite comparing to the rule at high temperature. This can be explained by the phonon freeze-out effect[30], which is discussed in Chapter 5.

## 1.5 Organization of the Dissertation

This dissertation considers the phonon transport in small length scale and short time scale using the Boltzmann transport equation. The ballistic effect on both scales are investigated. Low temperature thermal transport properties are also investigated.

This dissertation is organized as follows:

Chapter 2 investigates thermal conductivity of randomly oriented superlattice polycrystals using Boltzmann transport equation. Both the in-plane and cross-plane thermal conductivities are obtained. The effective thermal conductivity is obtained using a "correlational approximation". This theory is verified by finite element simulation. The theoretical results are compared with experiments from our collaborators. How different parameters would affect the thermal conductivity has also been investigated.

Chapter 3 builds up a theory for phonon mean free path spectra for steady state heat conduction. It is found the long mean free paths play a important role. An integral transform framework is established to evaluate the nanostructure thermal conductivity. This framework has been used in the nanowire and in-plane thin film for case study.

Chapter 4 discusses phonon transient behavior. The heating frequency dependent thermal conductivity has been investigated also by Boltzmann transport equation. A framework on how to measure the accumulation function with respect to mean free time has been discussed. An analogy of phonon transport in time domain and space domain has also been made.

Chapter 5 discusses the thermal transport at the cryogenic low temperature. It discusses the thermal contact resistance crossover at cryogenic temperature.

Finally, Chapter 6 summarizes the major work of this dissertation and proposes several future problems.

# Chapter 2 Thermal Conductivity of Randomly Oriented Superlattice Polycrystal

## 2.1 Introduction

The main work of this chapter is based on our recent publication [Yang, Ikeda, Snyder, and Dames, *Journal of Applied Physics* 108, 034310 (2010)].[23]

Controlling lattice thermal conductivity, especially by reducing it, has attracted great attention nowadays, because the reduction of thermal conductivity can improve the thermoelectric performance. There are various methods to achieve this goal, ranging from doping impurities to defect scattering, to bringing in interfaces or grains to increase boundary scattering. With the development of nanotechnology, the later one of using interfaces becomes more and more important. Different structures have been investigated by researchers, such as thin film, superlattice, nanowire, quantum dot, *etc*. The superlattice is one of the most important structures which introduced a series of interfaces and can effectively increase the phonon scattering at the interface[31, 32] to reduce the effective thermal conductivity in both the in-plane[33] and cross-plane[8] directions.

Most superlattice structures were obtained using molecular beam epitaxy (MBE) or metal-organic chemical vapor deposition (MOCVD) [8, 33], because these methods can control the interface quality and layer thicknesses very precisely. High quality superlattice structures have been used in various fields, such as light emitting diode, laser diode, and chip cooling device [34]. However, one of the major considerations of these methods is that they need complicated and expensive equipment, thus the sample cost would be very high and can not be easily scaled up for mass production.

Therefore, much recent attention has been working toward the direction of low-cost synthesis methods to create bulk-scale samples with internal nanostructures inside. These methods would usually dramatically reduce the synthesis cost and enhance the massive production with the cost of some degree of sample quality. There are several materials systems that use this "nano-bulk" approach[35] to create nano grains in the bulk samples, such as hot pressed ball milled nano-powders (such as $Bi_xSb_{2-x}Te_3$ system[16, 36, 37]), complex crystal structures (such as skutterudites, clathrates, and Zintl phases) [29], or self-assembled composites (such as precipitates[38] or lamellae of $PbTe/Sb_2Te_3$. [Ref. [36]) One of the characteristics of these materials systems is that they are bulk samples but contain nano-grains. For instance, the lamellae of the $PbTe/Sb_2Te_3$ system (Ref. [36]), which will be studied in this work, is made of numerous randomly-rotated superlattice grains with the period in order of ~100nm or above. The thermal property would be very anisotropic in different directions of the superlattice due to the anisotropy of the materials[36]. However, on the macroscale it would be isotropic due to random orientation, as shown in Fig. 2.1(a). This chapter will investigate the effective thermal conductivity $\kappa_{eff.}$ of randomly-rotated superlattice nano-grains.

This chapter will focus on the materials systems of self-assembled $PbTe/Sb_2Te_3$ nano-composite[29, 36]. We built up a model, based on the Boltzmann transport equation, to evaluate the effective macroscopic thermal conductivity $\kappa_{eff}$ of bulk polycrystalline materials. The model discussed the relationship between $\kappa_{eff}$, in-plane $\kappa_x$, and cross-plane $\kappa_z$ of the superlattice. The validity of this relationship has been verified by the Finite Element Method (FEM). With this verified general model, next goals are calculating the in-plane and cross-plane thermal conductivity separately using the BTE solution[31, 32, 39] with the gray assumption. The information needed for the in-plane and cross-plane thermal conductivity are shown in Fig. 2.2. The sequence of calculating the thermal conductivity is also shown in Fig. 2.2. After obtaining the gray solution, we extend the gray solution to frequency dependent regime to include all phonons with different vibrational frequencies. After building up the model, we investigate different effects, such as the interface smoothness, thickness, and temperature. We also compare our model with experimental measurements from our collaborators, and discuss the underlying physics.

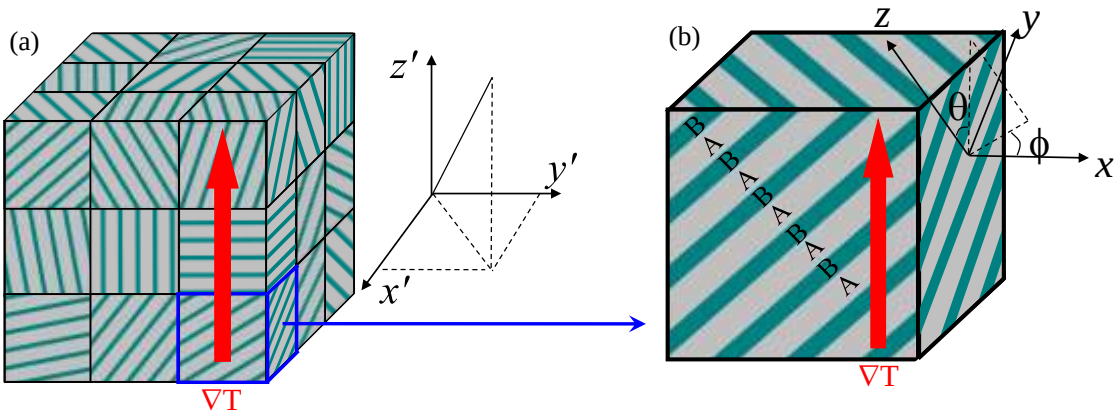


**Figure 2.1 (a) Schematic of a nano-bulk composite material made of randomly oriented superlattice grains with the global coordinate system *x'y'z'* and (b) a single superlattice grain with its local coordinate system *xyz* aligned to the superlattice planes.**

## 2.2 Effective Thermal Conductivity on the Macroscale

### 2.2.1 General Theory

This subchapter focuses on building up a relationship between the general effective thermal conductivity and elements of the thermal conductivity tensor. We use the self-assembled $PbTe/Sb_2Te_3$ lamellar structures reported in Ref. [36] as an example. The superlattice grain size is in the order of μm with superlattice period in several hundreds nm, but the bulk materials contain numerous of these grains. For the orientation probability of the nano-grain, we assume each direction has the same opportunities. Since these samples are self-assembled, the contact resistance between different grains would be small compared to the resistance between material A and B in Fig. 2.1(b), thus we neglect these contact resistances between different grains. We also define the coordinate here. For the local directions, we define a local coordinate system with the local *z*-axis aligned along the cross-plane direction of superlattice, and the local

*x*- and *y*-axes along in-plane of the superlattice (Fig. 2.1b). We also restrict our analysis to materials systems where the thermal transport properties in the local *x* and *y* directions are identical due to the symmetry. Thus, for the thermal conductivity tensor, **K**, within the grain, the elements in the *x* and *y* directions are the same. Thus, in the local coordinate system, the thermal conductivity tensor of a single grain can be expressed as

$$\mathbf{K} = \begin{pmatrix} \kappa_x & 0 & 0 \\ 0 & \kappa_x & 0 \\ 0 & 0 & \kappa_z \end{pmatrix}. \tag{2.1}$$

Here the element of $\kappa_x$ and $\kappa_y$ are the same, thus we use $\kappa_x$ replace the $\kappa_y$ in the whole chapter. Because of the symmetries, the diagonal elements are all zero in the local *xyz* coordinate system. Before we discuss the full theory of the nano-bulk system, we first consider two extreme cases, the thin polycrystalline film and the long wire, as shown in Section 2.2.2 and 2.2.3.

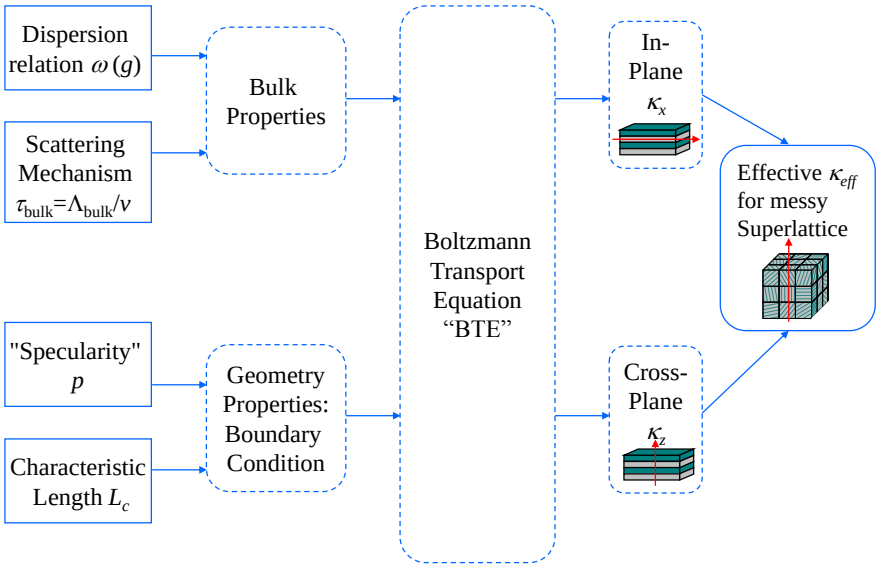


**Figure 2.2 Flow chart of obtaining effective thermal conductivity for messy superlattice.**

### 2.2.2 Average Thermal Conductivity for a Thin Film

We will discuss the thin polycrystalline film in this subchapter as shown in Fig. 2.3(a). The polycrystalline film is made up of may grains, with same thickness, on the same plane, but each grain has different orientation. Both the top and bottom surface of the thin film are isothermal.

The local heat flux through the thin film can be evaluated by

$$\mathbf{q} = -\mathbf{K}\nabla T = -\mathbf{K}\hat{\mathbf{s}}\left\|\nabla T\right\|, \tag{2.2}$$

where $\nabla T$ is the temperature gradient vector, which has magnitude $\left\|\nabla T\right\|$ and points in the $\hat{\mathbf{s}}$ direction, and ***q*** is the heat flux vector. The $\hat{\mathbf{z}}'$ direction of global *x'y'z'* coordinate system has also been defined using the $\hat{\mathbf{s}}$. Thus, in the local coordinate, the $\hat{\mathbf{s}}$ direction can be expressed as

$$\hat{\mathbf{s}} = \begin{pmatrix} \sin\theta\cos\phi \\ \sin\theta\sin\phi \\ \cos\theta \end{pmatrix}, \tag{2.3}$$

where $\theta$ and $\phi$ describe the rotation of the grain's coordinate system away from the imposed $\nabla T$.

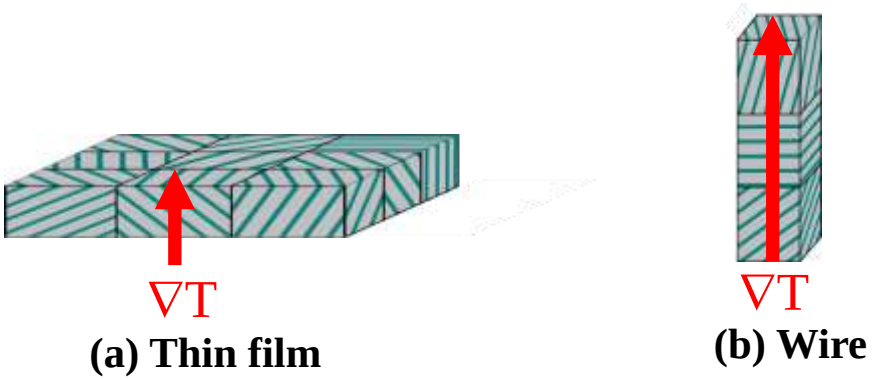


**Figure 2.3 Schematics of (a) nano-grain thin film and (b) nano-grain wire.**

In the case of polycrystalline film, the top and bottom boundaries are isothermal. All the grains have the identical average temperature gradient $\nabla T$. Thus, the key here is to evaluate the effective heat flux along the $\nabla T$ direction. For a single grain, the average heat flux would be $q_{net} = \mathbf{q} \cdot \hat{\mathbf{s}}$. Consider the angular dependence of the heat flux, the net heat flux from top layer to the bottom layer would be $q_{net} = -\left(\kappa_x \sin^2\theta + \kappa_z \cos^2\theta\right)\|\nabla T\|$. Thus, in analogy to the heat conduction in isotropic form, we can obtain the effective thermal conductivity

$$\kappa_{eff} = -\frac{q_{net}}{\|\nabla T\|} = \kappa_x \sin^2\theta + \kappa_z \cos^2\theta. \tag{2.4}$$

This $k_{eff}$ is only for a single grain. When considering all the grains with random orientation in the thin film, each direction is equally distributed over the full solid angle Ω. Thus, the effective thermal conductivity for the film would be

$$\kappa_{eff,film} = \frac{1}{4\pi}\int_0^{4\pi} \kappa_{eff}\, d\Omega = \tfrac{2}{3}\kappa_x + \tfrac{1}{3}\kappa_z. \tag{2.5}$$

To make a comparison of this limiting case to the general effective thermal conductivity, we will rewrite this $\kappa_{eff,film}$ in a dimensionless form with respect to the thermal conductivity contrast parameter $r = \kappa_z / \kappa_x$ and characteristic thermal conductivity $\kappa_{char} = \left(\kappa_x^2 \kappa_z\right)^{1/3}$. Thus, the effective thermal conductivity of thin film in Eq.(2.5) can be expressed as

$$\kappa_{eff,film} / \kappa_{char} = \tfrac{2}{3} r^{-1/3} + \tfrac{1}{3} r^{2/3}. \tag{2.6}$$

### 2.2.3 Averaging Thermal Conductivity for a Long Wire

In this subchapter, we will discuss another limit of nano-grains which all grains with the same size and along a long wire, as shown in Fig. 2.3(b). Along the wire, the same heat flux would pass through each grain. The temperature gradient of each grain would be different. Thus, the temperature gradient $\|\nabla T\|$ would also be different. In this case, the heat flux $\mathbf{q}$ is the forcing and $\nabla T$ is the response to the heat flux. Thus, the temperature gradient would be $\nabla T = -\mathbf{K}^{-1}\mathbf{q} = -\mathbf{K}^{-1}\hat{\mathbf{s}}\|\mathbf{q}\|$, where $\hat{\mathbf{s}}$ refers to the direction of the average heat flux. Using similar averaging rules as the thin film in previous subchapter, the temperature gradient components along the average heat flux direction would be $\|\nabla T\|_{net} = \left(-\mathbf{K}^{-1}\hat{\mathbf{s}}\|\mathbf{q}\|\right)\cdot\hat{\mathbf{s}}$. Considering the random orientation, after integrating over all solid angle $\Omega$, we obtain the effective thermal conductivity of the long wire

$$\kappa_{eff,wire} = \left(\tfrac{2}{3}\kappa_x^{-1} + \tfrac{1}{3}\kappa_z^{-1}\right)^{-1}. \tag{2.7}$$

We also use the thermal conductivity contrast parameter $r = \kappa_z / \kappa_x$ and characteristic thermal conductivity $\kappa_{char} = \left(\kappa_x^2 \kappa_z\right)^{1/3}$, thus we can rewrite the $\kappa_{eff,wire}$ in a dimensionless form

$$\kappa_{eff,wire} / \kappa_{char} = \left(\tfrac{2}{3} r^{1/3} + \tfrac{1}{3} r^{-2/3}\right)^{-1}. \tag{2.8}$$

### 2.2.4 Averaging Thermal Conductivity for Nano-bulk

For the randomly oriented grain, Mityushov and Adamesku used a "correlational approximation" [40] and obtained a approximate solution, which has the form of

$$\kappa_{eff,bulk,MA} / \kappa_{char} = \tfrac{1}{3} r^{2/3} + \left[\tfrac{2}{3} - \tfrac{2}{9}\left(\frac{(r-1)^2}{r+2}\right)\right] r^{-1/3}. \tag{2.9}$$

To the best of our knowledge, this expression is not known in the Western literature and no comparison of this method has been made. In the chapter 2.2.5, we would verify it by our FEM simulation. We will see that this method has a much better accuracy than limiting case discussion above and in literature[41, 42]. For instance, the upper bound effective bulk thermal conductivity from Adams *et al.*[42] that $\kappa_{eff,bulk,UB} = \kappa_{eff,film}$ or the lower bound from Schulgasser[43] with the form of $\kappa_{eff,bulk,LB} / \kappa_{char} = \tfrac{1}{2} r^{2/3}\left(-1 + \sqrt{1 + 8r^{-1}}\right)$. Finally, in this work, we would use the more general results from "correlational approximation" in Eq.(2.9).

### 2.2.5 Numerical Analysis and Verification

In this subchapter, we performed the FEM simulation, three-dimensional numerical simulations using COMSOL multiphysics, to verify the results of "correlational approximation", the thin film limit, and long wire limit. We summarize the details of the simulation in Table 2-1. In the simulation, the size of each grain is expressed by $L_x \times L_y \times L_z$. The number of grains in the sample is an array $N_x \times N_y \times N_z$. To mimic the conditions of thin film, wire, and bulk, we choose a flat, elongated, and cubic structure for each case, respectively. With the configuration of the simulation

structure, the next input for the FEM is the boundary conditions. We also listed them in Table 2-1. For the thin film structure, since the lateral direction is infinite, we use a periodic boundary condition to represent this boundary condition. In the other limit of long wire, due to the lateral confinement, heat would only flow in the wire direction, thus we would use the adiabatic condition as the lateral boundary condition.

**Table 2-1 Simulation structure, boundary conditions, and other input parameters used in FEM simulations.**

| | Thin Film | Thin Wire | Nano-Bulk |
|---|---|---|---|
| Grain Configuration ($N_x \times N_y \times N_z$) | $6 \times 6 \times 1$ | $1 \times 1 \times 20$ | $4 \times 4 \times 4$ (most runs)<br>$5 \times 5 \times 5$ (several runs) |
| Grain Size ($L_x \times L_y \times L_z$) | $10 \times 10 \times 0.1$ | $1 \times 1 \times 10$ | $1 \times 1 \times 1$ |
| Boundary Conditions | Constant $T$ ($z$ faces); Periodic ($x$ and $y$ faces) | Constant $T$ ($z$ faces); Adiabatic ($x$ and $y$ faces) | Periodic with fixed $T$ difference ($z$ faces); Periodic ($x$ and $y$ faces) |
| Equation for comparison | Eq. (2.6) | Eq. (2.8) | Eq. (2.9) |

With both the structure and boundary conditions, we can run the FEM simulation. The thermal conductivity tensor of the nano-grain is assigned randomly by the COMSOL Matlab interface. We generated the random function as the thermal conductivity tensor in the Matlab and transfer it to COMSOL through the interface. The tensor has the principal conductivity $\kappa_x$ and $\kappa_z$ (where $\kappa_x = \kappa_y$). The grain has been rotated by any random angle. This can be expressed by a randomly rotated matrix $\mathbf{R}$ in Ref. [44]. Thus, the thermal conductivity tensor of the grain finally has the tensor of $\mathbf{R}^T\mathbf{K}\mathbf{R}$.

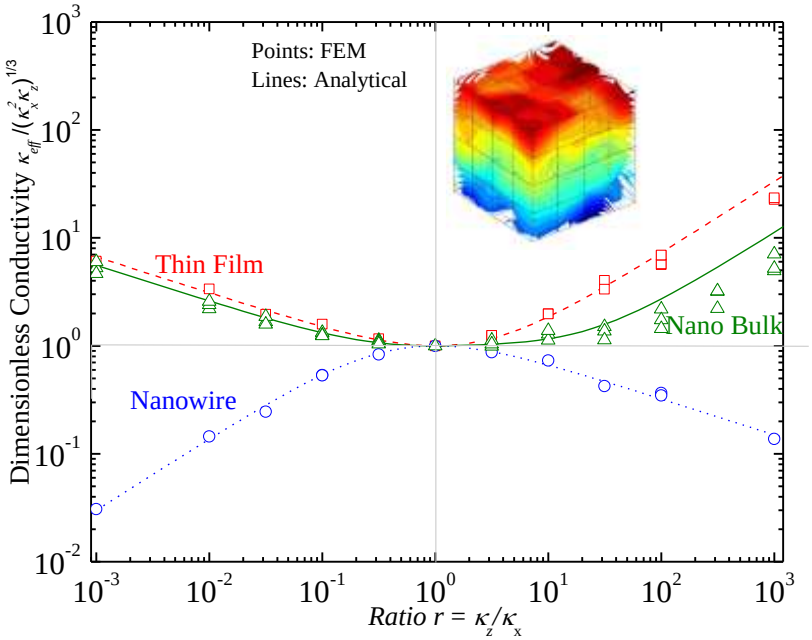


**Figure 2.4 Averaging rules for the effective thermal conductivity of polycrystalline thin films, wires, and nano-bulk materials. Points are from FEM simulations. Green line is analytical result from Mityushov and Adamesku approximation. Red and blue line are results of Thin film (Eq. 2.6) and nanowire (Eq. 2.8). The inset is typical FEM simulation of a 4×4×4 nano-bulk configuration.**

The FEM results are shown in Fig. 2.4. The *x*-axis is the thermal conductivity contrast parameter $r = \kappa_z / \kappa_x$ and the *y*-axis is the effective thermal conductivity normalized to characteristic thermal conductivity $\kappa_{char} = \left(\kappa_x^2 \kappa_z\right)^{1/3}$. The numerical results verify that Eq. (2.6) and Eq. (2.8) are appropriate for thin film and long wire, even though large deviation happens at large *r*. For thin films and wires, they have totally different trends. If we fixed the characteristic thermal conductivity $\kappa_{char}$, for the thin film, the larger thermal conductivity contrast parameter *r*, the larger $\kappa_{eff}$. Because all the nano-grains are in parallel, probably the large $\kappa_z$ dominates the heat conduction at larger *r*. For the wire, it is a opposite trend. Since heat need to pass through every grain, if the contrast parameter *r* is too large, some grains which have very small $\kappa_x$ would block the heat conduction, and greatly reduce the total effective thermal conductivity.

The power law of the effective thermal conductivity have also been observed for thin film, wire, and nano-grain structure in Fig. 2.4. Both the power law of $\kappa_{eff} / \kappa_{char} \propto r^{2/3}$ or $\kappa_{eff} / \kappa_{char} \propto r^{-1/3}$ in both the limits of large and/or small *r*, have been observed. For the thin film, which means parallel conductance, we have $\kappa_{eff} / \kappa_{char} \propto r^{2/3}$ for $r >> 1$ and $\kappa_{eff} / \kappa_{char} \propto r^{-1/3}$ for $r << 1$. In the other limit of long wire, with in series of resistance, we would have $r^{-1/3}$ ($r >> 1$) and $r^{2/3}$ ($r << 1$). For our randomly oriented nano-grain, both the analytical calculation and the FEM tends to show that the nano-grain behaviors as thin film. Thus, the parallel conductance but not the series resistance is more suitable for interpretation of the effective thermal conductivity of the nano-grain.

Figure 2.3 also shows the "correlational approximation" from Mityushov-Adamesku (M-A) agrees with the FEM simulation the best for a wide range of *r*. For $r<0.01$, the disagreement is approximately 8%. Within $r<10$, the disagreement is very small within 10%. Even when $r = 100$, there disagreement is still within 35%. We speculate this reduction of FEM simulation comparing to M-A is partially due to cubic grains arrayed in a cubic lattice assumption. For the cubic structure, it can only interact with 6 of its neighbors. However, a unit cell with different symmetry can have much more neighbors and have more interconnections. For instance, the face-centered cubic lattice would have 2 neighboring grains. Thus, more interactions between the grain and its neighbors would increase the macroscopic effective thermal conductivity. Thus, the cubic assumption in this FEM simulation would reduce the effective thermal conductivity. This reduction effect is expected to stronger at larger *r*, because when *r* is very large, the *x* and *y* two directions will tend to block the heat flow. Thus, only two interfaces are interacting with neighbors. Thus, the disagreement is larger at larger *r*.

## 2.3 Modeling in-plane and cross-plane conductivity of a single superlattice grain

This section discusses the modeling of superlattice thermal conductivity. In a superlattice, when the superlattice period length is comparable or even smaller than the

phonon mean free paths, the heat diffusion equation would fail. Thus, the Boltzmann Transport Equation (BTE), which captures the ballistic effects, needs to be used. The BTE method approximates the phonons as classical particles and neglects the possibility of coherent wave interference effects. This assumption is appropriate for self-assembled materials considering the length scales here. For instance, the thickness of period in this work is in the order of hundreds nanometers (283 nm as minimum for PbTe/$Sb_2Te_3$ system), which is two orders of magnitude larger than the 1 nm typical phonon wavelengths, which is estimated from Debye temperature[18].) In literature, there are solutions to BTE in both superlattice in-plane and cross-plane which are based on gray relaxation time assumption[31, 32, 39]. In this work, we use the in-plane solution and extend the gray solution in cross-plane direction.

### 2.3.1 Approximating the Dispersion Relations

For materials with more than one atom in the primitive unit cell, there are optical phonons. Since the dispersion of optical phonon is almost flat, the group velocity could be approximated as zero. Thus, the optical phonon's contribution would be neglected. For the acoustic phonons, the isotropic Born-von Karman dispersion is used [31, 45]

$$\omega = \omega_0 \sin\left(\frac{\pi q}{2q_0}\right) \tag{2.10}$$

where $q$ is the wavevector, $q_0 = \left(6\pi^2\eta\right)^{1/3}$ is a cutoff wavevector, $v_s$ is the sound velocity, $\eta$ is the number of primitive unit cells per unit volume, and $\omega_0 = 2v_s q_0 / \pi$ is a characteristic frequency. This dispersion is also relatively simple, but it is more realistic than the Debye approximation because it captures the group velocities at the Brillouin zone edge, which are much smaller than the sound velocity. In addition, the computational effort needed is much less than the exact phonon dispersion calculation[46]. This is especially useful when applied to complicated material system whose full dispersion relations are not known, because the acoustic dispersion is fully determined by the parameters density of primitive unit cells $\eta$ and sound velocity $v_s$.

With the dispersion, we can obtain other thermal properties, such as density of states $\rho(\omega)$ and specific heat $C(\omega)$. We first consider the single polarization branch, the density of states is $\rho(\omega) = \frac{q^2}{2\pi^2 v}$, where $v$ is the group velocity which is the slope of the dispersion, $v = \partial\omega / \partial q$. It is also common to lump two transverse branches and one longitudinal branches into three identical one, with the average group velocity $v_{avg}(\omega)$. Thus, the total density of states is $\rho(\omega) = \dfrac{3q^2}{2\pi^2 v_{avg}}$. For thermoelectric application, we are usually interested in the high temperature regime which is usually well above the Debye temperature $\theta_D$. In this case, the effective sound velocity can be shown to be the arithmetic average of the three branches, $v_{s,avg} = \frac{1}{3}v_{s,L} + \frac{2}{3}v_{s,T}$. In addition, we can also obtain the volumetric specific heat per unit frequency $C(\omega)$ that $C(\omega) = \hbar\omega\rho\dfrac{\partial f}{\partial T}$ where $f$ is the Bose-Einstein distribution function and $\hbar$ is the reduced Planck constant.

### 2.3.2 Phonon Scattering Mechanisms in Bulk

The key to determine thermal conductivity is its scattering mechanisms, which here we describe by the phonon frequency dependent mean free path $\Lambda_{bulk}(\omega)$. For the bulk materials, most common scatterings are the impurity scattering and phonon-phonon Umklapp scattering. These two scatterings are usually combined together using Matthiessen's rule [30] that

$$\Lambda_{bulk}^{-1} = \Lambda_{imp}^{-1} + \Lambda_{umkl}^{-1} \tag{2.11}$$

The impurity scattering can be evaluated by a Rayleigh expression $\Lambda_{imp}^{-1} = A_1 \omega^4 / v_{avg}$, where the $A_1$ is a fitting parameter obtained from fitting the bulk thermal conductivity. It can also be evaluated by theory, which is affected by the mismatch of atoms' weight, volume, and stress[47]. The Umklapp mean free paths are common expressed as[48]

$$\Lambda_{umkl}^{-1} = B_1 \omega^2 T \exp(-B_2 / T) / v_{avg} \tag{2.12}$$

where $B_1$ and $B_2$ are fitting parameters, and $T$ is the absolute temperature. $B_2$ can also be written $\theta_D/const$, where *const* is usually not too different from 3.[49] In thermoelectrics, most heavy semiconductors have low Debye temperature. For example, in this work we work on PbTe ($\theta_D \approx 136$ K)[50] and $Sb_2Te_3$ ($\theta_D \approx 160$ K)[50] at room temperature and above, which are both satisfy $T >> \theta_D/3$. Thus, the exponential function $\exp(-B_2 / T)$ can be simplified as 1. Furthermore, except very heavily doping, the impurity usually only play roles at very low temperature. In our case (at >300 K), the main scattering is still the phonon-phonon Umklapp scattering. Thus, the bulk mean free path can be simplified as

$$\Lambda_{bulk}^{-1} \approx \Lambda_{umkl}^{-1} \approx B_1 \omega^2 T / v_{avg} \tag{2.13}$$

Thus, in this case, only $B_1$ needs to be obtained to calculate the bulk thermal conductivity.

Since we already made several assumptions, it is necessary to check the validity of them. We check the Umklapp scattering expression in Eq. (2.13) by comparing the theoretical results of this expression with experimental data from literature of both PbTe[51, 52] and $Bi_2Te_3$.[53] For PbTe, at high temperature of our interests, the experimental data is very well fitted with the power law $T^{-1}$. We can see from Fig. 2.5 that the expression in Eq.(2.13) agreed very well with the experimental data for PbTe above room temperature. This also means if lacking bulk experimental data for the fitting, a single experimental data point can be used to obtain the fitting parameter $B_1$. This is essential for $Sb_2Te_3$ because we lack experimental data to determine the temperature dependent thermal conductivity in literature[54]. To further test the validity of this assumption, we use $Bi_2Te_3$ to test the model, since both $Sb_2Te_3$ and $Bi_2Te_3$ have the same crystal structure. As we can see in the inset of Fig. 2.5, using Eq.(2.13), we find the single parameter fitting can also be applied to $Bi_2Te_3$ in both directions. The values of the parameters in both the *a*-plane and *c*-axis directions are summarized in Table 2-2.

**Table 2-2 Properties for PbTe and $Sb_2Te_3$ at 300 K. The adjustable parameters $B_1$ for $Sb_2Te_3$ were fitted using the room temperature bulk phonon thermal conductivities $\kappa_{ph,FL}$ in Ref. [55]. Densities of primitive unit cells $\eta$ are calculated using the lattice constant and crystal structure. The sound**

**velocities $v_s$ of $Sb_2Te_3$ are estimated from those of $Bi_2Te_3$ using the scaling arguments explained in Chapter 2.7.**

| Parameters | PbTe | $Sb_2Te_3$ (*a*-plane) | $Sb_2Te_3$ (*c*-axis) |
|---|---|---|---|
| $B_1$ ($10^{-18}$ s/K) | 6.2[f][18][j] | 4.3 | 27.8 |
| Lattice constant (Å) | 6.462[f][50][j] | 4.25[f][50][j] | 30.35[f][50][j] |
| $\eta$ ($10^{28}$ m$^{-3}$) | 1.482 | 0.6329 | 0.6329 |
| $v_s$ (m/s) | 1730[f][18][j] | 2333 | 2270 |
| $K_{ph,FL}$ at 300K (W/m-K) | 2.0[f][18][j] | 2.2[f][55][j] | 0.34[f][55][j] |

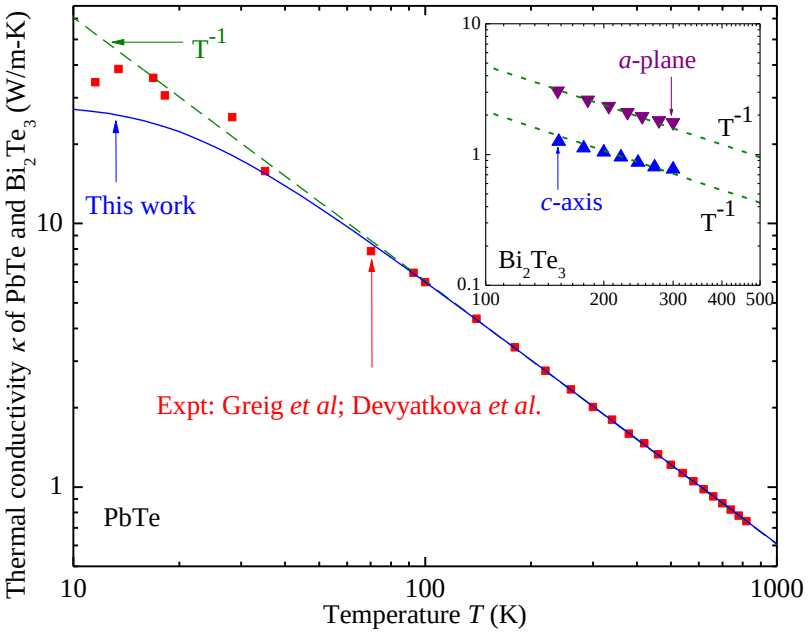


**Figure 2.5 Theoretical thermal conductivity of PbTe using only the high-temperature Umklapp expression, as compared to experimental data from Greig in Ref. [51] and Devyatkova in Ref. [52]. Above 80 K, the data and model follow a $T^{-1}$ relation almost perfectly. Inset: Experimental data[53] for the thermal conductivity of $Bi_2Te_3$ in both *c*-axis and *a*-plane directions also follows a $T^{-1}$ relation around room temperature.**

### 2.3.3 Considerations for Anisotropic Constituent Materials

This work only focuses on materials with the isotropic dispersion and group velocity. This assumption has been used for many cubic materials, such as Si, Ge, PbTe, and most III-V semiconductor (GaAs *etc*), and good agreement has been shown in the literature. However, for $Sb_2Te_3$, it is a hexagonal material with significant anisotropy in the *ab*-plane and *c*-axis direction. In this work, we assume the *c*-axis direction is always along the cross-plane of the superlattice and *ab*-plane is on the same family of plane of the in-plane. Thus, we can treat the *ab*-plane and *c*-axis independently. When considering the cross-plane thermal conductivity, we use the *c*-axis effective sound velocity to fit the *c*-axis thermal conductivity to obtain the $Sb_2Te_3$ Umklapp parameter $B_1$.

### 2.3.4 In-plane Thermal Conductivity $\kappa_x$

The in-plane thermal conductivity of superlattice has been investigated by Chen using Boltzmann transport equation[31]. It is found that when the period thickness decreases, the in-plane thermal conductivity of superlattice would be greatly decreased. An analytical solution to the BTE has been obtained with the expression

$$\kappa_x = \sum_{i=1}^{2} \frac{d_i}{d_1 + d_2} \int_0^{\omega_{0,m}} \frac{1}{3} C_i v_{avg,i} \Lambda_{bulk,i} \left\{ 1 - \frac{3\Lambda_{bulk,i}}{2d_i} \left[ pG_{si}(\xi_1, \xi_2) + (1-p) G_{di}(\xi_1, \xi_2) \right] \right\} d\omega \qquad (2.14)$$

where $i$ =1,2 represents the layer numbers, $d_i$ is the layer thickness of the corresponding layer, $\xi_i = d_i/\Lambda_{bulk,i}$ is the layer thickness normalized to the bulk mean free path, $\omega_{0,m}$ is maximum phonon frequency, $p$ is the specularity parameter which captures the effects of the interfacial roughness, and $G_{si}$ and $G_{di}$ are dimensionless integral functions given in Ref. [31].

The specularity can be expressed by the root mean square surface roughness $\delta$ using $p = \exp(-16\pi^2\delta^2/\lambda^2)$, where $\lambda$ is the phonon wavelength. This widely used expression is given in Ziman's book [56] but there is contained an erroneous factor of $\pi$. The correction is in Zhang's book[57]. We did our own calculation, and confirmed Zhang's observation. The meaning of the specularity is the percentage of phonons which are reflected as perfect smooth surface. For instance, if $p$ = 1, all the phonons reflected specularly on the surface, as shown in Fig. 2.6(a). If $p$ = 0, all the phonons reflected diffusely, as shown in Fig. 2.6(b). In this case, the surface is very rough compared to the phonon wavelength. After the reflection, the phonons forget where they are from, thus the reflected phonon are isotropically distributed in all solid angle.

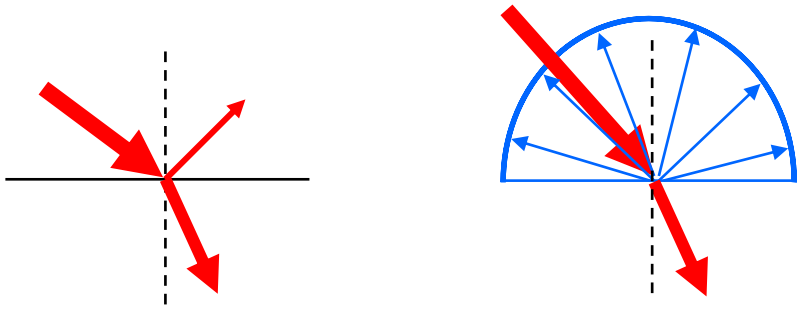


**Figure 2.6 (a) Specular and (b) diffuse interfaces**

### 2.3.5 Cross Plane Thermal Conductivity $\kappa_z$

Great thermal conductivity reduction has also been experimentally observed in the superlattice cross plane[8, 58], which is caused by the interface scattering. The Boltzmann transport equation has also been used to investigated the effects of these interfaces[32, 39]. For instance, in Ref. [32], Chen investigated different conditions for phonon scattering at the interface, such as elastic and inelastic scattering, and diffusive and specular interfaces. He found the inelastic acoustic mismatch model (AMM) agrees

with the experiments better than other models for GaAs/AlAs and Si/Ge superlattice. Thus, we also use the inelastic AMM in this work. To reduce the computational effort, the gray relaxation time approximation is used first, which means the phonon frequency dependent relaxation time is assumed to be a constant. We will also verify our gray model with literature Ref. [32], as the temperature profile shown in Fig. 2.7. The temperature profiles agree with the literature calculation[32]. There are a few percent difference between my simulation and the data from literature[32]. Possible reason could be the errors from extracting data from Ref. [32]. Even though the gray relaxation time approximation provide great convenience for modeling, it would lead to over-prediction of the thermal conductivity as discussed before in nanowire system[59]. Thus, we extend the gray relaxation approximation to the phonon frequency dependent model.

The frequency-dependent model breaks the dispersion into *l* small bands and each band is treated as gray model as Ref. [32]. The width of *j*-th band in the *i*-th layer (where $i$ =1,2) will be expressed as $\Delta\omega_{ij}$ and wavevector as $\Delta q_{ij} = \Delta\omega_{ij}/v(\omega_{ij})$, where $v(\omega_{ij})$, is the group velocity at $\omega_{ij}$. Thus, within the frequency range of $\Delta\omega_{ij}$, we treat it using the gray model and obtain its specific heat, group velocity, and mean free path. The volumetric specific heat for a single band within the frequency range of $\Delta\omega_{ij}$ is

$$\Delta C_{ij} = \hbar\omega_{ij}\rho(\omega_{ij})\Delta\omega_{ij}\frac{\partial f(\omega_{ij},T)}{\partial T} \tag{2.15}$$

Next step is to solve the BTE in this small frequency range $\Delta\omega_{ij}$. The mean free path can still be expressed as Eq.(2.13) that $\Lambda_{bulk}^{-1} \approx \Lambda_{umkl}^{-1} \approx B_1\omega_{ij}^2 T / v_{avg}$. Thus, the Boltzmann transport equation is[32]

$$\sin\theta_{ij}\cos\varphi_{ij}\frac{\partial I_{ij}}{\partial x} + \cos\theta_{ij}\frac{\partial I_{ij}}{\partial z_i} = -\frac{I_{ij} - I_{oij}}{\Lambda_{ij}} \tag{2.16}$$

This equation has the numerical solution as shown in Ref.[32]. The $\theta_{ij}$ is the polar and $\phi_{ij}$ is the azimuthal angle of local grain system as shown in Fig. 2.1(b). The $I_{ij}$ is the phonon intensity in the *i*-th layer and the *j*-th frequency band and $I_{oij}$ indicates the equilibrium phonon intensity with average over all directions (but not all frequency)[60]. Thus, after numerically solving Eq.(2.16), we can obtain the *j*-th frequency band's contribution $\Delta\kappa_{zj}$ to the total cross-plane thermal conductivity. Thus, summing up all the small bands' contribution, we obtain the cross-plane thermal conductivity

$$\kappa_z = \sum_{j=1}^{l}\Delta\kappa_{zj} \ . \tag{2.17}$$

Since phonons have both the spatial and angular dependence, both dependencies need to be considered. In the spatial domain across *z* direction, the temperature profile at the interface is sharper than the center of the layer. Thus, we use the Gauss-Legendre method, which has much finer mesh at the edges of the two integration limits. The challenge of the angular integration is that its mesh needs to match the inelastic acoustic mismatch model condition that[32]

$$\frac{\sin\theta_{1j}}{\sin\theta_{2j}} = \left(\frac{\Delta C_{2j}v_{2j}}{\Delta C_{1j}v_{1j}}\right)^{1/2} . \tag{2.18}$$

In this integration of angle, we uniformly divide the mesh into *m* parts in the top layer. Then, using Eq.(2.18), we calculate the corresponding angle in the bottom layer, which is non-uniform. In this layer, we use the trapezoidal integration to sum up all phonons' contributions. When the incident angles of some phonons are too large and reach total reflection, these phonons' contribution to the total cross-plane thermal conductivity has been neglected since it can not transport from one layer to another.

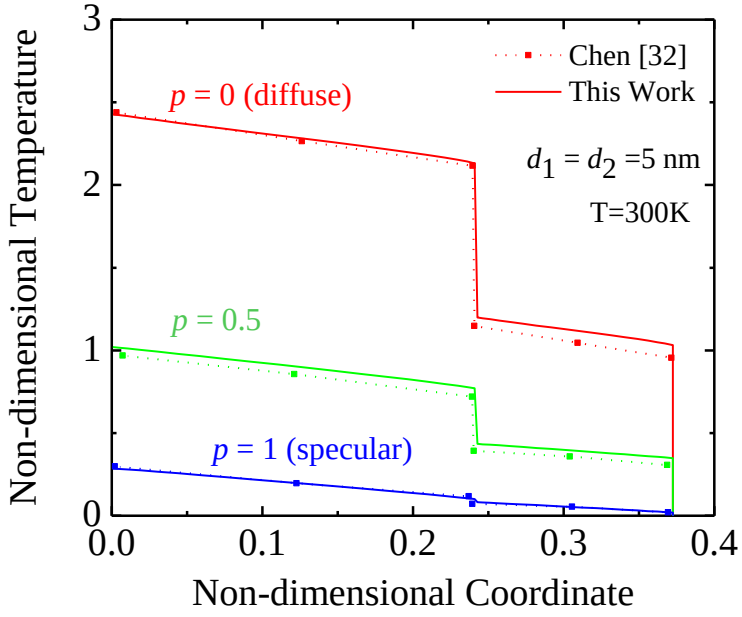


**Figure 2.7 Verification of the cross-plane thermal conductivity BTE solution, by comparison with the calculation from Chen's Fig. 5(c) [32].**

## 2.4 Numerical Results & Discussion

With the theory developed in the previous section, we now can apply it to the PbTe/$Sb_2Te_3$ system and compare it with the experiments. We will firstly obtain the in-plane and cross-plane thermal conductivity of the superlattice, then we combine them together to obtain the total effective thermal conductivity $\kappa_{eff}$ of the bulk polycrystal made of randomly oriented superlattice grains. With the $\kappa_{eff}$, we will investigate the effect the period *L*, surface roughness, and temperature. We also compare the gray model and frequency dependent model. In all the cases, the PbTe/$Sb_2Te_3$ thickness ratio use the reference value from experiment [36] and is fixed at $\frac{d_1}{d_2} = \frac{d_{PbTe}}{d_{Sb_2Te_3}} = \frac{2}{7}$.

### 2.4.1 Effect of Period

The period dependent thermal conductivities are shown in Fig. 2.8 for four different specularities. In each subfigure, the in-plane, cross-plane, and effective thermal conductivity obtained from the Mityushov-Adamesku averaging model are all shown. The cross plane thermal conductivity (red) is always lower than the in-plane (green) due

to strong interface scattering. One reason is that we choose *c*-axis of $Sb_2Te_3$ ,which has lower thermal conductivity, to always be along the cross-plane direction.

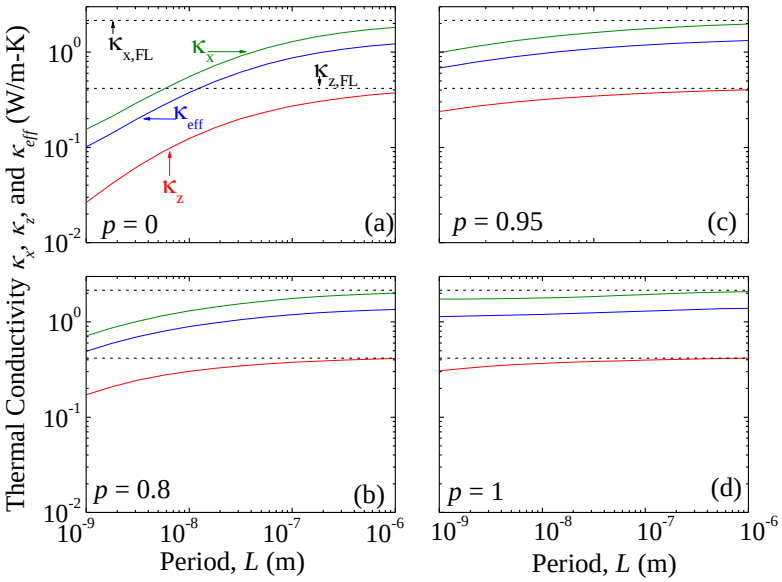


**Figure 2.8 Thermal conductivity as a function of period for four different values of the specularity parameter *p*, for a PbTe-$Sb_2Te_3$ nano-bulk system at *T*=300 K with thickness ratio PbTe:$Sb_2Te_3$ = 2:7. Solid lines: $\kappa_x$ and $\kappa_z$ are the in-plane and cross-plane values for a single superlattice grain, while $\kappa_{eff}$ is the value for a bulk polycrystal with randomly oriented grains. Dashed lines: $\kappa_{x,FL}$ and $\kappa_{z,FL}$ are the classical Fourier-Law values for a single superlattice grain, neglecting phonon size effects.**

At large periods in micrometer level, both the in-plane and cross-plane thermal conductivity approach their own Fourier limit (as shown in dashed lines). The Fourier limit for this in-plane arrangement is a parallel combination of two conductances so that

$$\kappa_{x,FL} = \frac{d_1}{d_1+d_2}\kappa_{1,FL} + \frac{d_2}{d_1+d_2}\kappa_{2,FL}\,, \tag{2.19}$$

where $\kappa_{1,FL}$ and $\kappa_{2,FL}$ are the bulk thermal conductivities for layers 1 and 2. In the other direction of cross-plane, the thermal conductivity is a series of two resistances so that

$$\kappa_{z,FL}^{-1} = \frac{d_1}{d_1+d_2}\kappa_{1,FL}^{-1} + \frac{d_2}{d_1+d_2}\kappa_{2,FL}^{-1}\,. \tag{2.20}$$

From the numerical simulation verification in Chapter 2.2.5, we find heat transfer in randomly oriented superlattice can be understood largely as thermal conductances in parallel. The in-plane thermal conductivity of superlattice is important because the heat would leak through the in-plane direction. In Fig. 2.8, the thermal conductivity contrast parameter $r = \kappa_z / \kappa_x$ is within the range between 0.17 to 0.25. This change is relatively small comparing to the scale of *r* we investigated in the FEM simulation in Fig. 2.4. We can also do the sensitivity check using the definition that

$$S_{\kappa_x} = \frac{\kappa_x}{\kappa_{eff}}\frac{\partial \kappa_{eff}}{\partial \kappa_x}\bigg|_{\kappa_z} = \frac{\partial\left[\ln(\kappa_{eff})\right]}{\partial\left[\ln(\kappa_x)\right]}\bigg|_{\kappa_z}\,. \tag{2.21}$$

For the Mityushov-Adamesku averaging model, we find the in-plane sensitivity is

$$S_{\kappa_x} = \frac{14r^2+20r+20}{(r+2)\left(r^2+16r+10\right)} \tag{2.22}$$

Within the range of thermal conductivity contrast parameter $r < 0.25$, the in-plane sensitivity is $S_{\kappa_x} > 0.82$ $\left(\text{and thus } S_{\kappa_z} < 0.18\right)$. Thus, the in-plane thermal conductivity has 4.6 times more sensitivity than the cross-plane thermal conductivity. This means a 10% change of in-plane thermal conductivity would cause 8.2% change of $\kappa_{eff}$; while a 10% change of cross-plane change would only cause 1.8% change of $\kappa_{eff}$. These results suggest controlling the in-plane thermal conductivity $\kappa_x$ is more important than cross-plane thermal conductivity $\kappa_z$, as referring to reducing the total thermal conductivity $\kappa_{eff}$.

### 2.4.2 Effect of Specularity

The specularity dependent thermal conductivity is in Fig. 2.9. The diffuse interface always has lower thermal conductivity, because the rougher surface would scatter phonons more effectively. The thermal conductivity is most sensitive at large specularity regime, especially at $p > 0.8$. In this regime, the thermal conductivity dramatically changes with respect to $p$. For instance, for period of $L$=10 nm, there is a 62% thermal conductivity reduction at $p = 0.8$ comparing to $p = 1$. In addition, it can also be found that the short period $L$ tends to be more sensitive to the specularity. This is because the interface scattering play more role in the short $L$ sample; while for the long $L$ sample, the bulk materials thermal conductivity of PbTe and $Sb_2Te_3$ both contribute more to the total thermal conductivity, which are independent of specularity.

In the limit case of $p = 1$, in both Fig. 2.8 and 2.9, we also find the thermal conductivity is not sufficient to recover the Fourier limit for of $\kappa_{x,FL}$ and $\kappa_{z,FL}$., especially when the period is in the order of nanometer. We think this is because the period is comparable to the mean free path, thus the Fourier limit would not be applied anymore. This effect in both the in-plane[31] and cross-plane[32] directions has also been reported before.

### 2.4.3 Effect of Temperature

Temperature dependent thermal conductivity is shown in Fig. 2.10. The superlattice period is fixed at 10 nm. For the specular interface with $p = 1$, the temperature dependence closely follows the $T^{-1}$ trend. This means the Umklapp scattering in both PbTe and $Sb_2Te_3$ is the main scattering mechanism. In the other limit of $p = 0$, the diffuse interface, the temperature dependence is weaker. The thermal conductivity reduces from 0.378 W/m-K to 0.288 W/m-K over the temperature range of 300 to 500 K. The temperature power law is about $T^{-0.52}$. This means at interface scattering, which is temperature independent, plays important role at $p = 0$.

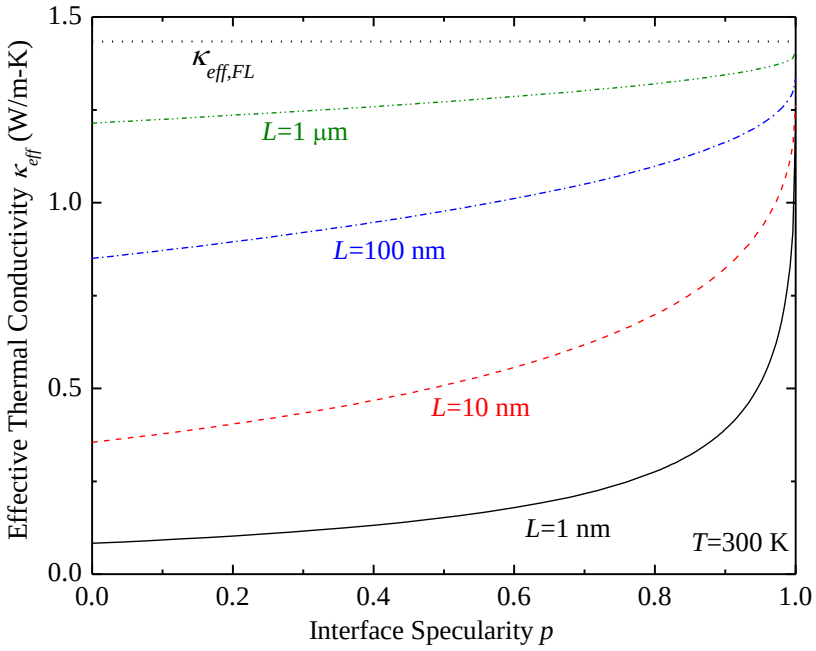


**Figure 2.9 Bulk effective thermal conductivity as a function of specularity for four different periods *L*, for a PbTe-$Sb_2Te_3$ nano-bulk system at *T*=300 K with thickness ratio PbTe : $Sb_2Te_3$ =2:7.**

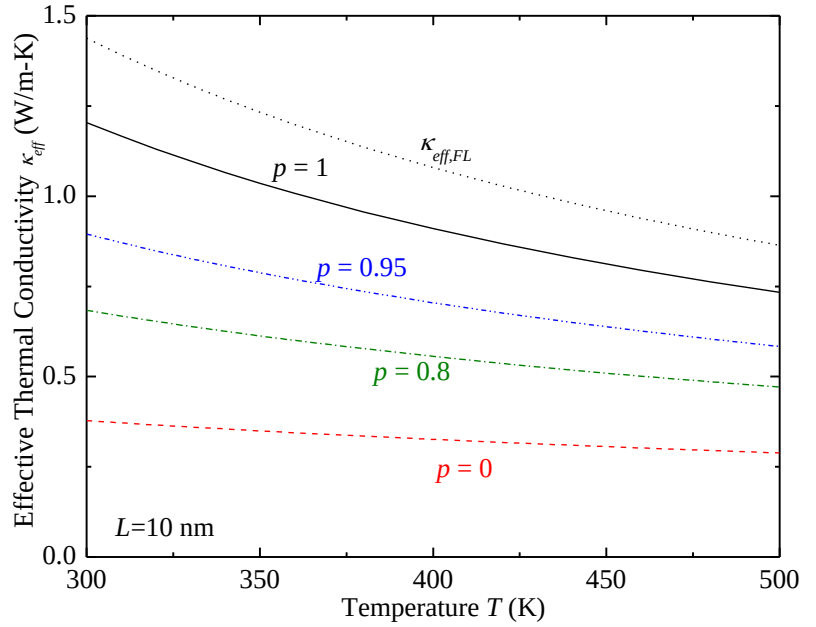


**Figure 2.10 Bulk effective thermal conductivity as a function of temperature for four different values of the specularity *p*, for a PbTe-$Sb_2Te_3$ system with thickness ratio PbTe : $Sb_2Te_3$ =2:7 and fixed period *L*=10 nm. The black dotted line is the bulk classical Fourier law value.**

### 2.4.4 Comparison of Gray vs. Frequency Dependent Modeling.

This subchapter discusses the difference between gray and frequency dependent models. Previous Boltzmann transport equation solutions of the superlattice transport[32, 39] are based on gray media approximation. Here we consider the phonon frequency-dependence and compare the difference in Fig. 2.11. In the long superlattice limit, $L \to \infty$, the interface scattering would be negligible compared to the phonon-phonon Umklapp scattering, so the thermal conductivity recovers the bulk limit for both the gray and frequency dependent models. The specularity effect can also be neglected because of neglecting the interface scattering. In the opposite limit of $L \to 0$, the boundary scattering dominates the scattering process. For the same specularity, the difference between gray and frequency-dependent model also decreases with the reduction of $L$.

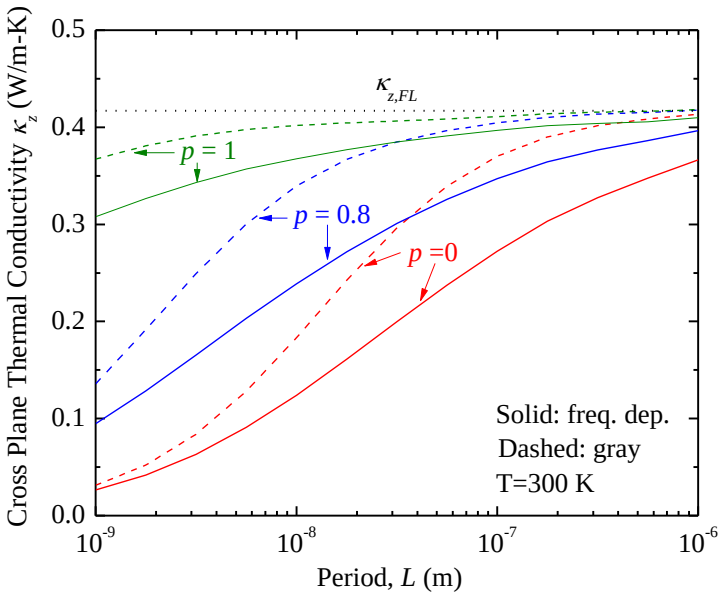


**Figure 2.11 Comparison of present frequency-dependent model (solid lines) and traditional gray media model (dashed lines) for the period-dependence of the cross-plane superlattice thermal conductivity $\kappa_z$. The calculations are for a PbTe-$Sb_2Te_3$ superlattice system at $T$=300 K with thickness ratio PbTe : $Sb_2Te_3$ =2:7.**

In the moderate periods, the difference between the gray media model and frequency dependent model is the largest, as shown in Fig. 2.11, because the former fails to capture the broad distribution of phonon mean free path. Similar phenomenon has also been observed in Si nanowires[59]. For instance, at $p$ = 0 and $L$=200 nm, the reduction of thermal conductivity for gray model only is 6.6%, but 27% for the frequency-dependent model. The frequency-dependent model also has a broader transition regime between the gray limit and small-period limit. This is also caused by the broad phonon distribution of phonon mean free path in the frequency-dependent model. For a superlattice at specific period $L$, phonons with MFPs much larger than $L$ would be affected much more than shorter MFP phonons. Thus, this transition regime would be

broad. For the gray model, all phonons are lumped into a single MFP $\Lambda_{lump}$. When MFP $\Lambda_{lump}$ is comparable to the superlattice period $L$, there would have a sharp transition. Thus, the gray model has narrower distribution than the frequency-dependent model.

## 2.5 Comparison With Experiment

The experiment of materials synthesis and properties measurement are done by our cooperators Dr. Ikeda and Prof. Snyder from Caltech[23]. Samples weighing 15-20 g with overall composition of "$Pb_2Sb_6Te_{11}$" compound ($Pb_{10.5}Sb_{31.6}Te_{57.9}$) were prepared by injection molding with the $20 \times 30 \times 3$ mm$^3$ copper mold. The Ref. 44 describes the details of this method. The samples were cut to the size of $10 \times 10$ mm$^2$ by diamond saw and the surface layer was removed. The final thickness is about 1.5 mm. The samples were annealed under vacuum in fused silica tubes at temperature 573 K for 840 hours. The other samples were annealed at 673 K for 78 h and 150 h, or at 773 K for 1 h and 126 h.

The field emission-scanning electron microscope (Carl Zeiss LEO 1550 VP) equipped with backscattered (BSE) detector was used to measure the microstructure composition. It is found the microstructure is essentially the same as previous results[36]. The inter-lamellar spacing (period) and fraction transformed ($Y$) of the microstructure were analyzed using the image analysis program (Macscope, Mitani Corp.). Details of the method to determine the period is in literature[61]. The analyzed results are listed in Table 2-3.

**Table 2-3 Fraction transformed ($Y$) and inter-lamellar spacing (period) of the samples used for lattice thermal conductivity measurements.**

| Sample ID | Annealing condition | | $Y$ (%) | Period (nm) | |
|---|---|---|---|---|---|
| | $T$ / K | $t$ / h | | Average | Standard deviation |
| 1 | 573 | 840 | 100 | 283 | 76 |
| 2 | 673 | 78 | 99.7 | 536 | 155 |
| | | 150 | 100 | 575 | 153 |
| 3 | 773 | 1 | 88.7 | 544 | 168 |
| | | 126 | 100 | 1591 | 487 |

The van der Pauw method is used to measure the electrical resistivity ($\rho$) as a function of temperature using a current of 10 mA. The magnetic field of ~9500 G was used for Hall coefficient ($R_H$) measurement in the same apparatus forwardly and backwardly. The measured Hall coefficients ($R_H$) were used to calculate the carrier concentration ($n$), by $n = 1/R_H e$, assuming the scattering factor of 1.0 and only one type of carrier. A flash diffusivity technique (LFA457, NETSZCH) is used to measure the thermal diffusivities at 300 K. The thermal conductivities ($\kappa_{tot}$) were evaluated using the relation $\kappa_{tot} = \rho C_P \alpha$, where $\alpha$ is the measured thermal diffusivity, $\rho$ is the measured density, and $C_P$ is the DuLong-Petit heat capacity per unit mass. The electrical thermal conductivity was calculated using the Wiedemann-Franz law, $\kappa_{el} = LT/\rho$, where $L$=2.45 ×

$10^{-8}$ $\Omega K^{-2}$ is the Lorenz number. Thus, the lattice thermal conductivity is obtained by $\kappa_{ph} = \kappa_{tot} - \kappa_{el}$ as shown in Fig. 2.12. The data of $Pb_2Sb_6Te_{11}$ before annealing is also plotted in the figure. The size of a single atomic unit cell of $Pb_2Sb_6Te_{11}$ of 1.4 nm is also used as the equivalent period.

The Fourier limit of both in-plane and cross-plane can be evaluated using the parameters in Table 2-2. With these two limits, the effective thermal conductivity can be obtained using the Mityushov-Adamesku averaging model. We obtained the Fourier limit as $\kappa_{eff,FL}=\kappa_{eff}(L\to\infty)=1.43$ W/m-K. This result is lower than the experimental measurement showing above, for instance $\kappa_{eff}$ is about 3.87 W/m-K for period of $L$=1590 nm PbTe/$Sb_2Te_3$. The measurement also exceed bulk thermal conductivity of PbTe and $Sb_2Te_3$ in both directions. There are two major factors which may have led to this disagreement. One is from the modeling side. The $Sb_2Te_3$ values in Table 2-2 are from theoretical analysis from Ref. [55] rather than direct measurement. The other is from experimental extraction of phonon's contribution. The Wiedemann-Franz law is applied to obtain the electronic thermal conductivity and Lorenz number is assumed known. The Lorenz number is only suitable for degenerate semiconductors with high doping concentration. The measured low Seebeck coefficient (30 μV/K)[36, 37] indicates this degenerate behavior is appropriate, however the carrier concentration observed by Hall effect[62] is still relatively low. Thus, further work needs to be done to verify how well the Wiedemann-Franz law applied here. In addition, the ambipolar effect[29, 63] could also be expected to be significant in these samples. In this effect, the electron and hole pair contribute significant to the thermal conductivity $\kappa$, but not to electrical conductivity $\sigma$. Thus, the measured $\kappa_{ph}$ is actually $\kappa_{ph} + \kappa_{ambipolar}$ , which overestimated $\kappa_{ph}$ by $\kappa_{ambipolar}$.

To reduce the effect of bulk thermal conductivity, we normalized to the theoretical and experimental bulk values, respectively. For the theoretical calculation, the Fourier limit is $\kappa_{eff}(L\to\infty)=\kappa_{eff,FL}$ =1.43 W/m-K. Thus, we normalize the theoretical thermal conductivity by using $\kappa_{eff}(L)/\kappa_{eff}(L\to\infty)$. For the experiment, the maximum period we have is $L$=1590 nm. At this period, the theoretical thermal conductivity is about 88.6% ($p$=0) to 95.8% ($p$=0.95) of the Fourier limit. We choose the average of 92.2% and assume the ratio $\kappa_{eff}(1590)/\kappa_{eff}(\infty)$ for experimental thermal conductivity is the same. Thus, we obtain experimental Fourier limit $\kappa_{eff}(\infty)\approx 4.21$ W/m-K for the normalization.

For the very short period sample, $L$=1.4 nm of metastable $Pb_2Te_6Sb_{11}$ phase, even though the experiment and BTE theory agrees well, we still need to be very cautious to interpret these data. Because at this length scale, the particle assumption of phonons for BTE theory may not be valid any more. The wave effects[64, 65] may be significant in this length scales.

The normalized effective thermal conductivity are shown in Fig. 2.12. The smaller the period, the lower the phonon thermal conductivity. The bound of specularity between $p$ = 0 to $p$ = 1 are also plotted. For the experiment at $L$ = ~500 nm, there has a

sudden change of thermal conductivity which may be caused by different surface interfaces. Even though some of the sample points are outside this bound, the general qualitative trend is still consistent with the period dependence with the rougher interfaces (smaller $p$).

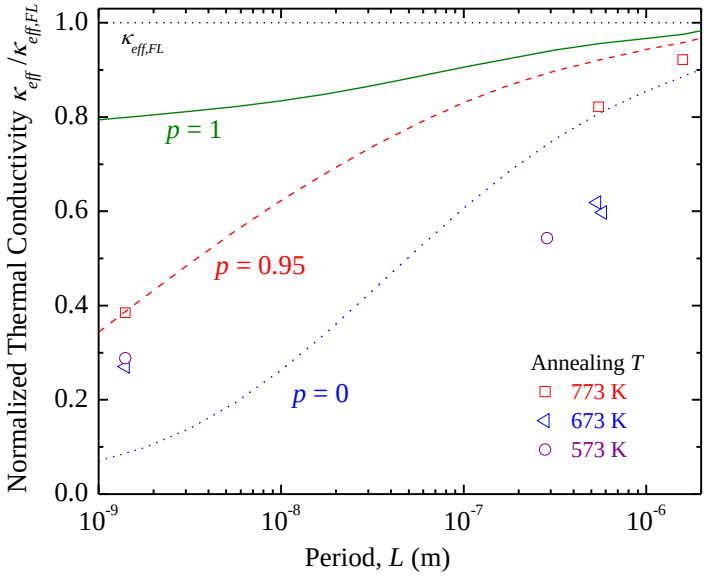


**Figure 2.12 Comparison of normalized theoretical (lines) and measured (points) thermal conductivity at $T$=300 K. The theoretical results are normalized as $\kappa_{eff}(L)$/1.43 W/m-K and the experimental results as $\kappa_{eff}(L)$/4.21 W/m-K.**

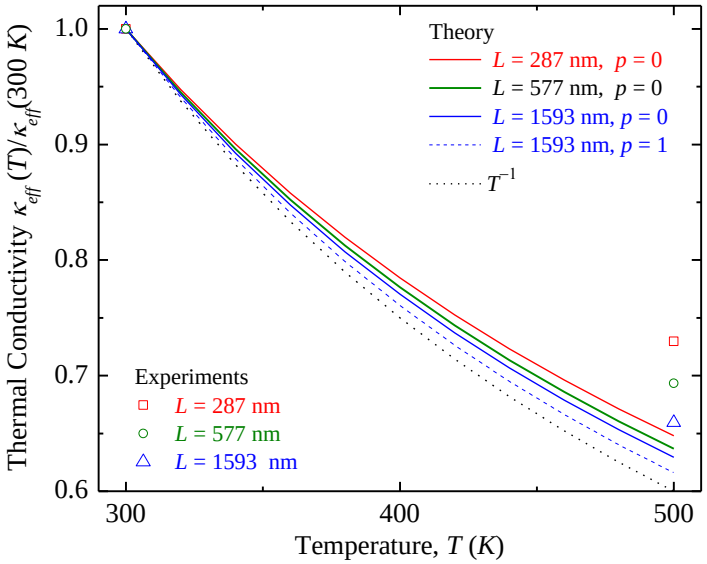


**Figure 2.13 Temperature dependence of normalized effective thermal conductivities for periods of 287 nm, 577 nm and 1590 nm. All thermal conductivities are normalized as $\kappa_{eff}(T)$/ $\kappa_{eff}$(300 $K$).**

Finally, we compare the temperature dependence of modeling and experimental results in Fig. 2.13. The thermal conductivities are normalized to their room temperature values. As expected, when the period and specularity increase, the temperature dependence power law trends approaching the $\kappa \propto T^{-1}$, which is phonon-phonon Umklapp scattering. In the other limit of small period of $L$ =287 nm, the interface scattering, which is temperature independent, plays a more important role. Thus, the temperature dependent power law would be smaller. Experimentally, we have the relationship of $\kappa_{eff} \propto T^{-0.61}$, which has much smaller power law than the Umklapp scattering dominated $T^{-1}$.

## 2.6 Conclusions

Effective thermal conductivity of nano-bulk material made of randomly oriented superlattice grain PbTe/$Sb_2Te_3$ has been investigated by the frequency-dependent Boltzmann transport equation. An average rule based on Mityushov and Adamesku's[40] model has been used and verified by FEM simulations. The sensitivity analysis of in-plane and cross-plane shows the maximum value of ($\kappa_x$, $\kappa_z$) affects the effective thermal conductivity the most in this system.

We extended previous gray model for the cross-plane direction to frequency-dependent model. This treatment captures the broad distribution of phonon mean free paths. In addition, the numerical results also show the in plane thermal conductivity $\kappa_x$ is 4 to 5 times larger than cross-plane thermal conductivity $\kappa_z$. Thus, reducing $\kappa_x$ would be the major focus for reducing the effective thermal conductivity $\kappa_{eff}$ in this PbTe/$Sb_2Te_3$ system.

The modeling results are also compared with experiment after normalizing to the thermal conductivity Fourier limit. The temperature dependent power law indicates the scattering in the samples is between the Umklapp and boundary scattering.

## 2.7 Appendix: Estimating the Sound Velocities of $Sb_2Te_3$

The properties of $Sb_2Te_3$ are investigated using its close counterpart $Bi_2Te_3$, which has been extensively discussed in literature. We evaluate the sound velocities of $Sb_2Te_3$ in this subchapter.

From continuum elasticity, the sound velocity is expressed as $v = \sqrt{C/\rho}$ where $C$ is an elastic stiffness constant and $\rho$ is the mass density. For $Bi_2Te_3$ in the *ab*-plane, the longitudinal sound velocity $v_{sL} = \sqrt{C_{11}/\rho} = 2884$ m/s is calculated. The two transverse sound velocities $v_{sT1}$ =2170 m/s and $v_{sT2}$ =1390 m/s can also be obtained[66]. Similar calculation can also be used in the *c*-axis of $Bi_2Te_3$, which can be obtained that $v_{sL}$ = 2539 m/s and $v_{sT1} = v_{sT2}$ = 1835 m/s. After the averaging rule of the one longitudinal and two

transverse modes, the average sound velocity is $v_{s,avg} = \frac{1}{3}\left(v_{s,L} + v_{s,T1} + v_{s,T2}\right)$. Thus, we can obtain 2147 m/s and 2070 m/s as the average sound velocity along the *a*-plane and *c*-axis directions, respectively.

With the average velocity of $Bi_2Te_3$, we can evaluate its counterpart properties of $Sb_2Te_3$, because they have the exactly the same lattice structure. Since the sound velocity is related to the lattice constant *a*, force constant $\beta$, and total mass of all atoms in one primitive unit cell *M*, by the expression $v_s = a\sqrt{2\beta / M}$ , we can obtain the sound velocity ratio as[30]

$$\frac{v_{s,Sb_2Te_3}}{v_{s,Bi_2Te_3}} = \frac{a_{Sb_2Te_3}}{a_{Bi_2Te_3}}\sqrt{\frac{M_{Bi_2Te_3}}{M_{Sb_2Te_3}}} \,. \tag{2.23}$$

We can obtain the velocity ratio are 1.096 and 1.086 for the *a*-plane and *c*-axis, respectively. Thus, we calculate the sound velocity in these two directions as shown in Table 2-2.

# Chapter 3 Mean Free Path Spectra as a Tool to Understand Thermal Conductivity in Bulk and Nanostructures

## 3.1 Introduction

This chapter is very closely based on our recent publication by Yang and Dames [Phys. Rev. B 87, 035437 (2007)].[67]

The thermal conductivity of a nanostructured material can be greatly reduced compared to its bulk counterpart due to the increased scattering of energy carriers (e.g., phonons, electrons, photons, gas molecules) at the nanostructure surfaces, as in wires[10], films[68, 69], porous[70], and nanocrystalline[71] materials, *etc*. Thermal transport in such nanostructured materials is relevant for a broad range of applications in energy conversion[72], sensors[73, 74], microelectronics[75], and lasers[76]. The key physics that determines the importance of this boundary scattering is the comparison between the characteristic length of the nanostructure and the bulk mean free paths (MFPs) of the energy carriers. Thus it is very helpful to have a detailed quantitative understanding of which bulk MFPs are important in a given material.

The most common formulas for the bulk thermal conductivity are based on kinetic theory, which can be derived from the Boltzmann transport equation in the relaxation time approximation[4, 77]. The polarization- and frequency-dependence of the heat capacity, group velocity, and MFPs are readily accounted for using a summation and integration, respectively. Recently, a new perspective expressing the thermal conductivity integral in terms of MFPs rather than frequency has been developed[18, 20, 25, 78-84]. The main benefit of this MFP spectrum approach is that it quantifies the contribution of every MFP to the bulk thermal conductivity. An equivalent concept is the thermal conductivity accumulation function, which is the normalized integral of this MFP spectrum. The resulting distributions visually and intuitively show which ranges of MFPs are most important for thermal conductivity, information which is not readily apparent in the traditional and complementary approach of plotting the MFPs as functions of frequency.

Although the concept of a MFP spectrum applies to heat conduction by all types of energy carriers, most prior work has focused on calculations for phonons, including MFP distributions for analytical models[18, 79] and numerical results from molecular dynamics (MD) simulations[78] and first principles ($1^{st}$P) calculations based on density functional theory[77, 81-83]. Measurements of portions of the phonon MFP distribution are also beginning to be reported for silicon[20] and several semiconductor alloys[25], although analyzing the raw data requires certain assumptions which, although plausible, have not yet been rigorously proven.

Here, we revisit the concept of the bulk MFP spectrum and show how it is also useful for understanding nanostructures. This paper has three major objectives. First, we rigorously re-derive the expressions for the bulk MFP distribution and thermal

conductivity accumulation function first given by Dames & Chen[18], identifying the major assumptions and restrictions, not all of which were noted previously. Then we derive an integral transform which, given a bulk MFP distribution and a boundary scattering law, yields the thermal conductivity of a nanostructure as a function of its characteristic length. As summarized in Fig. 3.1, this integral equation does not require any explicit knowledge of the carrier's dispersion relation or frequency-dependent scattering laws, and thus represents a quantitative application of the MFP spectrum beyond its more common use for visualizing MFP distributions. Finally, to demonstrate these concepts we present a detailed case study of the phonon thermal conductivity of bulk and nanostructured silicon, revealing major differences among the MFP spectra of three common analytical models (Callaway[85], Holland[86], and Born–von Karman-Slack[18]), an MD simulation[78], and a 1$^{st}$P calculation[82].

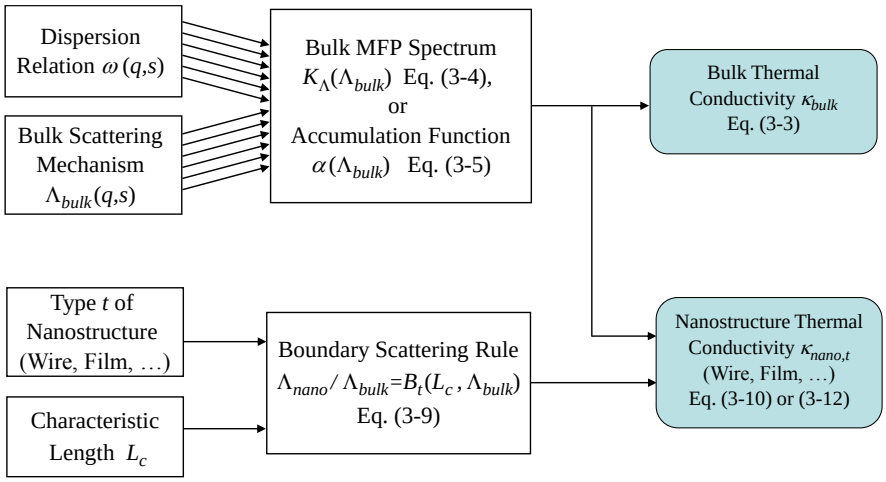


**Figure 3.1 The framework of using a MFP spectrum (or equivalently, accumulation function) to model the thermal conductivity of an isotropic bulk material and a corresponding nanostructure. The multiple arrows at top-left suggest multiple polarizations s. The other variables are defined in the main text.**

## 3.2 Theoretical Framework

### 3.2.1 Bulk MFP Spectrum and Thermal Conductivity Accumulation Function

Our starting point is the kinetic theory integral for the thermal conductivity of an isotropic bulk material,

$$\kappa_{bulk} = \sum_s \int_0^\infty \tfrac{1}{3} C v \Lambda_{bulk} d\omega \,, \tag{3.1}$$

where $C$ is the volumetric specific heat capacity per unit frequency, $v$ is the group velocity, $\Lambda_{bulk}$ is the bulk MFP, $\omega$ is the frequency, and $s$ indexes the polarizations. The most important assumption of this work is that the dispersion relation and bulk MFPs are well-approximated as isotropic. From symmetry considerations this assumption is exact

for gases (*e.g.* molecules, photons, free electrons), as well as electrons and phonons in amorphous materials. In crystalline materials the dispersion relation of electrons and phonons depends on direction and a more general form[77] of Eq. (3.1) is appropriate, even if $\kappa_{bulk}$ itself is isotropic (as in crystals with cubic symmetries). Nevertheless, such dispersion anisotropies are commonly neglected in models of the thermal conductivity that have been shown to agree well with experiments, in cubic crystals as well as non-cubic crystals that are only weakly anisotropic[31, 85-89], and the present work is limited to materials where this isotropic approximation is acceptable. Furthermore, to ensure that the only sub-continuum effects are due to boundary scattering and not ultrafast phenomena, the analysis is restricted to heat transfer problems that are steady, or if unsteady involve transients that are slow compared to the carrier relaxation times $\tau$.

To focus the theoretical framework on the bulk MFPs, we formally change the integration variable from $\omega$ to $\Lambda_{bulk}$, obtaining

$$\kappa_{bulk} = -\sum_s \int_0^\infty \tfrac{1}{3} C v \Lambda_{bulk} \left( \frac{d\Lambda_{bulk}}{d\omega} \right)^{-1} d\Lambda_{bulk} \,. \tag{3.2}$$

The negative sign arises from swapping the limits of integration, because the dominant trend of $d\Lambda_{bulk}/d\omega$ is negative, and the final value of $\kappa_{bulk}$ will still be positive.

Physically, the change of variables in Eq. (3.2) can be understood as changing to a different labeling scheme for the energy carriers. In general, four numbers are required to uniquely specify a carrier, for example, $\{q_x, q_y, q_z, s\}$ or $\{q, \theta, \phi, s\}$, where $\mathbf{q}$ is the wavevector of magnitude $q$ and direction $(\theta, \phi)$. It is common to use the dispersion relation $\omega = \omega(\mathbf{q}, s)$ to change the labeling scheme to $\{\omega, \theta, \phi, s\}$. The change of variables in Eq. (2) is equivalent but instead uses the bulk scattering function $\Lambda_{bulk} = \Lambda_{bulk}(\mathbf{q}, s)$ to get a $\{\Lambda_{bulk}, \theta, \phi, s\}$ scheme. Then, with the key assumption that $\omega(\mathbf{q}, s)$ and $\Lambda_{bulk}(\mathbf{q}, s)$ are approximately isotropic, the labeling scheme reduces to simply $\{\Lambda_{bulk}, s\}$. That is, every energy carrier is uniquely identified by its bulk MFP and polarization branch.

For fixed *s*, often $\Lambda_{bulk}$ is a smooth, monotonically decreasing function of ω. In cases where $\Lambda_{bulk}(\omega, s)$ is not monotonic in ω, the inverting function $\omega(\Lambda_{bulk}, s)$ will be multivalued and there may appear to be an ambiguity in the $\{\Lambda_{bulk}, s\}$ labeling scheme. However this is easily remedied by breaking the offending polarization branch into piecewise monotonic sections and increasing the number of branches in the index list *s* accordingly. This remedy of piecewise integration can also be used to avoid any singularities which arise at points where $\frac{d\Lambda_{bulk}}{d\omega} = 0$.

Returning to Eq. (3.2), because the integrals converge we apply Fubini's theorem to exchange the orders of summation and integration and write

$$\kappa_{bulk} = \int_0^\infty K_\Lambda \, d\Lambda_{bulk} \,, \tag{3.3}$$

where

$$K_\Lambda = -\sum_s \tfrac{1}{3} Cv\Lambda_{bulk}\left(\frac{d\Lambda_{bulk}}{d\omega}\right)^{-1} \tag{3.4}$$

is the thermal conductivity per MFP, with SI units (W/m$^2$-K). This function[18] is known as the MFP distribution or MFP spectrum for the bulk thermal conductivity. By definition, the quantity $K_\Lambda(\Lambda_{bulk})\cdot d\Lambda_{bulk}$ represents the differential thermal conductivity due to those energy carriers with MFPs between $\Lambda_{bulk}$ and $\Lambda_{bulk} + d\Lambda_{bulk}$.

A complementary perspective is the thermal conductivity accumulation function,

$$\alpha(\Lambda_\alpha) = \frac{1}{\kappa_{bulk}} \int_0^{\Lambda_\alpha} K_\Lambda d\Lambda_{bulk}\ , \tag{3.5}$$

which represents the fraction of the total thermal conductivity due to carriers with MFPs less than $\Lambda_\alpha$. Thus, the range $\Lambda_{0.1} < \Lambda_{bulk} < \Lambda_{0.9}$, analogous to the 10% - 90% risetime of a signal on an oscilloscope, is one useful guideline to the range of bulk MFPs that are important for heat conduction in a given system: 80% of the thermal conductivity is carried by particles with MFPs in this range, with only 10% carried by MFPs shorter than $\Lambda_{0.1}$, and another 10% carried by MFPs longer than $\Lambda_{0.9}$.

Equations (3.4) and (3.5) are the first major results of this paper. These equations quantify the range of MFPs that contribute to heat conduction, which traditionally was described mainly through a single lumped "gray" or effective MFP,

$$\Lambda_{gray} = \kappa_{bulk} \Big/ \left(\sum_s \int_0^\infty \tfrac{1}{3} Cvd\omega\right). \tag{3.6}$$

This is equivalent to a MFP distribution that is a Dirac delta function with weight $\kappa_{bulk}$ centered on $\Lambda_{gray}$. Such a gray MFP model is a good approximation in systems where the real MFP distribution is narrow, including ideal gases[90] and free electron gases. However, in other systems with strongly frequency-dependent scattering, the distributions can be quite broad. For example, as we shall discuss further in Section III, phonons in semiconductor crystals and alloys are generally believed to have MFP distributions typically spanning two or more orders of magnitude from $\Lambda_{0.1}$ to $\Lambda_{0.9}$ [18, 20, 25, 78, 79, 82, 83].

### 3.2.2 An Integral Transform to Relate Bulk and Nanostructures

We now shift attention from bulk to nanostructures, and make the common assumption that wave confinement effects are negligible. This is generally appropriate as long as the structure's characteristic length $L_c$ is much larger than the thermal wavelengths of the energy carriers[18, 91, 92] and there is sufficient roughness or disorder to wash out any coherence effects. Thus, the group velocity and spectral heat capacity in the nanostructure are identical to those in bulk, so the only effect of the nanostructuring is to reduce the effective MFP $\Lambda_{nano}$ by scattering at boundaries and interfaces. Thus the nanostructure thermal conductivity is commonly written[18, 45, 69, 71, 93]

$$\kappa_{nano,t} = \sum_s \int_0^\infty \tfrac{1}{3} C v \Lambda_{nano} d\omega \tag{3.7}$$

where $\Lambda_{nano}(\omega, s) < \Lambda_{bulk}(\omega, s)$ and the subscript *t* indicates the "type" of geometry (such as a wire, film, *etc*.). We again change variables from $\omega$ to $\Lambda_{bulk}$ and rearrange to obtain

$$\kappa_{nano,t} = \int_0^\infty \left[ -\sum_s \tfrac{1}{3} C v \Lambda_{bulk} \left( \frac{d\Lambda_{bulk}}{d\omega} \right)^{-1} \right] \frac{\Lambda_{nano}}{\Lambda_{bulk}} d\Lambda_{bulk} , \tag{3.8}$$

where the term in square brackets is exactly the bulk MFP spectrum $K_\Lambda$ from Eq. (3.4), an important feature we shall return to shortly. Recall that physically this change of variables from $\omega$ to $\Lambda_{bulk}$ is equivalent to choosing to label each carrier by its polarization and *bulk* MFP, even though now that carrier's MFP in the nanostructure is reduced to $\Lambda_{nano}$.

There is a deep physical reason for choosing $\Lambda_{bulk}$ as the independent variable in Eq. (3.8), rather than $\tau_{bulk}$, $\omega$, $q$, wavelength $\lambda$, or indeed any other quantity. The key is in the functional dependencies of the effective MFP $\Lambda_{nano}$. $\Lambda_{nano}$ obviously must depend on $L_c$ and the type of nanostructure (wire, film, *etc*.). More importantly, we recognize the very general result that $\Lambda_{nano}$ transitions between bulk and strongly confined behaviors depending primarily on the comparison between $L_c$ and $\Lambda_{bulk}$. Therefore, the simplest, and also very common, situation is that $\Lambda_{nano}$ is a function exclusively of $L_c$ and $\Lambda_{bulk}$. In this case, from basic considerations of dimensional analysis the functional relationship between these three length scales must be expressible in the form

$$\frac{\Lambda_{nano}}{\Lambda_{bulk}} = B_t\left(\tfrac{\Lambda_{bulk}}{L_c}\right) = B_t(Kn). \tag{3.9}$$

Here $B_t$ is some function to be determined that depends only on the type of nanostructure and on the *ratio* $\Lambda_{bulk}/L_c$. Note that this reasoning has nothing to do with Matthiessen's rule, and that the ratio $\Lambda_{bulk}/L_c$ is the Knudsen number, *Kn*. Examples of the $B_t\left(\tfrac{\Lambda_{bulk}}{L_c}\right)$ for both thin film and wire are shown in Fig. 3.2.

Thus, out of all possible quantities to label an energy carrier, it is uniquely $\Lambda_{bulk}$ that has the strongest physical connection to the processes of boundary scattering. Indeed, for a wide variety of geometries the most common boundary scattering laws for $\Lambda_{nano}$ can be written in the form of Eq. (3.9) without any other explicit dependence on polarization, group velocity, frequency, *etc*. Examples include wires of arbitrary cross section[94-96], thin films both in-plane and cross-plane[97-100], porous media with arbitrary pore shapes and distributions[79], and simple models of grain boundary scattering.[16, 71, 101] Equation (9) will also result for the combined effect of scattering by bulk and surface mechanisms in single-phase structures with arbitrarily complicated geometries and with surface roughness, as long as all of the important energy carriers experience the same specularity, *p*, representing the probability of specular scattering[102]. Such a constant *p* approximation has been used for wires[102] and thin films[97, 98].

The most common breakdown of the functional form of Eq. (3.9) is when *p* varies substantially with the wavelength of the important energy carriers, as in the transition between specular and diffuse scattering for a surface of roughness δ comparable to the thermal wavelengths[71, 102, 103]. In this case Eq. (3.9) could be generalized to $B_t(Kn, \frac{\lambda}{\delta})$, although such scattering laws would no longer be compatible with the analysis in the remainder of this section. If $\delta$ is either much smaller or much greater than the thermal wavelengths, then *p* should be a constant for all important energy carriers, the wave nature again should be negligible, and the form of Eq. (3.9) recovered.

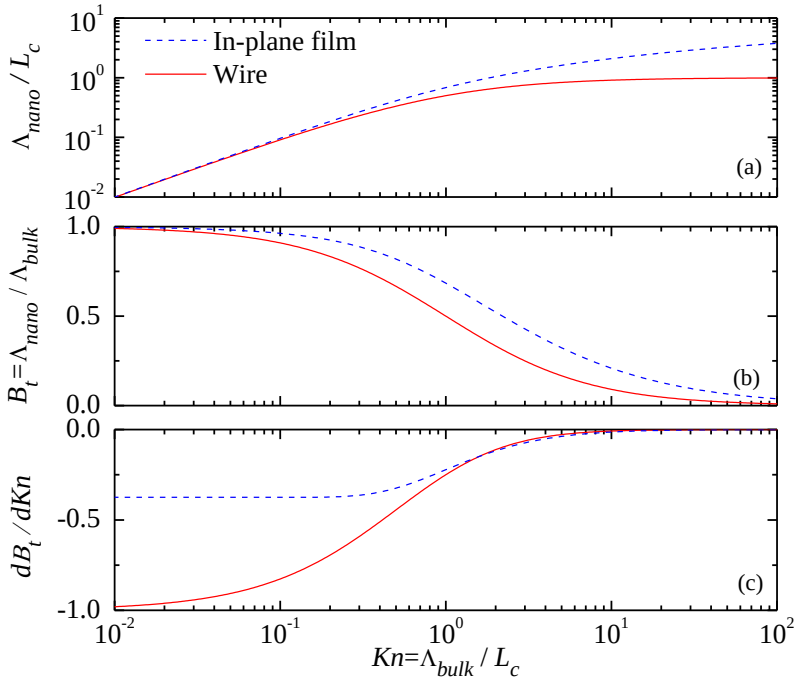


**Figure 3.2 Two examples of the effect of Knudsen number on (a) $\Lambda_{nano}$, (b) the integral transform kernel $B_t$, and (c) its derivative $\frac{dB_t}{d\Lambda_{bulk}}$. Quantities are non-dimensionalized by the nanostructure's characteristic length $L_c$, taken as the nanowire diameter and film thickness, both of which are assumed diffuse.**

Proceeding, we restrict the analysis to those many systems whose boundary scattering laws can be expressed in the form of Eq. (3.9), and assume the function $B_t(Kn)$ is known. In this case the nanostructure thermal conductivity in Eq. (3.8) becomes

$$\kappa_{nano,t} = \int_0^\infty K_\Lambda B_t d\Lambda_{bulk} . \tag{3.10}$$

Equation (3.10) has a counterpart in terms of the accumulation function. Integrating Eq. (3.10) by parts and using Eq. (5) gives

$$\kappa_{nano,t} = \kappa_{bulk}\left[\alpha(\Lambda_{bulk})B_t\right]_{\Lambda_{bulk}=0}^{\Lambda_{bulk}=\infty} - \kappa_{bulk}\int_{\Lambda_{bulk}=0}^{\Lambda_{bulk}=\infty}\alpha(\Lambda_{bulk})dB_t . \tag{3.11}$$

From the definition of accumulation, $\alpha(\Lambda_{bulk})=0$ when $\Lambda_{bulk} = 0$. Furthermore, $B_t \rightarrow 0$ as $\Lambda_{bulk} \rightarrow \infty$ because in this limit boundary scattering always dominates regardless of the type of geometry, causing $\Lambda_{nano} << \Lambda_{bulk}$ . Thus Eq. (11) simplifies to

$$\kappa_{nano,t} = -\kappa_{bulk} \int_0^\infty \alpha\left(\Lambda_{bulk}\right) \frac{dB_t}{d\Lambda_{bulk}} d\Lambda_{bulk} \,. \tag{3.12}$$

As noted above, in the present work the boundary scattering function $B_t\left(\Lambda_{bulk}, L_c\right)$ is considered known[71, 94, 96, 97]with two specific examples given later in Section III(C) and (D) for a wire and film, respectively. As with Eq. (2), the negative sign in Eq. (12) will be cancelled because the dominant trend of $B_t(\Lambda_{bulk})$ at constant $L_c$ must be of negative $\frac{dB_t}{d\Lambda_{bulk}}$. Two examples of this trend are shown in Fig. 3.2 for the simple cases of heat conduction along a round wire and in the plane of a film. The exact expressions used for $B_t$ are given later in Eqs. (16) and (17). To obtain a consistent nondimensional representation of $\frac{dB_t}{d\Lambda_{bulk}}$ we normalize $\Lambda_{\text{bulk}}$ in the denominator by $L_c$, yielding $\frac{dB_t}{dK_n}$. In the limit of very large structures, $L_c >> \Lambda_{bulk}$, it is obvious that boundary scattering is negligible and thus $\Lambda_{nano} \rightarrow \Lambda_{bulk}$, so $B_t \rightarrow 1$. Conversely, in the limit of very strong boundary scattering, $L_c << \Lambda_{bulk}$, clearly $\Lambda_{nano} << \Lambda_{bulk}$ and thus $B_t$ must asymptote towards zero. Therefore, $B_t$ very generally decreases from 1 to 0 with increasing $\Lambda_{bulk}$, confirming that the dominant behavior of $\frac{dB_t}{d\Lambda_{bulk}}$ is negative.

Equations (10) and (12) are the second major result of this paper. We recognize both as Fredholm integral equations of the first kind. Equation (10) transforms the bulk MFP spectrum $K_\Lambda(\Lambda_{bulk})$ to the size-dependent nanostructure conductivity $\kappa_{nano,t}(L_c)$ by means of the kernel $B_t$. Similarly, Eq. (12) transforms the bulk accumulation function $\alpha(\Lambda_{bulk})$ to $\kappa_{nano,t}(L_c)$ using the kernel $\frac{dB_t}{d\Lambda_{bulk}}$.

The flowchart in Fig. 3.1 summarizes this approach. We emphasize that the theoretical development so far is general and applies to all types of energy carriers, provided their bulk dispersion relations and bulk MFPs are approximately isotropic. As a concrete example of the utility of this approach, consider the phonon thermal conductivity of silicon. For bulk silicon some of the most accurate models are based on 1$^{st}$P calculations[77, 82, 83] or MD simulations[78] and thus lack any compact analytical form. After making the isotropic approximation, the traditional way to extend such models to predict the thermal conductivity of, for example, a nanowire is based on Eq. (7). This requires detailed numerical information about *twelve* functions from the bulk model: the six dispersion branches $\omega(q,s)$ and six scattering laws $\Lambda_{bulk}(\omega,s)$. Here the key advantage of writing the kinetic theory integral in terms of MFPs rather than $\omega$ becomes apparent: As shown in Fig. 3.1, Eqs. (10) or (12) require only a *single* numerical function from the bulk model, namely its MFP spectrum $K_\Lambda$ or, equivalently, its accumulation function $\alpha$. The information from the six dispersion branches and six scattering laws is not lost, but rather is collapsed into the bulk MFP spectrum [recall Eq. (4)] in exactly the

form needed for the nanostructure calculation. Thus, if we can obtain the MFP spectrum or accumulation function of a bulk material – whether from an analytical solution[18, 79], numerical model[77, 78, 81-83], or experiments[20, 25] – given any boundary scattering law Eq. (9) we can also evaluate the thermal conductivity of the corresponding nanostructure.

### 3.2.3 Comparison of MFP Spectrum and Accumulation Function Approaches

We have seen that $K_\Lambda$ and $\alpha$ are both equally valid for visualizing a bulk MFP spectrum as well as transforming it to a nanostructure's thermal conductivity using Eqs. (10) or (12). However, there are certain practical reasons to prefer $\alpha$ and Eq. (12). First, for distributions that span more than one order of magnitude in $\Lambda_{bulk}$, the accumulation function is far more convenient for visualizing the breadth of the distribution because the ordinate is expressed directly as a fraction of the total thermal conductivity. On the other hand, plots of $K_\Lambda$ require mentally integrating the area under the curve, which is prone to misunderstanding if a logarithmic abscissa axis is required to cover a large range of $\Lambda_{bulk}$.

The second reason why Eq. (12) may be preferred is related to numerical accuracy. Note that Eq. (12) involves the integral of $K_\Lambda$ (namely, $\alpha$) and the derivative of $B_t$; while Eq. (10) involves the derivative of $\alpha$ (namely, $K_\Lambda$) and the integral of $\frac{dB_t}{d\Lambda_{bulk}}$. Note also that the current numerical formulations[78, 79, 81-83] and experimental estimates[20, 25] of the MFP distribution arise most fundamentally from an accumulation perspective, $\alpha(\Lambda_{bulk})$, and thus the numerical differentiation to generate $K_\Lambda$ is expected to introduce some numerical noise. On the other hand, the expressions for $B_t$ are always analytical, so generating $\frac{dB_t}{d\Lambda_{bulk}}$ should not introduce any additional noise. Therefore, for numerical reasons the form of Eq. (12) is expected to be preferable to Eq. (10).

### 3.2.4 Gray Approximation

The gray model is a common simple approximation where at any given temperature the bulk MFPs are all assumed to take the same "gray" value, $\Lambda_{gr}$. Thus the thermal conductivity spectrum is a delta function, $K_\Lambda=\kappa_{bulk}\delta(\Lambda_{bulk}-\Lambda_{gr})$ and the accumulation function $\alpha$ is a Heaviside step function, $\alpha=H(\Lambda_{bulk}-\Lambda_{gr})$. Applying either Eq. (10) or Eq. (12) shows that this leads to the nanostructure thermal conductivity

$$\kappa_{nano,gr} = \kappa_{bulk} B_t\left(\frac{\Lambda_{gr}}{L_c}\right) = \kappa_{bulk} B_t\left(Kn_{gr}\right), \tag{3.13}$$

where $Kn_{gr}$ is the Knudsen number of the gray medium.

## 3.3 Case Study: Phonons in Si

In this section we apply the above concepts to interpret six models of the phonon thermal conductivity of silicon: three analytical, one MD[78], one 1$^{st}$P [82], and a simple gray model for comparison. For the analytical models we use three of the most common: Callaway[85, 88, 93, 104], Holland[86], and Born-von Karman-Slack (BvKS)[31, 45].

Details of our implementation of these models are given in Chapter 3.5, including a modification of the Callaway model with an Umklapp scattering law appropriate for all temperatures. Below we present the bulk MFP spectra of these six models, and apply the integral transform of Eq. (12) to calculate the corresponding size-dependent thermal conductivity of nanowires and thin films.

### 3.3.1 Temperature Dependence of Bulk and Nanowire Thermal Conductivity

For consistency we optimize the three analytical models to the same experimental data set for bulk silicon, from Holland[86, 105]. Thus the fit parameters for our Holland model are identical to those given in the original work[86], while the parameters for our Callaway and BvKS models are given in the Chapter 3.5. As shown in Fig. 3.3, the three models all fit the experimental data very well. To quantify this agreement we calculate the relative error between each model ($\kappa_{\text{model}}$) and experiment ($\kappa_{exp}$) in a root-mean-square (*rms*) sense:

$$\varepsilon = \sqrt{\frac{1}{n}\sum_{i=1}^{n}\left(\frac{\kappa_{\text{model}} - \kappa_{\text{exp}}}{\kappa_{\text{exp}}}\right)^2}, \qquad (3.14)$$

where $n$ is the number of experimental data points. As shown in Table 3-1, after optimizing their parameters the rms errors of these three bulk models are all less than 10%, very good agreement considering they span 2.5 - 3 orders of magnitude in $\kappa$ and $T$.

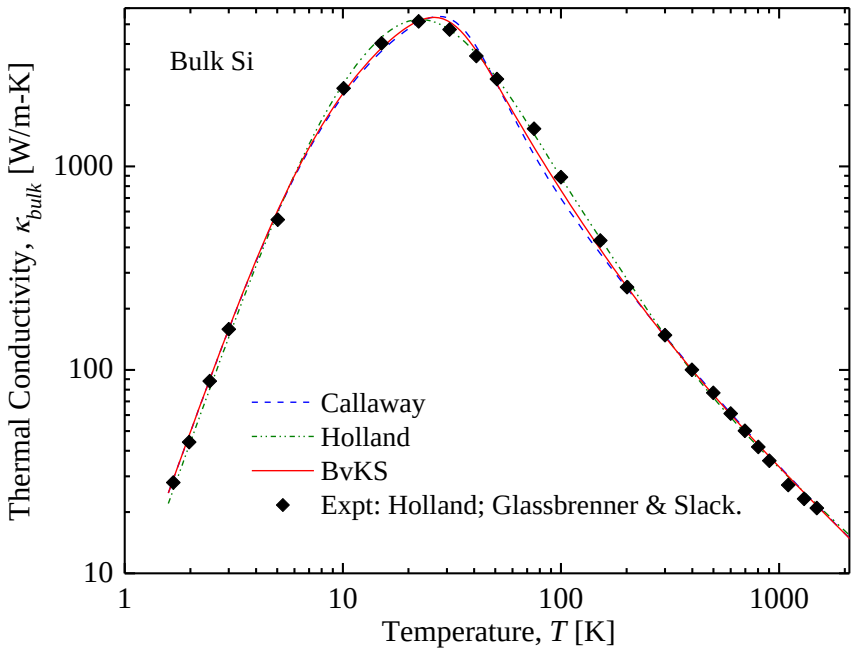


**Figure 3.3 Comparison between three analytical models (lines) and experiment[86, 105] (points) for the thermal conductivity of bulk silicon.**

Even though these models can be tuned to agree closely with each other and with experiments for bulk, the models' internal physical assumptions about $C$, $v$, and $\Lambda_{bulk}$ can

be quite different. This begins to become apparent by comparing the three models' predictions for $\kappa_{nano}(T)$ of a 115-nm-diameter Si nanowire[10], which tests the models' assumptions about $\Lambda_{bulk}$ while leaving $C$ and $v$ unchanged. The calculation combines Eq. (3.12) with the boundary scattering rule given later in Eq. (3.16).

As shown in Fig. 3.4 and summarized in Table 3-1, for this nanowire the BvKS model agrees better with the measurements of Li *et al*. [10] than do the gray and other analytical models. Figure 4 also reveals other insights. For example, for nanowires at $T$ above around 100 K the prediction of the modified Callaway model is substantially higher than that of the other models and the experiments. This is because the Callaway model's Debye dispersion overestimates the average phonon group velocities at moderate and large $\omega$. However, as shown in Fig. 3.3 the Callaway model still fits $\kappa_{bulk}(T)$ very well. This is accomplished by using overly-small $\Lambda_{bulk}$ to compensate for the overly-large $Cv$ at moderate and high $T$. This is also evident in the comparison of cutoff MFPs between the BvKS and Callaway models in Table 3-1, and will be discussed further below. Thus, because at most $T$ the Callaway model results in $\Lambda_{bulk}$ that are too small, when applied to a nanostructure the Callaway model is too insensitive to further reductions in $\Lambda_{nano}$ by boundary scattering, causing it to overpredict $\kappa_{nano}$ for a given $L_c$.

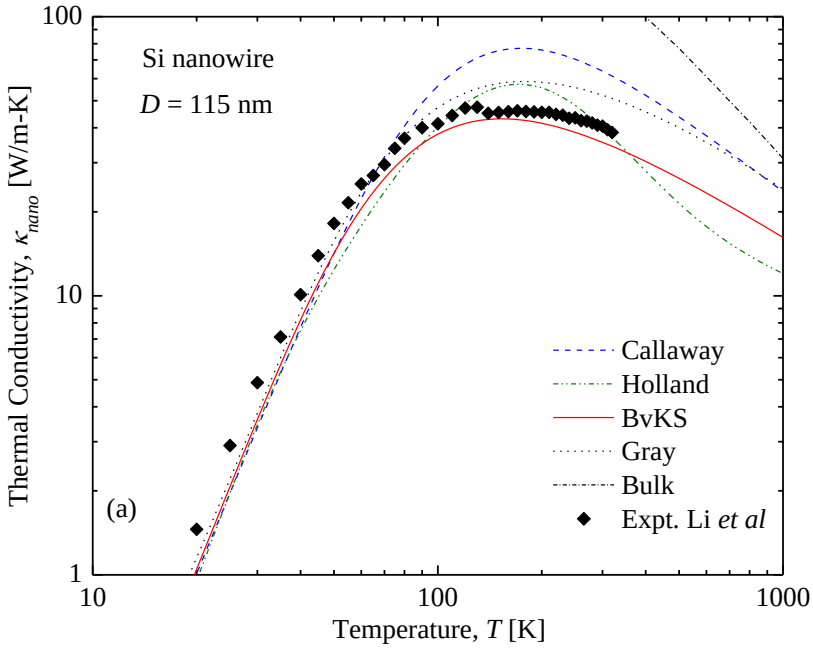


**Figure 3.4 Comparison between models and experiment [Li *et al.*[10]] for the thermal conductivity of a silicon nanowire of diameter 115 nm. The bulk data are from Refs. [86] and [105].**

**Table 3-1 Key parameters for the six models of bulk Si. Details for the three analytical models are given in the Chapter 3.5. The *rms* errors refer to the fits in Figs. (3) and (4). The cutoff MFPs are defined in Eq. (5) and are evident graphically in Fig. 3.6(a). The MD data is from Henry and Chen[78], the 1st P data was provided by Esfarjani[106] at 300 K using the same methods as Ref. [82],**

**and the gray MFP is calculated from Eq. (6) using a BvK dispersion. Rms errors were not evaluated for the MD and 1stP models because their temperature dependence was not available.**

| | rms errors in $\kappa(T)$, $\varepsilon$ [%] | | Cutoff MFPs at 300 K, $\Lambda_\alpha$ [nm] | | | |
|---|---|---|---|---|---|---|
| | Bulk | 115 nm nanowire | $\Lambda_{0.1}$ | $\Lambda_{0.5}$ | $\Lambda_{0.9}$ | "Bandwidth" $\Lambda_{0.9}/\Lambda_{0.1}$ |
| Callaway (modified) | 9.2 | 50 | 30.1 | 134 | 3,530 | 117 |
| Holland | 5.8 | 20 | 24.4 | 343 | 380 | 15.6 |
| BvKS | 6.5 | 15 | 79.3 | 532 | 14 000 | 177 |
| MD[a] | - | - | 41.6 | 335 | 15 700 | 376 |
| 1stP[b] | - | - | 42.8 | 547 | >6 580 | >154 |
| Gray | 0 | 23 | 205 | 205 | 205 | 1 |

### 3.3.2 Bulk MFP Spectra and Accumulation Functions

To quantify the different models' internal assumptions about $\Lambda_{bulk}$, we calculated their bulk MFP spectra and accumulation functions using Eqs. (4) and (5), shown in Fig. 3.5 (a) and (b), respectively. For comparison, this figure also shows MFP spectra from MD calculations by Henry & Chen[78] and from 1stP calculations by Esfarjani[106] at 300 K, using the same 1stP method as in Ref. [82] at 277 K. It is clear from Fig. 3.5(b) that the MFP spectra for several of the models extend far beyond 1 μm, so this broad range is better visualized on the logarithmic MFP scale of Fig. 3.6 at (a) 300 K and (b) 1000 K. The gray MFPs were calculated using the BvKS model and Eq. (6), yielding $\Lambda_{gr}$=205 nm at 300 K and 44 nm at 1000 K. This gray MFP at 300 K is consistent with other gray calculations for Si [32, 107] which obtain values in the range from 260 to 300 nm. Figure 6 also shows how the MFP spectra are shifted towards shorter $\Lambda_{bulk}$ at higher $T$, consistent with the increase in the phonon population (i.e., $\Lambda_{umklapp} \propto T^{-1}$, for $T$ near and above $T_{Debye}$.)

Figures 3.5 and 3.6 reveal striking differences between the various MFP spectra. The models can be roughly grouped into those with broad distributions and those with tight distributions. The first group comprises the Callaway, BvKS, MD, and 1stP models, whose distributions all span more than two orders of magnitude in "bandwidth" from $\Lambda_{0.1}$ to $\Lambda_{0.9}$ (see also Table 3-1). Within this group the Callaway model places more emphasis than the other models do on short MFPs. An important feature of these models is their "long tails": a substantial portion of the heat in bulk is conducted by MFPs much longer than the gray estimate of 205 nm. Specifically, as summarized in Table 3-2, at 300 K bulk MFPs larger than 1 μm account for 19% of the heat conduction in the Callaway model, 31% in the MD results of Ref. [78], 39% in the BvKS model, and 46% of the heat in 1stP results of Ref. [106]. Even bulk MFPs longer than 10 μm may not be completely negligible: the BvKS and MD calculations both attribute 12% of the conduction to such long MFPs. The 1stP distribution likely also would assign over 10% of the heat conduction to MFPs larger than 10 μm, though the exact value of $\alpha$ at 10 μm is not available because that calculation stopped at 6.58 μm (found to correspond to $\Lambda_{0.86}$). If the 1stP calculation for the long-MFP tail is assumed to follow a simple scattering law

of the form $\Lambda_{bulk} \propto \omega^{-n}$ with known $n$, an analytical extrapolation function is available (Chapter 3.6).

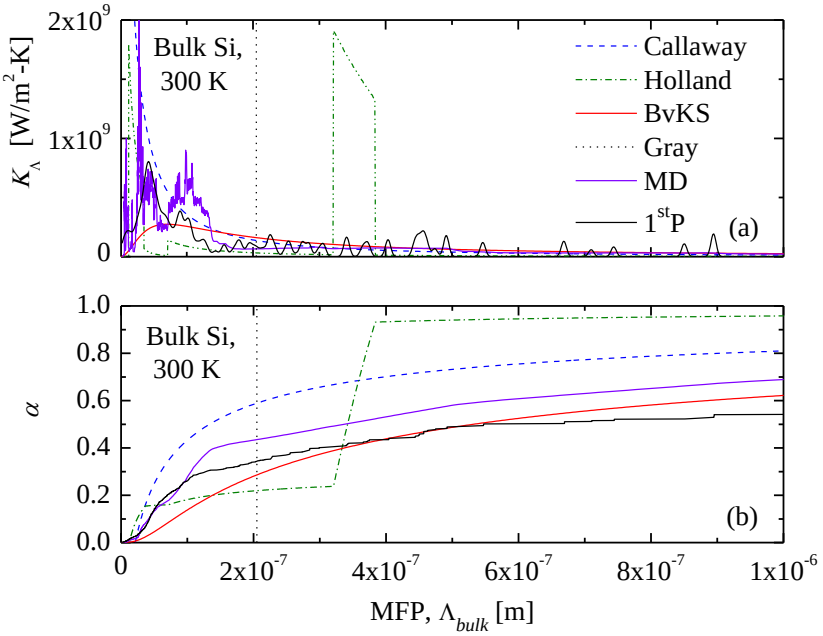


**Figure 3.5 (a) MFP spectra and (b) accumulation functions according to the six models described in the main text. The MD calculation is from Henry & Chen[78] and the 1stP calculation is from Esfarjani *et al.*[82],[106]**

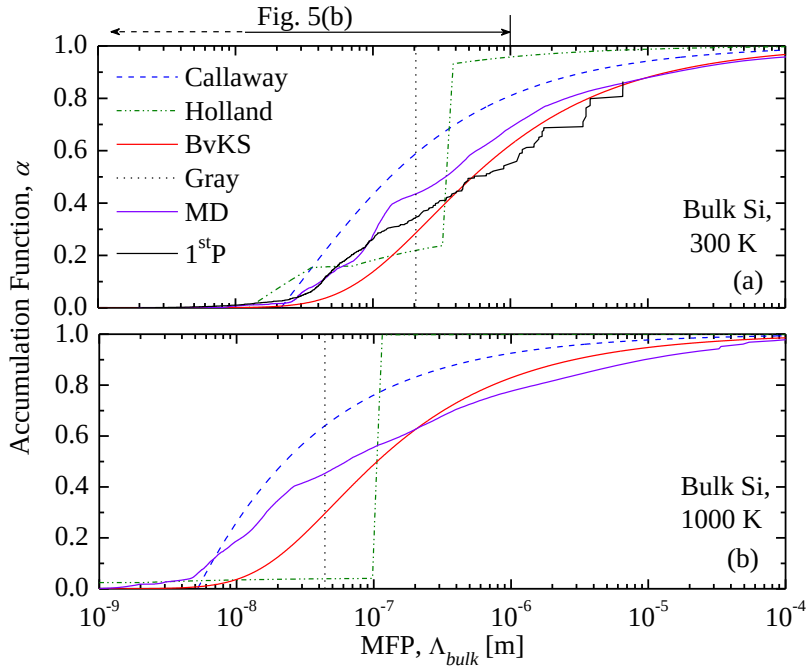


**Figure 3.6 Thermal conductivity accumulation functions for various models at (a) 300 K and (b) 1000 K, using a logarithmic MFP scale. (a) represents a superset of Fig. 3.5(b). See also Table 3-2. The**

**MD calculation is from Henry & Chen[78] and the 1st P calculation is from Esfarjani *et al*.,[82],[106] although the 1st P data was only available at 300 K and $\Lambda_{bulk} \leq 6.58$ μm.**

The second group of models, with tight distributions, comprises the gray and Holland models. At 300 K in the Holland model of Si over 68% of the heat is carried by high frequency TA phonons, within the very narrow range of MFPs from 321 nm to 385 nm. The Holland distribution is even tighter at 1000 K as shown in Fig. 3.6(b), with more than 95% of the thermal conductivity contributed by phonons with MFPs from 98 nm to 116 nm, very much like a gray model.

**Table 3-2 Fraction of thermal conductivity carried by phonons with MFPs longer than three selected values of $\Lambda_{bulk}$, in bulk Si at 300 K. These points are a subset of Fig. 3.6(a). N/A = not available.**

| Model | $1 - \alpha(\Lambda_{bulk})$, (%) | | |
|---|---|---|---|
| | $\Lambda_{bulk}$= 0.1 μm | $\Lambda_{bulk}$=1 μm | $\Lambda_{bulk}$=10 μm |
| Callaway (modified) | 57 | 19 | 5.8 |
| Holland | 82 | 5.6 | 2.3 |
| BvKS | 86 | 39 | 12 |
| MD | 72 | 31 | 12 |
| 1st P | 74 | 46 | N/A |
| Gray | 100 | 0 | 0 |

Among all six models presented here, considering their greater sophistication it is reasonable to expect that the MD[78] and 1st P[82, 106] models should be the best approximations of real Si. It is noteworthy that these two accumulation functions are also consistent with results from another first principles calculation recently reported by Li *et al*.[83], which found $\Lambda_{0.1}$=50 nm and $\Lambda_{0.9}$=13,000 nm for Si at 300 K. Among the other four models presented here, Tables 3-1 and 3-2 and Figs. 5 and 6 show that the BvKS results are closest to those from the MD and 1st P calculations, suggesting that among simple models the BvKS model should be more accurate than the gray, Holland, and modified Callaway models.

### 3.3.3 Diameter Dependence of Thermal Conductivity for a Nanowire

We now use the integral transform of Eq. (12) to calculate the thermal conductivity of nanowires according to the various bulk accumulation functions presented above in Fig 6(a). For the geometry function $B_{wire}$, the exact analytical solution of the Boltzmann transport equation in the relaxation time approximation has been given by Dingle[96]. Dingle's result indeed is of the form of Eq. (9) making it appropriate for this framework, but here for convenience we use a more compact analytical expression for a diffuse cylindrical wire based on Matthiessen's rule,

$$\Lambda_{nano}^{-1} = \Lambda_{bulk}^{-1} + D^{-1}. \tag{3.15}$$

It is readily shown that the errors in this approximation are never more than 6% compared to the exact result from Dingle[96]. Thus, for a diffuse nanowire Eq. (9) becomes

$$B_{wire}(Kn) = (1 + Kn)^{-1}, \tag{3.16}$$

where the Knudsen number is $Kn = \Lambda_{bulk}/D$.

Although the nanowire thermal conductivity for the gray and analytical (Holland, BvKS, and modified Callaway) models could readily be calculated using the traditional integral over frequency, Eq. (7), here we use the integral transform, Eq. (12). As is suggested in Fig. 3.1, we emphasize that the traditional approach of Eq. (7) requires knowledge of 12 functions from the bulk model (6 dispersion relations + 6 MFP functions, although the contribution of the optical modes' 3 + 3 functions is often negligible). On the other hand, the strength of Eq. (12) is that it requires only one function (the accumulation function, or equivalently the MFP spectrum), and thus we can proceed without any explicit knowledge of the dispersion relation or frequency-dependent MFPs that are built into the MD[78] or 1$^{st}$P results[82, 106] for $\alpha$.

Figure 3.7 shows the calculated nanowire thermal conductivities at 300 K, normalized to the bulk thermal conductivity of 148 W/m-K[86]. The accumulation function from Esfarjani *et al.*[82, 106]. was only available for MFPs ≤ 6.58 μm, at which point $\alpha = 0.86$, whereas Eq. (12) requires integration out to $\Lambda bulk = \infty$. Therefore, we evaluated $\kappa nano(D)$ for both bounding limits, where for all $\Lambda bulk > 6.58$ μm $\alpha$ either jumps immediately to 1 or remains constant at 0.86. For clarity Fig. 3.7 shows only the average of these two bounds. For this 1stP result, the difference between the plotted curve and either bound is less than 0.8% of $\kappa bulk$ for all $D \leq 1$ μm, and never exceeds 7% even for $D \to \infty$.

Figure 3.7 also shows that the transition from bulk to strong boundary scattering behavior spans a larger range of *D* for the Callaway, BvKS, MD, and 1$^{st}$P models, as compared to the other two models. This is because these four models all have similarly broad accumulation functions as seen from Table 3-1 and Fig. 3.5. The Callaway curve in Fig. 3.7 is shifted to smaller *D* than the BvKS, MD, and 1$^{st}$P calculations, because the Callaway model places more emphasis on shorter MFPs (Figs. 5 and 6). On the other hand, the Holland and gray models show a steeper transition from bulk to confined behavior, because both have much tighter MFP distributions that the other four models.

Table 3-3 highlights the differences among the models' predicted thermal conductivity reductions at three selected diameters. For example, at $D = 10$ μm the BvKS model predicts a reduction (17%) that is comparable to that of the MD (15%) and 1$^{st}$P (18.2±4.0%) calculations, because these three models all have the "longest tails" in their MFP distributions [Fig. 3.6(a)]. On the other hand, at this same diameter the gray (2%) and Holland (6%) models predict substantially smaller thermal conductivity reductions, because of their tighter MFP distributions and emphasis on shorter bulk MFPs.

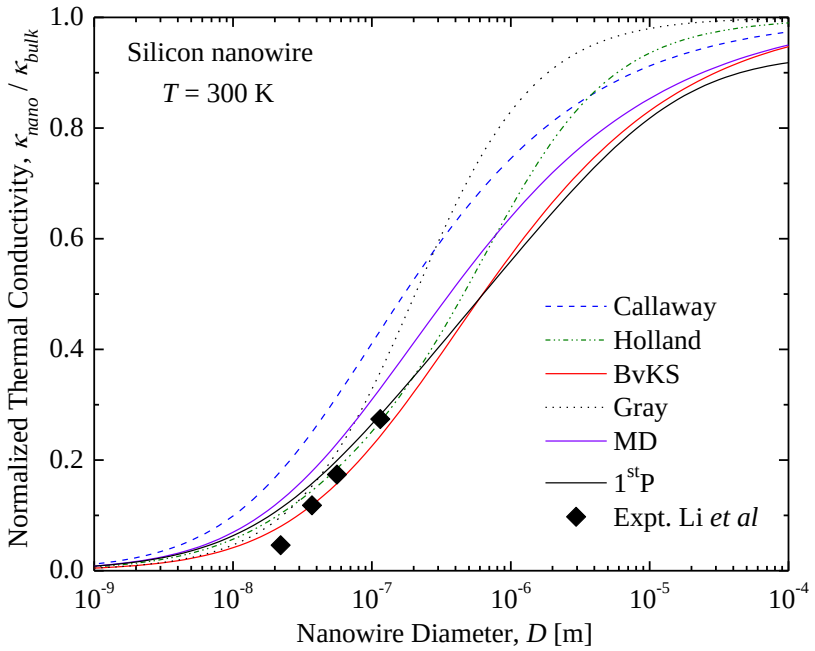


**Figure 3.7 Normalized thermal conductivity $\kappa_{nano}(D)/\kappa_{bulk}$ of silicon nanowires calculated using the integral transform of Eq. (12) and assuming diffuse boundary scattering. See also Table 3-3. The experimental data are from Li *et al.*[10] As explained in the main text, the curve for the 1stP spectrum is an average of two bounding cases, with spread less than ± 0.8% of $\kappa_{bulk}$ for $D \leq 1$ μm.**

**Table 3-3 Thermal conductivity reduction of silicon nanowires at 300 K compared with bulk, at three selected diameters. These points are a subset of Fig. 3.7. The range of values for the 1stP calculation reflect extreme bounds due to lack of information for $\alpha$ beyond $\Lambda_{bulk}$ = 6.58 μm (see text).**

| Model | Reduction compared to bulk, $(\kappa_{bulk} - \kappa_{nano})/\kappa_{bulk}$, [%] | | |
|---|---|---|---|
| | $D$ = 0.1 μm | $D$ = 1 μm | $D$ = 10 μm |
| Callaway (modified) | 59 | 25 | 9 |
| Holland | 75 | 36 | 6 |
| BvKS | 77 | 43 | 17 |
| MD | 69 | 36 | 15 |
| 1stP | 73.5±0.1 | 44.0±0.8 | 18.2±4.0 |
| Gray | 67 | 17 | 2 |

Comparing the model curves in Fig. 3.7 with the experiments of Li *et al.*[10] suggests that the modified Callaway model is not among the top choices. However, additional measurements of larger diameter samples (e.g. $D$ = 1 - 100 μm) would be needed to discriminate among the other five models. Also, none of these models can explain the measurement of the smallest diameter sample (22 nm), nor other recent reports of sub-Casimir thermal conductivity in Si nanowires[12, 13, 15]. Assuming that the MD and 1stP models are most likely to be correct for all diameters, inspection of Fig. 3.7 and Table 3-3 again suggests that among the four simpler models the BvKS model is likely to be most accurate.

### 3.3.4 Thickness Dependence of In-plane Thermal Conductivity for a Film

As a second application of the integral transform of Eq. (12), we consider the in-plane thermal conductivity of a film of thickness $d$ and diffuse surfaces. We again emphasize that this calculation uses only the geometry function and accumulation function for each model, and does not require explicit knowledge of any dispersion relation or scattering rule $\Lambda_{bulk}(\omega,s)$. The geometry function $B_{film}$ for this problem is readily obtained from the well-known solution of the Boltzmann transport equation by Fuchs and Sondheimer[97, 98],

$$B_{film}(Kn) = 1 - \tfrac{3}{8} Kn\left[1 - 4E_3\left(Kn^{-1}\right) + 4E_5\left(Kn^{-1}\right)\right], \tag{3.17}$$

where $E_n$ is the $n^{\text{th}}$ order exponential integral and here $Kn = \Lambda_{bulk}/d$.

The resulting thickness dependence of the film thermal conductivity is shown in Fig. 3.8. Because of the scatter in the experimental data[69, 107, 108], it is not possible to assess which of the models is best. Comparing the models to each other, the major trends are all qualitatively similar to those for the nanowire calculation in Fig. 3.7. For example, the Holland and gray models again show a sharper transition in $\kappa_{nano}(D)$, due to their narrower distributions and emphasis on shorter MFPs. Figure 8 also shows the importance of long MFP phonons in the BvKS, MD, and 1$^{st}$P models: For a 10-μm-thick film, the thermal conductivity reductions compared to bulk are 11% for BvKS, 10% for MD, and 13±5% for 1$^{st}$P (bounding scenarios), but only 6% for Callaway, 3% for Holland, and less than 1% for the gray model.

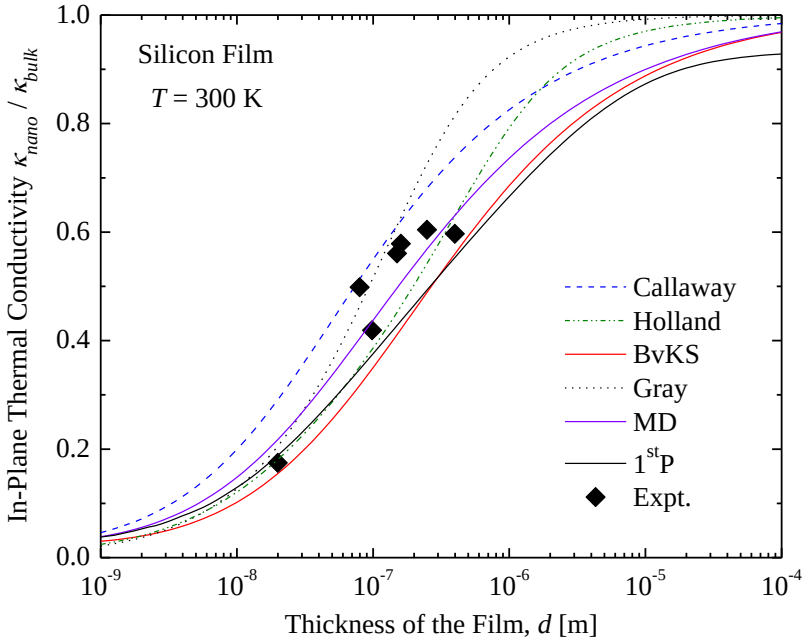


**Figure 3.8 Normalized in-plane thermal conductivity $\kappa_{nano}(d)/\kappa_{bulk}$ of silicon thin films, using the integral transform of Eq. (12) and assuming diffuse boundary scattering. The experimental data are from Refs. [69, 107, 108]. As with Fig. 3.7, the result for the 1$^{st}$P spectrum is an average of two bounding cases.**

### 3.3.5 Broadening of $\kappa_{nano}$ Compared to $\alpha$

Comparison of Fig. 3.6(a) with Figs. 7 and 8 suggests that the integral transform of Eq. (3.12) makes the $\kappa_{nano}(L_c)$ function even broader than the $\alpha(\Lambda_{bulk})$ function. This is fundamentally due to the smoothing effect of the kernel[44], whether $\frac{dB_t}{d\Lambda_{bulk}}$ (Eq. 3.12) or $B_t$ (Eq. 3.10). Focusing on the nanowire example, this broadening effect is more clearly seen in Fig. 3.9, which plots the accumulation functions and normalized conductivities together on the same axes. We show the BvKS model as a representative of the family of broad-spectrum models (which includes Callaway, MD, and 1$^{st}$P), and the gray model as a representative of the narrow-spectrum models (the other being Holland). In close analogy to the definition of the cutoff MFPs $\Lambda_\alpha$ in Eq. (3.5), here we define cutoff diameters $D_\beta$ such that

$$\beta\left(D_\beta\right)=\frac{\kappa_{nano}(D_\beta)}{\kappa_{bulk}}. \tag{3.18}$$

For example, at $D=D_{0.9}$, the nanowire thermal conductivity is reduced by 10% compared to bulk. For the BvKS model of Si nanowires at 300 K, these cutoff diameters are $D_{0.1}$=30 nm and $D_{0.9}$=29,900 nm, with a "bandwidth" of $D_{0.9}/D_{0.1}$ = 997, over five times larger than the MFP bandwidth of $\Lambda_{0.9}/\Lambda_{0.1}$=177 (Table 3-1). For the gray model, the cutoff diameters are $D_{0.1}$=24 nm and $D_{0.9}$=1,890 nm, with a bandwidth of $D_{0.9}/D_{0.1}$=79. Clearly this represents a great deal of broadening as compared to the gray model's delta-function MFP spectrum ($\Lambda_{0.9}/\Lambda_{0.1}$=1). A similar broadening effect was also reported in a 1$^{st}$P calculation for silicon and diamond nanowires[83].

.

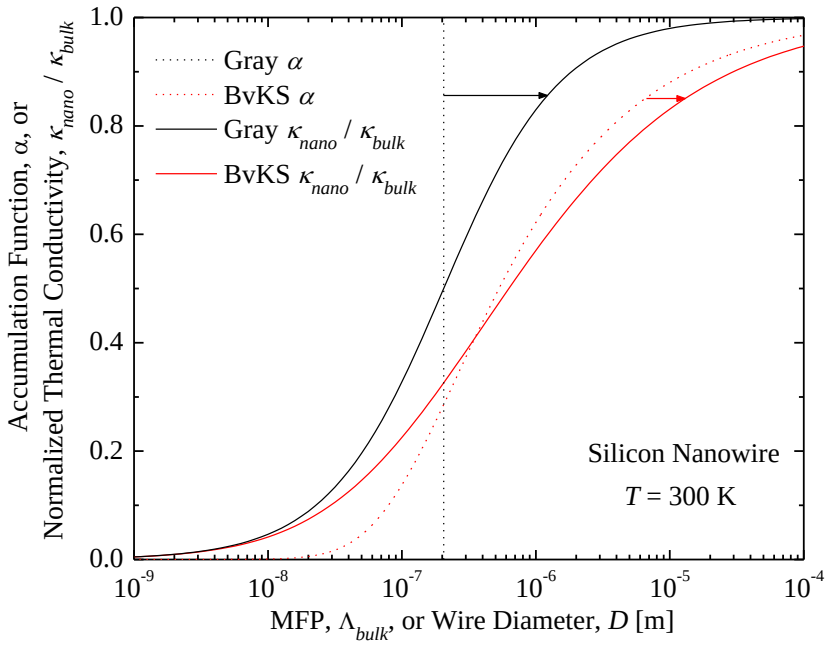


**Figure 3.9 Comparison of the bulk accumulation function (dashed lines) and normalized nanowire thermal conductivity (solid lines) for gray (black) and BvKS (red) models. As indicated by the arrows, for both models the $\kappa_{nano}(D)$ curves are substantially broadened as compared to the $\alpha(\Lambda_{bulk})$ curves.**

This broadening effect is relevant for current experimental efforts to measure the MFP distribution[20, 25], which use a plausible though currently unproven postulate that a sharp cutoff condition can be used to estimate a MFP spectrum from the raw measurements. Although those experiments[20, 25] are based on unsteady heating with varying frequency, here we consider the analogous postulate for a steady-state problem with varying $L_c$. Consider a hypothetical silicon-like material with a gray MFP spectrum. As shown in Fig. 3.9, a set of size-dependent measurements of this material would be broadened to a bandwidth of $D_{0.9}/D_{0.1}=79$. If this $\kappa_{nano}(D)$ dataset were then analyzed with a Koh & Cahill-type cutoff condition[20, 25], the estimated MFP spectrum would then also be broadened to $\Lambda_{0.9}/\Lambda_{0.1}=79$, much larger than the true breadth $\Lambda_{0.9}/\Lambda_{0.1}=1$. A more sophisticated approach to estimating $\alpha(\Lambda_{bulk})$ from $\kappa_{nano}(D)$ would require careful use of inverse methods[84], although this is known to be challenging for Fredholm equations of the first kind with smoothing kernels, such as Eqs. (10) and (12).[44]

## 3.4 Summary and Conclusions

Expressions for the bulk MFP spectrum (Eq. (4)) and accumulation function (Eq. (5)) have been rigorously re-derived[18]. The key physical insight is to write the kinetic theory integral in terms of MFP rather than frequency. The major restrictions are the assumptions that wave confinement effects are negligible, the bulk dispersion relation and bulk MFPs are approximately isotropic, and any thermal transients are much slower than the carrier relaxation times.

Extending this framework to nanostructures leads to the integral transform of Eq. (3.10). The inputs to the transform are the bulk MFP spectrum and a geometry function for boundary scattering, and the output is the size-dependent thermal conductivity of the nanostructure. Equation (3.12) is an equivalent transform in terms of the accumulation function, which may be preferred for practical reasons. The most important feature of these transforms is that they require no summation over polarizations and no explicit knowledge of the energy carriers' dispersion relation or bulk scattering rules. Rather, the derivation shows that this information is already incorporated in the bulk MFP spectrum in exactly the form needed to evaluate the additional effects of boundary scattering. This major simplification is not possible if the integrals are expressed in terms of other common quantities such as frequency, wavelength, or relaxation time.

Thus, the framework of MFP spectra (or accumulation functions) has two major benefits: visualization of the important MFPs for bulk thermal conductivity, and quantitative evaluation of a nanostructure's thermal conductivity given its bulk MFP spectrum. Therefore it is hoped that future models of the bulk thermal conductivity will include at least one plot of the accumulation function[18, 20, 25, 78-83].

To demonstrate these benefits, this paper closes with a case study of six models for phonons in bulk silicon: three analytical[31, 85, 86], one gray, and two purely

numerical[78, 82]. Among the four simple models, the BvKS model is in closest agreement with the more sophisticated numerical results of Henry and Chen[78], Li *et al.*[83], and Esfarjani *et al.*[82, 106]. This suggests that the BvKS model should be preferred over the gray, Holland, and modified Callaway models for studies involving phonon boundary scattering[18, 31, 71]. However, further experimental studies of the MFP spectra[20, 25], coupled with rigorous theoretical interpretation, are also needed.

## 3.5 Appendix A: Models of Si Thermal Conductivity

Table 3-4 summarizes the dispersion relations and scattering rules for the three analytical models used in the main text. These models ignore heat conduction by optical phonons and use simple functions to approximate the phonon dispersion and scattering rules for acoustic phonons. We use the Holland model exactly as described in the original work[86], including the values of all fitting parameters, so it is not discussed further here. Below we describe our implementation of the Callaway model[85] with a modified umklapp scattering law as well as a Born-von Karman-Slack (BvKS) model[31].

**Table 3-4 Summary of thermal conductivity models used in this paper. *A*, *b*, $C_U$, and $P_i$ are adjustable parameters.**

| Model | Dispersion | Phonon branch | Scattering Rates | | |
|---|---|---|---|---|---|
| | | | Boundary $\tau_B^{-1}$ | Impurity $\tau_I^{-1}$ | Phonon-Phonon $\tau_{PP}^{-1}$ |
| Callaway (modified) | Debye | Average | $v_g / b$ | $A\omega^4$ | $P\omega^2 T e^{-C_U/T}$ |
| Holland | Piecewise linear | *TO* | $v_g / b$ | $A\omega^4$ | $P_T \omega T^4$ |
| | | *TU* | $v_g / b$ | $A\omega^4$ | $P_{TU}\omega^2 / \sinh\left(\frac{\hbar\omega}{k_B T}\right)$ |
| | | *L* | $v_g / b$ | $A\omega^4$ | $P_L \omega^2 T^3$ |
| BvKS | BvK | Average | $v_g / b$ | $A\omega^4$ | $P\omega^2 T e^{-C_U/T}$ |

The Callaway model is based on a Debye dispersion relation for a single, triply-degenerate phonon branch. The Debye temperature $\theta_D$=530 K is calculated from

$$\theta_D = \left(6\pi^2 / V_P\right)^{1/3} \hbar v_s / k_B, \tag{3.19}$$

where $V_P$=3.98 × $10^{-29}$ $m^{-3}$ (Ref. [109]) is the volume of a primitive unit cell which contains 2 Si atoms and $v_s$=6084 m/s (Ref.[45]) is an average sound velocity. The original Callaway model[85] used an umklapp scattering rule with a lifetime proportional to $T^{-3}$, which is not appropriate for temperatures near or above the Debye temperature where the behavior is close to $T^{-1}$. Therefore, to adapt this model to high temperatures we replace Callaway's original umklapp scattering law with a common form[88, 104, 110]

$$\tau_{PP}^{-1} = P\omega^2 T \exp\left(-\frac{C_U}{T}\right) \tag{3.20}$$

where $P$ and $C_U$ are fitting parameters. For the natural silicon of interest in this work we neglect Callaway's $k_2$ correction term, which is only important for isotopically pure materials[86, 88, 93]. All other model parameters retain the same form as in the original paper[85]. We fit this modified Callaway model to the experimental data from Holland[86], yielding the fitting parameters shown in Table 3-5.

The Born–von Karman-Slack (BvKS) model is based on the Born–von Karman dispersion, $\omega = \omega_{\max} \sin\left(\pi q / 2 q_{\max}\right)$, where $q_{max}$=1.14×10$^{10}$ m$^{-1}$is the Debye cutoff wavevector based on the number density of primitive unit cells. The BvK dispersion includes the reduction of group velocity for wavevectors approaching the boundary of the first Brillouin zone[31, 45], although this rolloff is overestimated for LA modes in Si. As with our implementation of the Callaway model, in this BvKS model we approximate the three acoustic branches with a single effective branch based on an average sound velocity of 6084 m/s, and use Eq. (3.20) for phonon-phonon scattering. To the best of our knowledge this form of scattering time was first discussed by Slack[110], which is the reason we refer to this model as BvKS.

**Table 3-5 Scattering parameters used in the Callaway and BvKS models.**

| | $A$ ($10^{-45}$ s$^3$) | $P$ ($10^{-19}$ sK$^{-1}$) | $C_U$ (K) | $b$ (mm) |
|---|---|---|---|---|
| Callaway (modified) | 2.73 | 2.73 | 173 | 5.7 |
| BvKS | 2.54 | 1.53 | 144 | 5.7 |

## 3.6 Appendix B: Analytical Accumulation Function for Long MFP Phonons

We present a convenient analytical form for the $\alpha(\Lambda_{bulk})$ function for phonons in the long MFP limit. This is a straightforward generalization of unpublished results for the case of $\omega^{-2}$ umklapp scattering recently obtained independently by Cahill[111] and then Freedman & Malen[112]. The form below should prove useful for extrapolating numerical accumulation functions such as from first principle calculations,[82, 106] which are unable to directly calculate very long MFPs, as well as interpreting measured accumulation functions.

We consider a general scattering power law

$$\Lambda_{bulk} = A\omega^{-n}, \tag{3.21}$$

where $A$ may depend on $T$ but not $\omega$. This form applies for most common bulk scattering mechanisms, including impurities ($n$=4), umklapp ($n$=2), Akheiser damping[113] ($n$=0 - 2) and boundaries ($n$=0 or 1, Ref. [[71]]). In a bulk sample usually $n$>0, and thus large MFPs correspond to small $\omega$, justifying a Debye approximation for the long-MFP tail regardless of $T$. Furthermore, for sufficiently small $\omega$ it is always true that $\hbar\omega << k_B T$, so it is convenient to approximate the Bose-Einstein function by $f \approx \frac{k_B T}{\hbar\omega}$. Focusing on a

single scattering mechanism with $0 < n < 3$, applying this high-temperature Debye model to Eq. (2) yields

$$\kappa_{bulk} \propto \int_0^{\omega_D} \omega^{2-n}\, d\omega \propto \int_{\Lambda_D}^{\infty} \Lambda_{bulk}^{-\frac{3}{n}}\, d\Lambda_{bulk} \propto \Lambda^{1-\frac{3}{n}}\Big|_{\Lambda_D}^{\infty}, \qquad (3.22)$$

where $\Lambda_D = \Lambda_{bulk}(\omega_D)$ is the minimum MFP, *e.g.* at the Debye cutoff frequency. This form diverges for $n \geq 3$ in an infinite crystal, in which case we also allow for MFP truncation at some maximum length scale $L_{max}$, much larger than $\Lambda_D$.

Continuing to the accumulation function $\alpha(\Lambda_{bulk})$ from Eq.(3.5), we consider four cases depending on the value of $n$. For $0 < n < 3$, as in umklapp scattering,

$$\alpha(\Lambda_{bulk}) = 1 - \left(\frac{\Lambda_{bulk}}{\Lambda_D}\right)^{1-\frac{3}{n}} \qquad (3.23)$$

The analogous result for $n$=0 is identical to the gray assumption discussed in the main text with $\Lambda_{gr} = \Lambda_D$, so the accumulation is a Heaviside step function, $H(\Lambda_{bulk} - \Lambda_D)$. Results for $n$=3 and $n$>3 are given in Table 3-6, where the last expression also assumes $L_{\max} >> \Lambda_{bulk} >> \Lambda_D$. We note that results equivalent to Eq. (3.23) for $n$=2 were obtained previously by Cahill[111] and Freedman & Malen[112].

**Table 3-6 Analytical forms for the accumulation functions in the high-temperature Debye limit corresponding to Eq. (3.22), for different scattering exponents *n*.**

| | $n$=0 | $0 < n < 3$ | $n = 3$ | $n > 3$ |
|---|---|---|---|---|
| $\alpha(\Lambda_{bulk}) =$ | $H(\Lambda_{bulk} - \Lambda_D)$ | $1 - \left(\frac{\Lambda_{bulk}}{\Lambda_D}\right)^{1-\frac{3}{n}}$ | $\frac{\ln(\Lambda_{bulk}/\Lambda_D)}{\ln(L_{\max}/\Lambda_D)}$ | $\frac{\Lambda_{bulk}^{1-\frac{3}{n}} - \Lambda_D^{1-\frac{3}{n}}}{L_{\max}^{1-\frac{3}{n}}}$ |

To apply these analytical forms to extrapolate the numerical results[82, 106] of Fig. 3.6, we relax the derivation to require a pure power law only in the limit of small $\omega$, while allowing arbitrary $\Lambda_{bulk}(\omega)$ for moderate and large $\omega$. Thus, Eq. (3.22) applies for all $\Lambda_{bulk}$ beyond some threshold $\Lambda_T$ defining the long tail regime, at which point the accumulation has the value $\alpha_T = \alpha(\Lambda_T)$. For example, this point ($\Lambda_T$,$\alpha_T$) might be the longest MFP that was simulated numerically[82, 106] or measured experimentally[112]. For compactness we define a remainder function $r(\Lambda_{bulk}) = 1 - \alpha(\Lambda_{bulk})$ to describe the thermal conductivity contribution beyond $\Lambda_{bulk}$. Repeating the above analysis gives

$$r = r_T \cdot \left(\frac{\Lambda_{bulk}}{\Lambda_T}\right)^{1-\frac{3}{n}} \qquad (3.24)$$

for $\Lambda_{bulk} \geq \Lambda_T$ and where $r_T = 1 - \alpha_T$. Recognizing that the point $(\Lambda_T, r_T)$ is known, Eq. (3.24) shows that the long MFP tail will still have a clean analytical form even though the behavior for $\Lambda_{bulk} < \Lambda_T$ may be much more complicated. Thus, if the power-law

exponent in the long-MFP regime is believed known or bounded, Eq. (3.24) should be useful for extrapolating an incomplete accumulation function[82, 106]. Equation (3.24) holds for $0 < n < 3$, while the analogous derivations for other values of $n$ are similarly straightforward.

Equation (3.24) also suggests convenient transformed axes for graphically identifying the dominant scattering exponent $n$ from numerical and/or experimental data. In the long mean free path (i.e. low-frequency) limit, a plot of $\ln(r)$ versus $\ln(\Lambda_{bulk})$ should be a straight line with slope $1-\frac{3}{n}$, for MFP ranges where $n$ is approximately constant and $0<n<3$. Figure 3.10 gives an example of these transformed axes. For $\Lambda_T$ we choose the last available MFP from the 1$^{st}$P calculation[82, 106], 6.58 μm, and anchor all curves to this point as indicated by the solid black circle. This calculation confirms that the long MFP tails of the Callaway[85], Holland[86], and BvKS[31, 45] models all collapse onto the same $n$=2 behavior, with a shape matching that obtained previously[111, 112]. The MD results from Henry and Chen[78] have a slightly stronger exponent of $n \approx 2.1$ in this regime, while the 1$^{st}$P results from Esfarjani *et al*.[82, 106] are less clear but also appear to have $n$ of around 2. Thus, the good agreement between all six curves of Fig. 3.10 in the long MFP regime confirms that Eqs. (3.23) and (3.24) should be a reliable basis for analytical extrapolation.

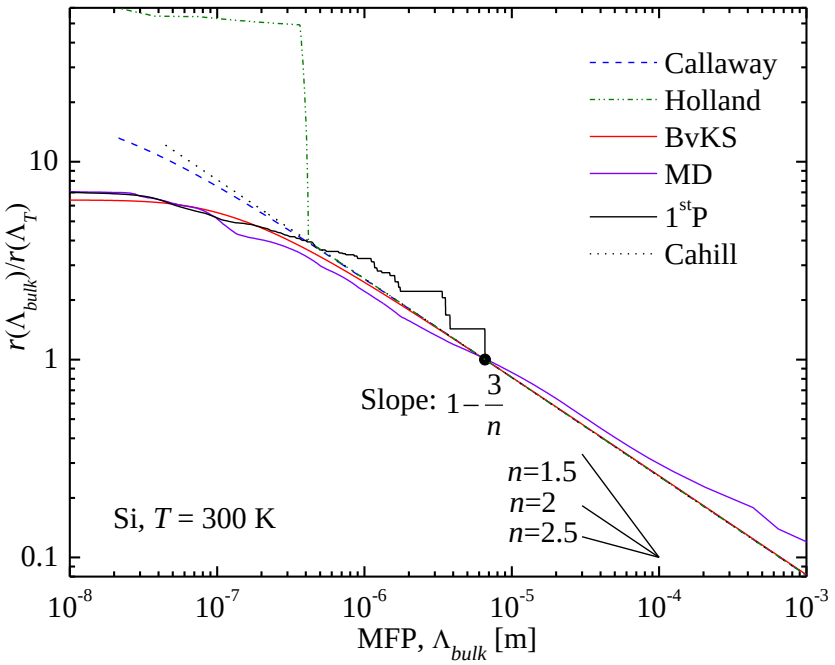


**Figure 3.10 Remainder functions $r(\Lambda_{bulk}) = 1-\alpha(\Lambda_{bulk})$ for different models in the long mean free path region for Si at 300 K. All six curves are referenced to the same arbitrary tail point $\Lambda_T$=6.58 μm.**

# Chapter 4 Heating Frequency Dependent Thermal Conductivity: an Analytical Solution From Diffusive to Ballistic Regime

## 4.1 Introduction

The diffusion process of Fourier's law of heat conduction breaks down whenever the characteristic length or time scale of a problem is smaller than the energy carrier's mean free path (MFP) or mean free time (MFT, *i.e.* relaxation time), respectively. Understanding the corresponding MFP or MFT distributions is crucial for controlling the thermal conductivity in nanostructured materials[18, 20, 22] or ultrafast process[25, 114, 115], and thus would help designing and optimizing a wide range of applications, such as heat dissipation and chip cooling[8, 34], thermoelectric energy conversion[12, 16], nanomedicine[116], *etc*. Essentially all studies of the thermal conductivity accumulation function have used MFP as the independent variable of the accumulation, including both modeling [18, 67, 78, 79, 81-83] and experiments[20, 22, 25, 26, 117].

One approach to measuring the accumulation function uses a heat source of small and variable size, to restrict the range of phonons which can fully participate in the heat conduction. In this way Minnich *et al.* reported a direct measurements of the phonon accumulation function, using optical heat sources with sizes first in the range of tens of microns[20, 118] then tens of nanometers[119]. Based on a related steady-state solution to the Boltzmann transport equation (BTE)[120], a cutoff approximation was made that phonons with MFPs longer than the spot size were fully ballistic and contributed negligibly to heat conduction. Thus, the measured apparent thermal conductivity was taken to represent the contribution of the phonons with MFP less than the spot size.

The other method used to obtain the accumulation function is to vary the heating frequency. Koh and Cahill[25] first measured heating frequency dependent thermal conductivity and reported the thermal conductivity per MFP, the derivative of the accumulation function. For several semiconductor alloys they found that the thermal conductivity measured by time domain thermoreflectance (TDTR) depended on heating frequency even at frequencies below 10 MHz. Similar measurements were extended to higher heating frequency (200 MHz) electro-optic modulators for natural silicon by Regner *et al.* using frequency domain thermoreflectance (FDTR)[26]. In both approaches the thermal conductivity accumulation function was calculated using Koh and Cahill's cutoff assumption that phonons with MFPs longer than the Fourier-law penetration depth would not conduct heat, evaluated using either the bulk[25] or frequency-dependent[26] thermal diffusivity.

The basis of using some form of truncated Fourier law has been widely used in the accumulation measurements and data interpretation[20, 25, 26, 117, 121, 122]. Since these experiments are specifically designed so that ballistic effects are significant over much of the measurement range, raising the question of whether the Fourier law is an

appropriate treatment for these measurements. A quantitative assessment of Koh and Cahill's cutoff assumption[25] by comparison with a more rigorous analysis is still needed. Thus, nondiffusive solution to the BTE has attracted great attention recently. There are numerical efforts on solving BTE to obtain the accumulation function.[84, 118, 123] Most recently, to deep understand the ballistic transport, there are also reports on analytical solutions. Collins *et al.*[124] and Hua *et al.*[125] analytically solve the nondiffusive BTE with periodic spatial distribution condition. Regner *et al.*[126] also obtained the analytical solution to BTE on both periodic heating planar and spherical heating sources. With the solution, they investigated the penetration depth and heating source size effects and also the suppression function.

However, there still have no systematic work on directly converting the measured experimental quantities, such as surface temperature phase lag with respect to heat flux in FDTR[28] or temperature decay in TDTR[25], to the ballistic phonon properties, such as accumulation function, yet. Thus, the present work uses the Boltzmann transport equation (BTE) to connect the macroscopic property of temperature phase lag to ballistic property of accumulation function. A second challenge in the rigorous analysis of existing TDTR[20, 25] or FDTR[26] accumulation data is that the measurements potentially involve subcontinuum phenomena in both time scale (modulation frequency) and length scale (laser spot size). Isolating the effects of each mechanism also needs to be explored. Our previous work[67] gave a rigorous BTE framework for steady state problems where only length scale matters. Here, we consider the complementary case where the subcontinuum phenomena arise purely from a periodic timescale effect, by using an infinite plane source to eliminate any spot size effects.

In this work, we build up a BTE-based framework to interpret the experimental quantities and bridge them to the ballistic properties, as shown in Fig.4.1. We first obtain an analytical solution to the gray BTE with a planar heat source. Then, we extend this gray model to the non-gray regime, which helps explain the heating frequency dependent thermal conductivity observed for semiconductor alloys[25]. Then, we provide a BTE based data analysis scheme instead of Fourier law based scheme for thermal conductivity measurement, as shown in Fig. 4.1 with more discussion in Sec. IIC. Finally, a virtual experiment is considered, which shows that for periodic planar heating the phonon accumulation is better recovered using a cutoff condition based on heater timescale rather than the apparent thermal penetration depth. An approximation method of obtaining thermal conductivity accumulation function with respect to MFT is also introduced.

## 4.2 Description of Model

Here we present the problem statement, outline the solution, and give the key theoretical results. Derivation details are deferred to the Chapter 4.5 to 4.8. Chapter 4.5 describes the two-flux BTE solution; Chapter 4.6 gives the analytical solutions for temperature, heat flux, penetration depth, temperature to heat flux phase lag; Chapter 4.7 describes the relationship between effective carrier velocities in one-dimensional (1D) and three-dimensional (3D) treatments; and Chapter 4.8 discussed the analytical solution

using the general form of 3D velocity treatment. The solution to the BTE and the difference between different approximations are also discussed.

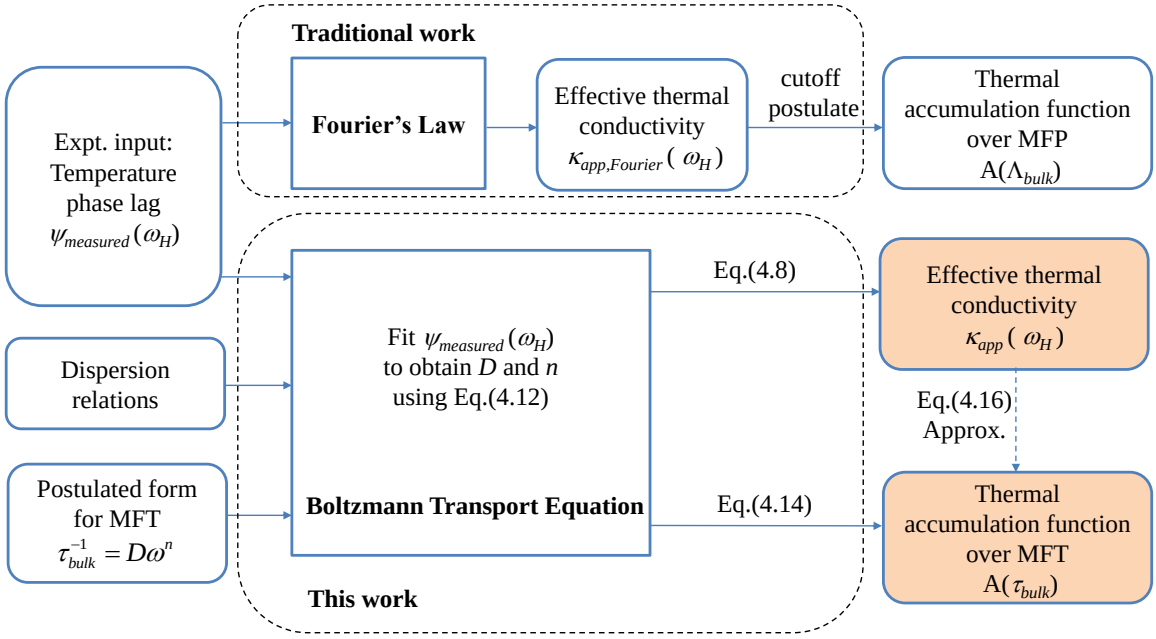


**Figure 4.1 Conceptual comparison between Fourier[28] and BTE (this work) approaches for obtaining the phonon accumulation function from measured temperature phase lag data.**

### 4.2.1 Periodic Heating Problem and BTE

This work focuses on heat conduction in a semi-infinite solid with periodic plane-source heating on the surface, especially when the heating frequency is high enough that ballistic effects cannot be neglected. In current TDTR or FDTR experiments the fastest heating frequencies (~10 to 200 MHz,[25, 26, 117]) are still several orders of magnitude smaller than typical semiconductor phonon vibrational frequencies . Thus, quantum wave effects should be negligible and phonon wave packets can be treated as particles, so that the BTE is applicable[60].

We start with the three dimensional BTE which is usually complicated and time consuming to solve for an arbitrary geometry. However, due to the translational symmetry of the present planar heating problem as shown in Fig. 4.2, the problem would be greatly simplified into a problem in *x*-direction.

As refer to the one dimensional transport in *x*-direction, there are two types of pictures for the group velocity, as shown in Fig.4.3. The simplest picture is assuming all the phonons transport in the same direction and with the same velocity $v_{1D}$, as showing in Fig. 4.2(a). Literature numerical simulations use this picture, especially in lattice Boltzmann transport equation (LBTE)[26], due to its greatly reduction of computational time (We also use this treatment in our LBTE in Sec. IIE). However, the other more realistic picture is assuming phonon isotropically travel along all directions, as shown in Fig. 4.2 (b). In this picture, the net heat flux of all phonons would still in one direction

due to symmetrical cancelation. In this work, we will first develop the BTE solution framework using the first picture in Fig. 4.2(a) and also verify it by the numerical LBTE method. Then, we will extend it to a more general picture in Fig. 4.2(b) and discuss their difference in the Chapter 4.8.

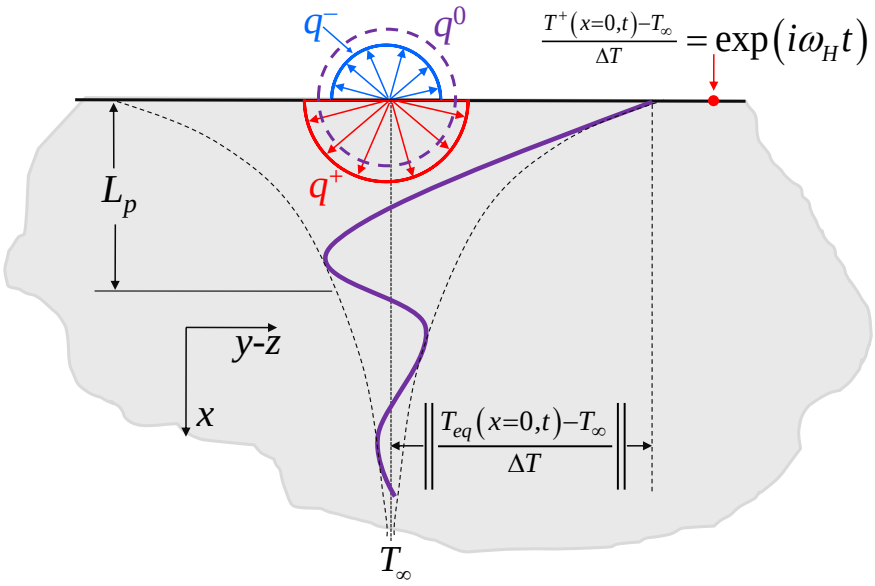


**Figure 4.2 Schematic of two flux BTE model of a semi-infinite solid with a planar periodic heat source of angular frequency $\omega_H$. Equilibrium temperature profile (solid purple) and temperature amplitude (dashed black) are also shown.**

The Boltzmann transport equation is firstly solved using a gray assumption (all phonons have the same MFT). Then, to allow for materials where the phonons have a broad distribution of MFTs,[18, 26, 67] the solution is extended to the non-gray regime in Sec. IIB using a similar method as Ref. [23]. To simplify the solution, we restrict the polarization to single-branch.[45, 67] Then, the three acoustic branches are lumped into a single one, good agreement with experiment for both bulk[85] and nanowire[45] in literature indicates this lumped approximation is a good evaluation. The optical modes are neglected due to their small group velocity. The isotropic Born-von Karman (BvK) dispersion is also used[23].

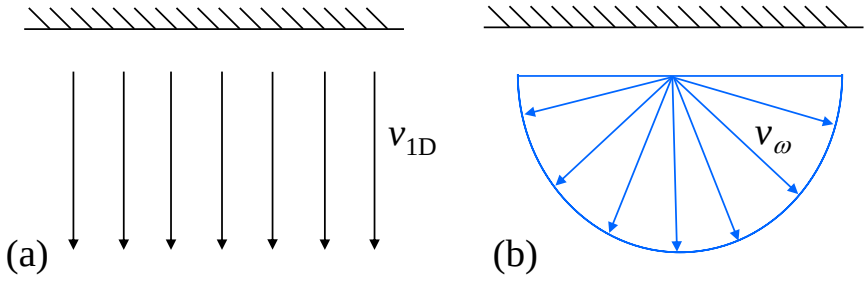


**Figure 4.3 Schematics of one dimensional and three dimensional views of group velocities. (a) all phonons travel at the same direction to form a 1D transport. (b) All phonons travel isotropically in all directions with group velocity $v_\omega$, but the net momentum is one dimensional transport.**

Based on the single relaxation time (MFT) approximation, the one dimensional BTE for phonons in the *x*-direction has the form[4, 102]

$$\frac{\partial f_\omega}{\partial t} + v_\omega \mu \frac{\partial f_\omega}{\partial x} = \frac{f_\omega^0 - f_\omega}{\tau_\omega}, \tag{4.1}$$

where $f_\omega$ is the phonon distribution function at phonon frequency $\omega$, $f_\omega^0$ is the equilibrium phonon distribution function, $v_\omega$ is the group velocity, $\mu = \cos\theta$ is the angle dependence (with respect to *x*-axis) of group velocity, and $\tau_\omega$ is the phonon MFT. In the first velocity picture in Fig. 4.2(a), $\mu$ is a constant that $\mu = 1$ because all phonons travel in the same direction. The more general picture in Fig. 4.2(b) is discussed in Chapter 4.8.

In the experiments, such as FDTR[26, 28], the semi-infinite material usually has a periodic heat flux boundary condition on the surface ($x = 0$), which also lead the temperature has the same period. In this analysis, it is more convenient to obtain heat flux from temperature rather than reversely. Thus, we use the temperature boundary condition in the forward direction to launch phonons at

$$T^+(x=0,t) = T_\infty + \Delta T \exp(i\omega_H t), \tag{4.2}$$

where the superscript "+" means forward direction (later the superscript "−" means backward direction), $\omega_H$ is the heating frequency, $T_\infty$ is the ambient temperature, and $\Delta T$ is the amplitude of temperature variation which is the heating source in the forward direction and is much smaller than $T_\infty$. Building on the boundary condition in Eq.(4.2), the BTE of Eq.(4.1) can be solved for the gray model, using two flux models, as detailed in Chapter 4.5 and 4.6. The key results of this gray solutions are the equilibrium temperature $T_{eq}(x)$ and surface heat flux $q''_{net}(x=0)$, given in Eqs. (4.43) and (4.46), respectively.

### 4.2.2 Apparent Thermal Conductivity: Gray and Non-gray Model

Having obtained analytical expressions for the equilibrium temperature and heat flux on the surface of gray model in Chapter 4.6, we define an apparent thermal conductivity as the amplitude ratio of heat flux to equilibrium temperature gradient,

$$k_{app,gray}(\omega_H) = \left\| \frac{q''_{net}(\omega_H, x, t)}{\frac{\partial T_{eq}(x,t)}{\partial x}} \right\|, \tag{4.3}$$

where the arguments $x$ and $t$ in $q''_{net}(\omega_H, x, t)$ and $T_{eq}(x,t)$ drops out with each other. Substituting Eqs.(4.42) and (4.45) into Eq.(4.3), the apparent thermal conductivity of gray model is obtained. We expressed it as

$$k_{app,gray}(\omega_H) = B_t(\omega_H \tau_{gray}) k_{Fourier}, \tag{4.4}$$

where $\tau_{gray}$ is gray MFT, $k_{Fourier}$ is the Fourier limit of the bulk thermal conductivity, and $B_t(\omega_H, \tau_{gray})$ is the periodic heating effect term defined as

$$B_t(\omega_H \tau_{gray}) = \sqrt{\frac{1+d^2-2d\cos\phi}{1+d^2+2d\cos\phi}} \frac{1}{\sqrt{a^2+b^2}}, \tag{4.5}$$

where $a$, $b$, $\phi$, and $d$ are all only functions of $\omega_H \tau_{gray}$ and are defined and explained in Chapter 4.5. The $B_t$ function, here in the time scale, serve the similar function as the Kernel function in the length scale[67], as more detailed comparison showing in Table 4-1. The Kernel function is also called suppression function in other works[84, 123, 124, 126]. Importantly, this $B_t$ function depends only on $\omega_H \tau_{gray}$ and not on any other material properties, such as group velocity, as shown in Sec. IID. For $\omega_H \tau_{gray} << 1$, $B_t(\omega_H \tau_{gray}) \to 1$ which recovers the Fourier limit.

All of the discussion above is based on the gray MFT model. However, in real materials the phonon MFPs (or MFTs) have a broad distribution, typically spanning two to three orders of magnitude at room temperature[18, 20, 26, 67, 78], and necessitating a non-gray model. From kinetic theory, after making a simple change of variables we express the bulk thermal conductivity $k_{bulk}$ in terms of MFT as

$$k_{bulk} = \int_0^\infty \mathrm{K}_\tau\left(\tau_\omega\right) d\tau_\omega \,. \tag{4.6}$$

Here $\mathrm{K}_\tau(\tau_{bulk})$ is the thermal conductivity per MFT,

$$\mathrm{K}_\tau\left(\tau_\omega\right) = \sum_s \tfrac{1}{3} C_\omega v_{1D}^2 \tau_\omega \left(\frac{d\tau_\omega}{d\omega}\right)^{-1}, \tag{4.7}$$

where $s$ represent the polarizations and $C_\omega$ is the specific heat per phonon frequency, which is in close analogy to the thermal conductivity per MFP $\mathrm{K}_\Lambda\left(\Lambda_{bulk}\right)$ in the length scale[18, 67].

Next, to construct an apparent thermal conductivity for this non-gray model, the phonon population is broken into numerous bands $\omega\tau_\omega$, each of which is treated as gray using Eq.(4.4). Summing up all the band-wise contributions[23] yields the apparent thermal conductivity

$$k_{app}\left(\omega_H\right) = \int_0^\infty \tfrac{1}{3} C_\omega v_{1D}^2 \tau_\omega \left(\frac{d\tau_\omega}{d\omega}\right)^{-1} \frac{\tau_{eff}}{\tau_\omega} d\tau_\omega \tag{4.8}$$

where $\tau_{eff}$ is the effective MFT which depends on the heating frequency $\omega_H$ and also phonon vibrational frequency $\omega$. Comparing Eqs. (4.8) and (4.4) reveals the convenient identity $B_t\left(\omega_H \tau_\omega\right) = \frac{\tau_{eff}}{\tau_\omega}$, and finally the apparent thermal conductivity of the non-gray model simplifies to

$$k_{app}\left(\omega_H\right) = \int_0^\infty \mathrm{K}_\tau\left(\tau_\omega\right) B_t\left(\omega_H \tau_\omega\right) d\tau_\omega \,. \tag{4.9}$$

Equation (4.9) is one of the major results of this work. It is a Fredholm integral equation of the first kind, and is closely related an analogous result for the steady-state size effect in a nanostructure [e.g., Eq. (10) of Ref.[67]]. The example for the $B_t\left(\omega_H \tau_\omega\right)$ is shown in Fig. 4.4.

Here the short timescale effect of periodic heating reduces $\tau_{eff}$ and thus $k_{app}$, just as the small lengthscale effect of nanostructure boundary scattering[67] reduces $\Lambda_{eff}$ and $k_{app}$. Thus, the physical meaning of $B_t$ is to describe the strength of the periodic heating effect

in reducing $k_{app}$. as showing in Fig. 4.4(a). At low heating frequencies, $B_t$ = 1, there are no ballistic effects, the Fourier limit can be recovered. While at higher frequencies $B_t$ decreases indicating a stronger effect analogy between the present periodic heating problem in time scale and our previous work of MFP size problem in length scale, as it is given in Table 4-1. The function of heating frequency $f_H$ acts the same as characteristic size, which are used to determine the kernel function of the integral transform. The input function is the bulk property, the thermal conductivity per MFT or MFP. When the kernel is determined, apparent thermal conductivity of any structure or at any frequency heating can be obtained. More discussion of the $B_t$ function is in Sec. 4.2.4.

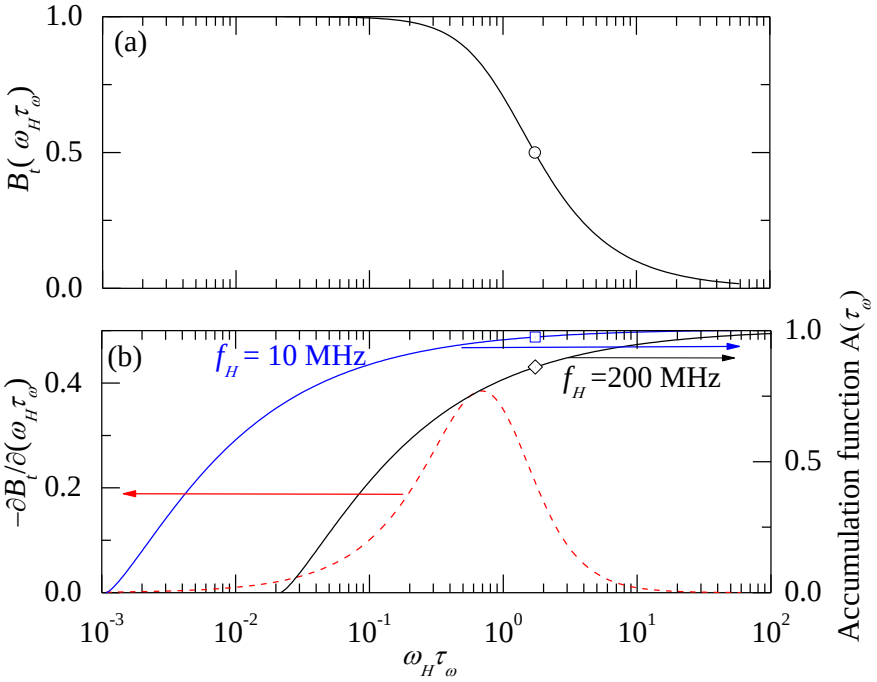


**Figure 4.4 (a) The $B_t$ function with respect to $\omega_H\tau_\omega$. (b) Accumulation function A($\omega_H\tau_\omega$) at different heating frequencies $\omega_H$ (note: A($\omega_H\tau_\omega$) itself is independent of $\omega_H$. Here $\omega_H$ is used to dimensionalize the *x*-axis, thus it scales *x*.) and integral transform kernel $\partial B_t/\partial(\omega_H\tau_\omega)$. The A($\tau_\omega$) is calculated for natural Si at 300 K (see text). The $B_t$ function and $\partial B_t/\partial(\omega_H\tau_\omega)$ function depend only on the product $\omega_H\tau_\omega$ and are general to all materials. The circle, square, and diamond mean the corresponding values at the $\omega_H\tau_\omega$ when $B_t$ =0.5, which has been used for MFT accumulation recovery in chapter 4.2.4.**

### 4.2.3 Experimental Determination of $k_{app}(\omega_H)$ From Phase Lag

Experimentally, the frequency-dependent thermal conductivity $k_{app}(\omega_H)$ is usually eva4luated by analyzing the raw phase[28] and/or amplitude[21] of the surface temperature response caused by periodic surface heating. In this work we consider the former. A detailed example is presented below in Sec. I using a virtual experiment which is calculated as follows.

**Table 4-1 Comparison of integral transform results for the small time scale effect (present work) and the small length scale effect[67]. Consistent with Ref.[67], $\Lambda_{bulk}$ is the bulk MFP, $L_c$ is the characteristic size, and $\Lambda_{eff}$ is the effective MFP.**

| | Time scale effect (infinite sample size) | Length scale effect (steady state) |
|---|---|---|
| Characteristic property of ballistic forcing | High heating frequency: $f_H$ | Small characteristic size: $L_c$ |
| Input function (material property) | $\mathrm{K}_\tau(\tau_\omega)$ Thermal conductivity per MFT [W/m-s-K] | $\mathrm{K}_\Lambda(\Lambda_{bulk})$ Thermal conductivity per MFP [W/m$^2$-K] |
| Kernel function (captures ballistic phenomenon) | $B_t(\omega_H\tau_\omega)=\frac{\tau_{eff}}{\tau_\omega}$ Characteristic time effect | $B_t\left(\frac{\Lambda_{bulk}}{L_c}\right)=\frac{\Lambda_{eff}}{\Lambda_{bulk}}$ Characteristic size effect |
| Apparent thermal conductivity (integral transform) | $k_{app}(\omega_H)=\int_0^\infty \mathrm{K}_\tau(\tau_\omega)B_t(\omega_H\tau_\omega)d\tau_\omega$ | $k_{app}(L_c)=\int_0^\infty \mathrm{K}_\Lambda(\Lambda_{bulk})B_t\left(\frac{\Lambda_{bulk}}{L_c}\right)d\Lambda_{bulk}$ |

Extending the gray model in Eq.(4.45) to include non-gray phenomena, the total heat flux at the surface is

$$q''_{net}(x=0,t)=\int_0^\infty \tfrac{1}{2}v_{1D}C_\omega\Delta T\left[1-d\exp(i\phi)\right]\exp(i\omega_H t)\,d\omega \tag{4.10}$$

Similarly, for the equilibrium temperature at the surface, the non-gray extension of Eq.(ach) is

$$T_{eq}(x=0,t)-T_\infty=\frac{\int_0^\infty \tfrac{1}{2}v_{1D}C_\omega\Delta T\left[1+d\exp(i\phi)\right]\exp(i\omega_H t)d\omega}{\int_0^\infty v_{1D}C_\omega d\omega}. \tag{4.11}$$

Thus, the phase lag $\psi_{surface}(\omega_H)$ of the equilibrium temperature with respect to the heat flux at the surface is obtained from

$$\frac{q''_{net}(x=0,t)}{T_{eq}(x=0,t)-T_\infty}=R_{amp,surface}\exp\left[i\psi_{surface}(\omega_H)\right], \tag{4.12}$$

where both $R_{amp,surface}$ and $\psi_{surface}$ are real numbers which depend on $\omega_H$. It is important to note that the physical origin of the phase lag in Eq. (4.12) is purely due to ballistic effects, whereas the phase lags reported in FDTR literature[26, 28] involve both ballistic and Fourier-law effects. Those FDTR measurements use a small (~microns) spot size, and when the heating frequency $f_H$ increases the thermal penetration depth decreases, causing the classical heat diffusion problem to transition from a point source regime (small $f_H$) to a plane source regime (large $f_H$). The corresponding phase lag thus increases from 0° to 45° due to purely Fourier-law effects. In addition, for larger $f_H$ ballistic effects also become important, causing the phase to roll off more quickly, the effects of which have been analyzed using modified Fourier-law models[26, 28]. In contrast, the present work considers a planar heat source, removing a length scale from the problem and ensuring that the classical solution exhibits a constant phase of 45° for all frequencies. Thus, any

changes in phase from Eq. (4.12) correspond unambiguously to ballistic effects, which we analyze using a BTE rather than Fourier treatment.

Taking the phonon dispersion relation [and thus $C_\omega(\omega)$ and $v\omega(\omega)$] as known, Eqs. (4.10) to (4.12) show how to calculate $\psi_{surface}(\omega_H)$ from $\omega_H \tau_{bulk}$. In experiment, it is natural to attempt the inverse problem: Given a set of measured phase lag data $\psi_{surface}$ $(\omega_H)$, what is the best estimate of $\tau_{bulk}$? Theoretically, it is possible to numerically solve the single integral inverse problem[44, 84], such as the Fredholm integral equation[44]. However, due to measured heat flux and temperature are both integrated over all phonons in Eq.(4.12), the inverse problem would be the ratio of two integrals, which is nonlinear and complicated to solve. Thus, instead of solving the general inverse problem, as shown in Fig. 4.1, we use the forward solution to obtain the best fit for a simple $\tau_{bulk}$ function with a small number of adjustable parameters. For example, assuming the phonon major scattering has a power law form $\tau_{bulk}^{-1} = D\omega^n$, fitting experimental $\psi_{surface}(\omega_H)$ yields $D$ and $n$. If more mechanisms involve, Matthiessen's rule can be used to combine different scattering mechanisms. Finally, intermediate quantities such as $K_\tau(\tau_{bulk})$ and $k_{app}(\omega_H)$ can then be calculated from Eqs. (4.7) and (4.9), as shown in more detail in Sec. IIIC. The key difference compared to traditional work[20, 25] is that here the subcontinuum effects seen in the measurements are analyzed self-consistently using a subcontinuum BTE solution rather than continuum Fourier's law.

### 4.2.4 Thermal Conductivity Accumulation Function, A($\tau_{bulk}$)

With the detailed results from above, the phonons' broad distribution, previously described by thermal conductivity accumulation function with respect to MFP, can be explored. In prior studies, this accumulation function was indirectly obtained by assuming phonons with MFPs longer than the characteristic size (heating laser spot size[20 ] or Fourier-law penetration depth[25, 26]) would not conduct heat. In this work, however, for the periodic heating problem we find that analysis is more natural and rigorous for accumulation with respect to MFT rather than MFP. Fundamentally this is because the key quantities in the BTE solution depend most directly on $\omega_H \tau_{bulk}$. In particular, for the planar source problem non-Fourier behavior is clearly due to the $B_t(\omega_H \tau)$ term [Eq. (4.5)]. This is physically expected because the forcing that results in sub-continuum behavior is fundamentally a timescale, the heater frequency $\omega_H$, and thus should be compared to another timescale representing the phonon properties, for which the most natural choice is $\tau_{bulk}$.

It is also possible to re-cast $B_t$ in terms of length scales. Previous work[25] implicitly did this by converting $\omega_H$ to a Fourier-law penetration depth using $L_p = \sqrt{2k/C\omega_H}$, and converting $\Lambda_{bulk} = v_{1D}\tau_{bulk}$, so that $\omega_H \tau_{bulk} \to \frac{2k\Lambda_{bulk}}{Cv_{1D}L_p^2}$. This last form may be considered less physically satisfying for several reasons: it involves a greater number of material parameters including some from the dispersion relation; it invokes Fourier-law concepts for a non-Fourier regime; and there is ambiguity about whether the $k$ and $C$ used should represent the full phonon population or only a subset thereof (*e.g.*, acoustic or acoustic + optical modes, perhaps with some weighting to be determined). In

contrast, expressing $B_t$ directly as a function of $\omega_H \tau_{bulk}$ makes it a universal function which is general to any material. Thus, for the heating frequency dependent measurement, we conclude that the accumulation function with respect to MFT is more suitable to capture the physics of the distribution of phonon scattering. A more detailed comparison between MFT- and MFP-based analyses is given in Sec. IIIC.

Similar to thermal conductivity accumulation with respect to MFP[18, 67, 78], $\alpha(\Lambda_\alpha)$, we introduce the thermal conductivity accumulation function with respect to MFT as

$$\mathrm{A}\left(\tau_{\mathrm{A}}\right)=\frac{1}{k_{bulk}}\int_0^{\tau_{\mathrm{A}}}\mathrm{K}_\tau\left(\tau_\omega\right)d\tau_\omega\,, \tag{4.13}$$

where $\mathrm{A}(\tau_{\mathrm{A}})$ represents the fraction of the total thermal conductivity contributed by phonons with MFTs less than $\tau_{\mathrm{A}}$ and $k_{bulk}$ is essentially the same as $k_{Fourier}$ in bulk materials. For investigating heating frequency $\omega_H$ effect, we normalize the apparent thermal conductivity to Fourier limit $k_{Fourier}$. After some manipulations and integrating by parts, the apparent thermal conductivity in Eq.(4.9) can be expressed as

$$\frac{k_{app}(\omega_H)}{k_{Fourier}}=-\int_0^{\infty}\mathrm{A}\left(\tau_\omega\right)\frac{dB_t}{d(\omega_H\tau_\omega)}d\left(\omega_H\tau_\omega\right). \tag{4.14}$$

Like Eq. (4.9), this Fredholm integral equation shows how to convert between the bulk MFT spectrum represented by $\mathrm{A}(\tau_\omega)$ and the apparent frequency-dependent thermal conductivity $k_{app}(\omega_H)$, via the kernel $B_t$, and has an analogous counterpart for length-scale effects in steady state problems[67, 84].

With Eq.(4.9) or (4.14), we can explain why the apparent thermal conductivity is dependent on heating frequency $\omega_H$ intuitively, as shown in Fig. 4.4(b). It is interesting to find that $-\frac{dB_t}{d(\omega_H\tau_\omega)}$, which is also independent of material, acting as a sampling window (red dashed curve). For the fixed MFT $\tau_\omega$, $\mathrm{A}(\tau_\omega)$ function would shift in the higher heating frequency $\omega_H$ direction when $x$-axis is transformed to $\omega_H\tau_\omega$ (such as from blue to black curve). Since the thermal conductivity $k_{app}(\omega_H)$ in Eq.(4.14) is the area under product of the two curves $A\left(\tau_\omega\right)$ and $-\frac{dB_t}{d(\omega_H\tau_\omega)}$, when heating frequency $\omega_H$ increases, there has less overlap and $k(\omega_H)$ decreases.

If we have the experimental $k_{app}(\omega_H)$, whether we can reversibly recover the accumulation function $\mathrm{A}(\tau_\omega)$ in Eq.(4.14) have also attract great attention recently[25, 26, 84, 126]. Different numerical methods[44, 84] can be used to solve the inverse problem. To obtain a simpler analytical expression which still captures the main physics, we develop an approximation method here. Referring to Fig. 4.4(a) we approximate $B_t$ as a Heaviside step function,

$$B_t\left(\omega_H\tau_\omega\right)\approx H\left(1.73-\omega_H\tau_\omega\right)\approx H\left(0.28-f_H\tau_\omega\right). \tag{4.15}$$

We elect to place the step edge at $\omega_H\tau_\omega$=1.73 because that is where $B_t$ =0.5, as indicated by the circle in Fig. 4.4(a). Equation (4.15) makes the sampling window $-\frac{dB_t}{d(\omega_H\tau_\omega)}$ a Dirac delta function, and thus from Eq. (4.14)

$$\frac{k_{app}(t_c)}{k_\omega} \approx \mathrm{A}\left(\tau_\omega = t_c\right). \tag{4.16}$$

where $t_c$ is the characteristic time which is approximated as $t_c \approx \frac{1.73}{\omega_H} \approx \frac{0.28}{f_H}$. This means with $k_{app}(\omega_H)$, we can directly recover $\mathrm{A}\left(\tau_\omega = t_c\right)$, the accumulation function with respect to MFT, without inverse integral transforms, numerical manipulation, or knowledge of the dispersion relation. This approximation gives a good explanation for pure materials and alloys as detailed in Sec. IIIB.

A physical interpretation of Eq. (4.15) is that when phonons with $\tau > t_c$ contribute nothing to heat conduction, while phonons with $\tau < t_c$ contribute fully. The approximation of Eq. (4.15) is somewhat similar in spirit to Koh and Cahill's assumption that phonons with MFPs longer than the Fourier-law penetration depth do not contribute to the thermal conductivity[25]. However as noted above, for periodic heating it is more physical to define any cutoff condition in terms of the timescales rather than lengthscales.

### 4.2.5 Numerical LBTE for Verification of Gray Model

To verify the analytical BTE solutions of our gray model across more than three decades of heating frequency we use a numerical method, the lattice Boltzmann transport equation method[127 ]. The essence of this method is to constrain the phonons by lattice site. The time step $\Delta t$ and space step $\Delta x$ are related by $\Delta x = v_{1D}\Delta t$. A detailed explanation can be found in Ref. [127 ]. We use $0.025\Lambda_{gray}$ as the space step $\Delta x$ and $20\Lambda_{gray}$ to approximate a semi-infinite domain. This is sufficient because at even the lowest $f_H$ of interest (*e.g.* $2\pi f_H \tau_{gray} = 10^{-2}$ which approaching diffusive limit), $20\Lambda_{gray}$ is still at least two times larger than the penetration depth. The chosen simulation time is $\frac{5}{f_H}$ which has been verified as long enough to eliminate the initial condition's effect and reach steady state conditions.

## 4.3 Case Study: Si and SiGe

Silicon has been chosen as the main example in this work, because its bulk thermal properties are very well known which facilitates the modeling. For the gray LBTE, to make a direct comparison with Regner *et al*.[26], we use the same parameters: a gray MFP of 41 nm, specific heat of $1.66\times10^6$ J/m$^3$-K, and sound velocity of 6733 m/s. For the non-gray model, the same dispersion, Born-von Karman dispersion, and the same scattering parameters are used as our previous work[67].

### 4.3.1 Gray Model

*4.3.1.1 Equilibrium Temperature and Penetration Depth*

The gray model equilibrium temperature profile is investigated in the Chapter 4.6.1. The equilibrium temperature amplitude is expressed as

$\left\| \frac{T_{eq}(x)-T_\infty}{\Delta T} \right\| = \frac{1}{2}\sqrt{1+d^2+2d\cos\phi}\exp\left(-x\frac{b}{v_{1D}\tau_{gray}}\right)$ which is derived from Eq.(4.42) and $v_{1D}$ is the effective group velocity as discussed in Chapter 4.7. The spatial profile is compared to the Fourier limit as shown in Fig. 4.5.

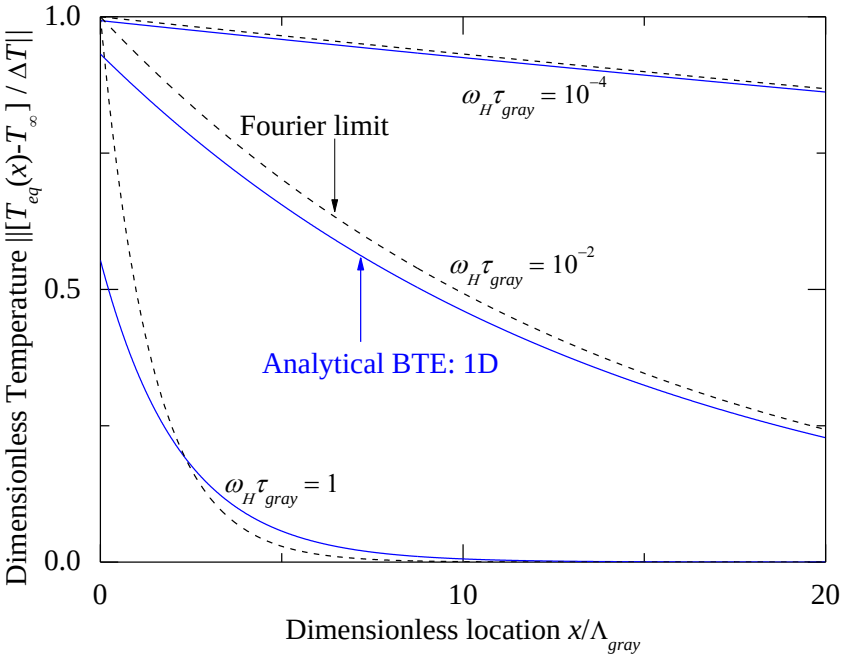


**Figure 4.5 Spatial distribution of the amplitude of normalized equilibrium temperature for three different heating frequencies $\omega_H\tau_{gray}$. The analytical BTE solution of Eq.(4.42) (blue solid line) is compared with the classical Fourier limit (black dashed line)[128 ]. The spatial location is normalized to the gray MFP $\Lambda_{gray}$, and the temperature amplitude to $\Delta T$, which is the temperature variation amplitude in the positive direction, the latter resulting in slip at higher frequencies.**

When the phonons have sufficient time to reach local equilibrium ($\omega_H\tau_{gray}<<1$), the analytical solution approaches the Fourier limit (<1% difference for $\omega_H\tau_{gray}<10^{-4}$). As $\omega_H\tau_{gray}$ becomes larger, the analytical solution deviates from this limit. For instance, at the surface $x$ = 0, the difference between BTE and Fourier solutions for the amplitude of equilibrium temperature oscillation $||T_{eq}(x=0)-T_\infty||$ increases from 0.7% at $\omega_H\tau_{gray}=10^{-4}$ to 6.8% at $\omega_H\tau_{gray}=10^{-2}$. As seen in Fig. 4.6(a), for even larger $\omega_H\tau_{gray}$ the surface temperature amplitude of the BTE solution monotonically approaches half of the Fourier limit. This surface temperature slip arises indicate the ballistic effect, because the amplitude of the backward flow $T^-(x)-T_\infty$ at the surface is much smaller than that of the forward flow $T^+(x)-T_\infty$, which is taken as a boundary condition: See Chapter 4.6.1 in the high frequency regime. Thus, after averaging, the equilibrium amplitude $T_{eq}(x)-T_\infty$ is only half of the forward amplitude.

The ballistic effect of surface temperature at $x$ = 0, which caused by periodic heating, is even more clear in Fig. 4.6. When $\omega_H\tau_{gray}$ becomes larger, the analytical solutions deviate from the Fourier limits, and reach another limit of half. The penetration

depth, which defines as the length when the temperature amplitude reaches $e^{-1}$ of the surface temperature, is

$$L_p = \frac{v_{1D}\tau_{gray}}{b}. \quad (4.17)$$

This BTE-based penetration depth $L_p$ can be rewrote as in the form as penetration depth Fourier law limit $L_{p,F}$, as shown in Eq.(4.44) that

$$L_p = L_{p,F}\frac{\sqrt{\frac{1}{2}\omega_H\tau_{gray}}}{b}. \quad (4.18)$$

This $L_p$ has exactly the same form as Regner *et al.*[126] obtained using Milne-Eddington approximation. After normalized to MFP $\Lambda_{gray}$ as shown in Fig. 4.6(b), $L_p/\Lambda_{gray}$ recovers the Fourier limit when $\omega_H\tau_{gray}$<0.1, but deviates from it at higher $\omega_H\tau_{gray}$ and approaches a constant when $\omega_H\tau_{gray}$>2. The analytical solutions to surface temperature and penetration depth have both been verified by the LBTE results, as shown in Fig. 4.6 by the black diamonds.

The penetration depth in 3D case has the same form as Eq.(4.17) except $v_{1D}$ is replaced with $v_{3D} = \beta v_g$, which $\beta$ is a coefficient dependents on the method as shown in Chapter 4.8 ($\beta$ = 2/3 in our method.). In this 3D case, if a phonon in the non *x*-direction travels one MFP, its contribution to the *x*-direction heat transport is only its projection onto the *x*-direction. Thus, in the 3D model, the temperature would roll over faster with respect to heating frequency in Fig. 4.6(a) and the ratio of penetration depth to MFP would be smaller as shown in Fig. 4.6(b).

*4.3.1.2 Surface Heat Flux and Phase Lag*

The surface heat flux for the gray BTE model is shown in Fig. 4.7(a), normalized to the Fourier limit $q''_{Fourier} = k_{Fourier}\Delta T\sqrt{\frac{\omega_H}{\alpha}}$ and verified by LBTE simulations. The BTE solution clearly converges to the Fourier result for small heater frequencies. In the opposite limit of large $\omega_H\tau_{gray}$, we find $\frac{q''_{BTE}}{q''_{Fourier}} = \frac{1}{2\sqrt{\omega_H\tau_{gray}}}$ from Eq.(4.46) in Chapter 4.6, which means Fourier's law over-predicts the heat flux caused by a prescribed surface temperature oscillation. This is equivalent to the BTE solution exhibiting a reduction in apparent thermal conductivity. From Eq.(4.45) the heat flux amplitude in this large $\omega_H\tau_{gray}$ limit is $q''_{BTE} = \frac{1}{2}v_{1D}C\Delta T$. It is independent of MFT $\tau_{gray}$, which means ballistic transport. Similar to the surface temperature, in the 3D case, the heat flux also rolls over faster than the 1D case with respect to $\omega_H\tau_{gray}$.

The phase lag of the surface equilibrium temperature as compared to net surface heat flux is $\psi_{gray} = \tan^{-1}\left(-\frac{2d\sin\phi}{1-d^2}\right)$, which is shown in Fig. 4.7(b). For small $\omega_H\tau_{gray}$ the BTE solution of Eq.(4.48) correctly approaches the well-known Fourier limit for planar periodic heating, $\psi$ = 45°. In the large $\omega_H\tau_{gray}$ limit, the heat transport gradually becomes ballistic and the phase lag decreases to zero. In the 3D case, the phase lag are exactly the same as 1D BTE solution. This is because the main difference between 3D and 1D model are only the velocities (in Fig. 4.3). However, the phase lag $\psi_{gray}$ only dependents on $\phi$ and *d*, which both are group velocity independent, as shown in Table 4-2 in Chapter 4.5.

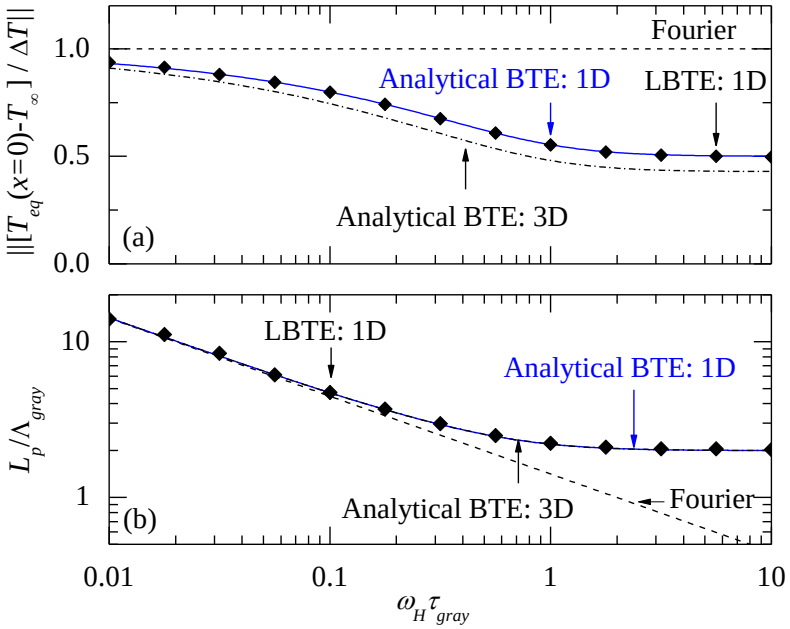


**Figure 4.6 Heating frequency dependence of (a) the surface temperature amplitude and (b) penetration depth for the gray model. The analytical BTE solutions (blue solid lines) for surface temperature from Eq.(4.42) and penetration depth from Eq.(4.44) are verified by numerical LBTE solutions (black diamonds). The BTE solutions considering 3D velocity are included for comparison (black dot dashed lines). The Fourier limits (dashed) are also shown for comparison at low heating frequency.**

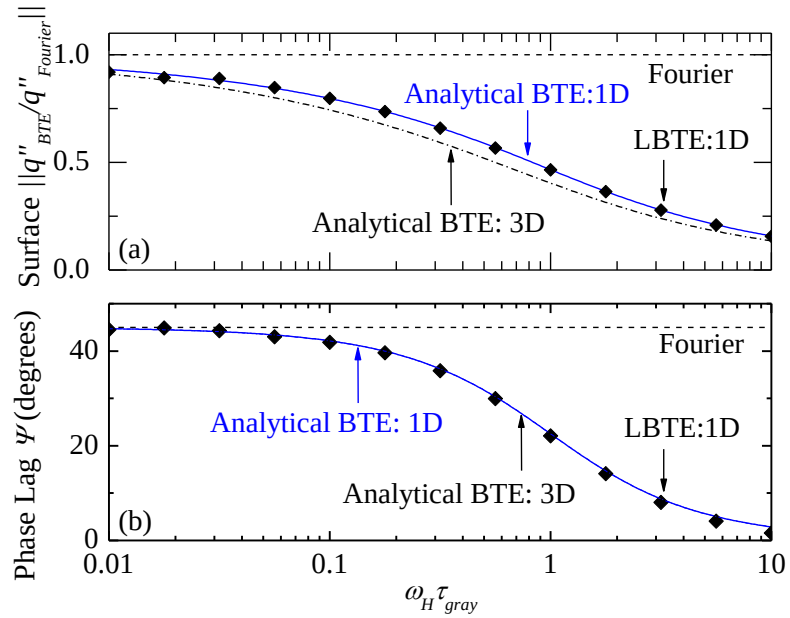


**Figure 4.7 Heating frequency dependence of the gray BTE results for (a) the amplitude of surface heat flux, and (b) phase lag of the surface temperature compared to surface heat flux. The analytical BTE solution of surface heat flux from Eq.(4.46) and phase lag from Eq.(4.48) (blue solid lines) are verified by a numerical LBTE solution (black diamonds). The BTE solutions considering 3D velocity**

**are also discussed (black dot dashed lines). The Fourier limits (dashed lines) are recovered at low heating frequency.**

*4.3.1.3 Apparent Thermal Conductivity of Gray Model: Dependence on Heater Frequency or Penetration Depth*

The $\omega_H$-dependent apparent thermal conductivity, which is defined in Eq.(4.4) by the gray model, is shown in Fig.4.8(a). When $\omega_H \tau_\omega$ increases, $k_{BTE}/k_{Fourier}$ decreases monotonically from unity to zero. We also applied the similar model on 3D case (as parameters discussed in Chapter 4.8). Both the 1D and 3D gray model have the same heating frequency dependence of apparent thermal conductivity.

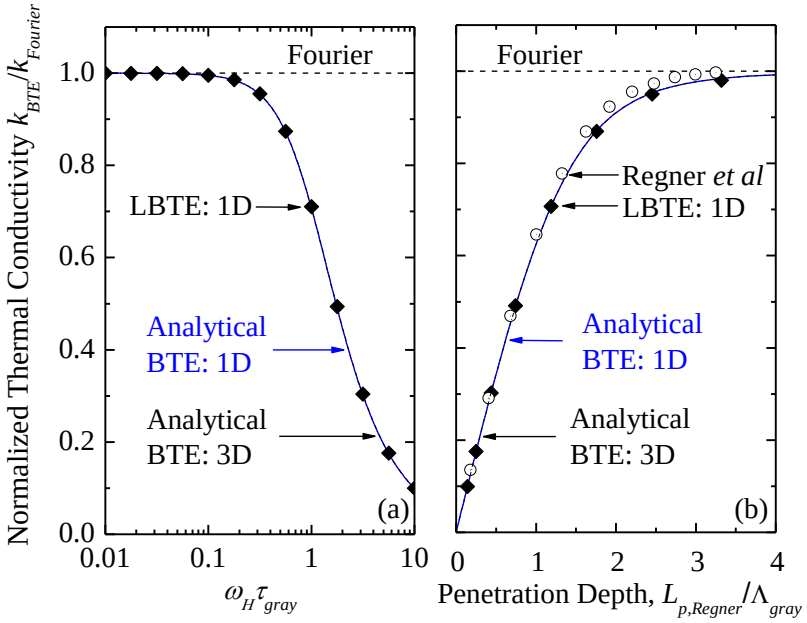


**Figure 4.8 Normalized apparent thermal conductivity of Si at 300 K for the gray model, as functions of (a) heating frequency and (b) Fourier-law penetration depth. The analytical BTE solutions of Eq.(4.4) (solid lines) and numerical LBTE results (black diamonds) are in excellent agreement with each other, and both recover the classical Fourier limit (dashed lines) for (a) low heating frequency and (b) large penetration depth. In (b), the penetration depth is normalized to the gray MFP $\Lambda_{gray}$.**

Because of the emphasis on MFPs in this field, it is common to transform $\omega_H$ to a corresponding Fourier-law penetration depth using $L_{p,KC} = \sqrt{\frac{2\alpha_{low}}{\omega_H}}$, where the subscript KC denotes the Koh & Cahill treatment[25] and $\alpha_{low}$ is the thermal diffusivity in the limit of low heating frequency, *e.g.*, the classical bulk value. In Koh & Cahill's approach[25], $L_{p,KC}$ acts as a cutoff threshold such that phonons with bulk MFPs longer than $L_{p,KC}$ do not contribute at all to heat conduction. Regner *et al.*[26] used a very similar cutoff conduction except that the critical penetration depth was defined using the apparent thermal diffusivity, namely, $L_{p,Regner} = \sqrt{\frac{2\alpha(f_H)}{\omega_H}}$ where now $\alpha(f_H)$ itself depends on heater frequency through $k_{app}(f_H)$. In the low-frequency limit, $L_{p,Regner} = L_{p,KC} = L_p$ where the

latter is the $e^{-1}$ penetration depth for the BTE solution given in Eq. (4.44); while at high frequency $L_{p,Regner} < L_{p,KC} < L_p$. To facilitate comparisons with the LBTE results of Regner *et al.*[26], Fig. 4.8(b) plots our results in terms of $L_{p,Regner}$. The comparison shows excellent agreement between our analytical and LBTE solutions over the entire $L_p$ range. Furthermore, it is reassuring that these results for $k_{BTE}$ also exhibit very good agreement with the LBTE results of Regner *et al.*[26] even though the two approaches began with different surface forcing conditions (prescribed $T^+$ in our case; prescribed $q$ in Ref.[26]). Figure4.8(b) does exhibit some minor disagreement (~2.7 %) in the transition regime although the reasons for this are not known.

### 4.3.2 Non-gray Model: Heating Frequency Dependent Thermal Conductivity

To account for the typically broad distribution of phonon mean free paths[18, 20, 78] we incorporated the phonon MFP distribution in Eq.(4.8) and obtained non-gray $k_{app}(f_H)$ as shown in Fig. 4.9. The non-gray model captures the characteristic of the long MFP tail, which results in a stronger heating frequency dependence than in the gray model. Although the measurements by Koh & Cahill[25] of natural Si did not exhibit any clear $f_H$ effect, that experiment was limited to $f_H$ =10 MHz, which according to the calculations of Fig. 4.9 corresponds to a reduction by less than 3% which likely is difficult to observe above experimental noise.

However, Koh and Cahill observed strongly $f_H$-dependent $k_{app}$ for several alloys, such as an undoped $Si_{0.4}Ge_{0.6}$ film of thickness 6 μm. For comparison with the present non-gray model, we normalize those measurements using a bulk reference value for undoped $Si_{0.4}Ge_{0.6}$ of $k \approx 8.3$ W/m-K[129]. To model the $Si_{0.4}Ge_{0.6}$ we use the virtual crystal approximation introduced by Abeles[47] and using the BvK dispersion[67], based on the averaged density of primitive unit cells of $2.3\times10^{28}$ $m^{-3}$ and sound velocity of 4630 m/s. The main scattering mechanism in $Si_{0.4}Ge_{0.6}$ is impurity scattering. The impurity scattering coefficient $A_{impurity}=6.7\times10^{-42}$ $s^3$ obtained by fitting to the bulk thermal conductivity $k$ = 8.3 W/m-K. The resulting $k_{app}(f_H)$ for the alloy is calculated from Eq. (4.9) and shown in Fig. 4.9 (red line). Comparing the non-gray results for Si and $Si_{0.4}Ge_{0.6}$ reveals the important fact that the $k_{app}$ suppression occurs at much lower frequencies in the alloy single crystal than in the pure single crystal. For example, at $f_H$ = 10 MHz, the reduction is only 2.7% for Si but 25% for $Si_{0.4}Ge_{0.6}$. This indicates that phonons with MFTs large compared to $f_H^{-1}$ play a more important role in the alloy than in the pure crystal.

Figure 4.9 also compares our $Si_{0.4}Ge_{0.6}$ calculation with the corresponding experimental data from Ref. [25]. The measurements have the same general trend show an even stronger $f_H$ effect. There are several possible reasons for the discrepancy. Due to the very broad MFP distribution expected for SiGe[18, 79] the film thickness of 6 μm may cause additional suppression of the apparent thermal conductivity in the experiment, which is not captured in the present calculation for a semi-infinite substrate. A similar size-effect reduction may arise from the finite Gaussian beam radii used in the experiment (6.5-15 μm), whereas the model deals with an infinite plane source. Although these calculations cannot be directly compared to Koh and Cahill's

measurement[25], the results still are important because they give a rigorous BTE explanation of the strong $f_H$ effect on $k_{app}$ in semiconductor alloys even when $f_H$ is orders of magnitude lower than the dominant thermal phonon frequencies (~10 MHz compared to ~THz).

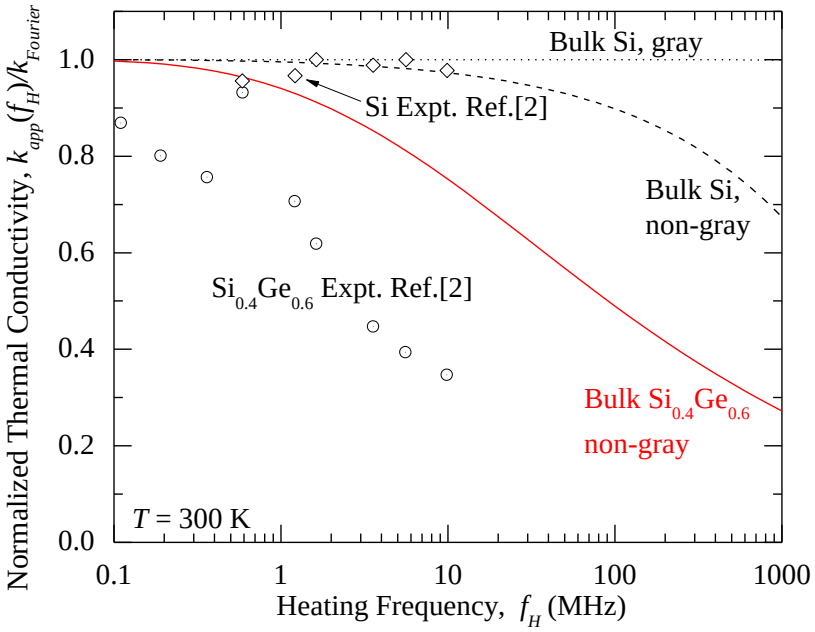


**Figure 4.9 Heating frequency dependence of thermal conductivity for Si (black dashed line) and $Si_{0.4}Ge_{0.6}$ (red solid line) for the non-gray BTE model described in the text. The measurements[25] (points) of $Si_{0.4}Ge_{0.6}$ and Si are also included for comparison.**

### 4.3.3 Measuring Accumulation Function A($\tau_{bulk}$): a Virtual Experiment

In Fig. 4.10 we consider a virtual experiment to measure the accumulation function using the phase difference between surface heat flux and temperature. We will still start from the heating frequency $f_H$ dependent thermal conductivity $k_{app}(f_H)$ in Fig. 4.9 (non-gray model). Then, we transform it to apparent penetration dependent $L_{p,Regner}$ or characteristic time $t_c$ dependent thermal conductivity as shown in Fig. 4.10(b) and (c) (solid lines). In Fig. 4.10(b), the penetration depth dependent thermal conductivity $k_{app}(L_{p,Regner})/k_{Fourier}$ (red curve) does not match the accumulation function with respect to MFP (dashed curve). However, in Fig. 4.10(c), the $k_{app}(t_c)/k_{Fourier}$ and MFT accumulation function A($\tau_{bulk}$) has much better agreement(compare solid and dashed curves), where the characteristic time $t_c$ is related to heating frequency by $t_c \approx \frac{0.28}{f_H}$, as discussed in Sec. IID. Thus, the MFT dependent thermal conductivity is used to construct the accumulation function with respect to MFT.

This construction can be understood from the $x$-axis of the accumulation function. In the time domain in Fig. 4.10(c), the characteristic time $t_c$ and MFT $\tau_\omega$ are the axis. As we discussed in Fig. 4.4(a), the kernel function $B_t$ acting as a sampling function, thus it cuts the phonon with MFT $\tau_\omega$ longer than the characteristic time $t_c$. The physical meaning is

that phonon with MFT $\tau_\omega$ longer than $t_c$ would not conduct heat. Thus, $f_H$ is directly related to cutoff MFT and the measured apparent thermal conductivity can be directly used to probe the thermal conductivity distribution over MFT. This means the result of approximation method in Eq.(4.16) can be used to probe accumulation function over MFT.

However, in the length domain in Fig. 4.10(b), the accumulation function with respect to MFP $\alpha(\Lambda_{bulk})$ and normalized penetration depth dependent apparent thermal conductivity does not agree with each other. Let's first consider Koh and Cahill's definition that $L_{p,KC} = \sqrt{\frac{2\alpha_{low}}{\omega_H}} \propto \frac{1}{\sqrt{f_H}}$. However, the MFP $\Lambda_{bulk} \propto \tau_\omega \propto \frac{1}{f_H}$. Thus, the MFP $\Lambda_{bulk}$ and $L_{p,KC}$ have different power law with respect to heating frequency $f_H$. Then, we consider the apparent penetration depth $L_{p,Regner} = \sqrt{\frac{2\alpha(f_H)}{\omega_H}}$ by Regner *et al.*[26] with the thermal diffusivity $\alpha(f_H)$ also depends on heating frequency $f_H$. This treatment make apparent penetration depth $L_{p,Regner}$ also have the same heat frequency $f_H$ dependence (which means the width of the solid and dashed curves in Fig. 4.10(b) are about the same.). However, the heating frequency dependent thermal conductivity $k_{app}(L_{p,Regner})/k_{Fourier}$ still cannot recover the accumulation function $A(\Lambda_{bulk})$. Possible reason may be caused by using the macroscopic concept, such as the thermal diffusivity $\alpha(f_H)$ which included all the phonons with different MFPs, to describe the microscope concept cutoff MFP.

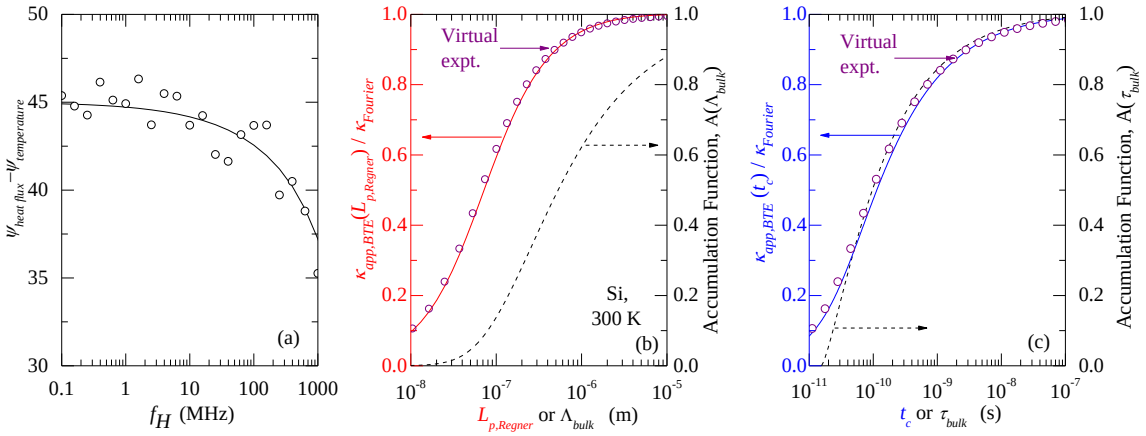


**Figure 4.10 (a) Heating frequency dependent phase lag (black solid line) and phase lag with 2° error by the virtual experiment (empty circle) (b) Penetration depth dependent thermal conductivity using bulk MFT calculated by Matthiessen's rule combining different scattering mechanisms(red solid line) and using fitted MFT in virtual experiment (empty circle), and accumulation function with respect MFP (black dashed line) (3) Characteristic time $t_c$ dependent thermal conductivity by calculation (blue solid) and virtual experiment fitting (empty circle), and expected actual accumulation function with respect to MFT (black dashed).**

To explain how this work can be used for experiment and how heating frequency $f_H$ dependent thermal conductivity can be used to construct accumulation function $A(\tau_{bulk})$ with respect to MFT, we also did a virtual experiment measuring the temperature phase lag as shown in Fig. 4.10(a). Since measurement always has error bars, we randomize the phase lag with 2 degree of error to represent the measurement error. From this

heating frequency dependent phase lag as the measured data, we can proceed to obtain the apparent thermal conductivity, as the flow chart shown in Fig. 4.1. We first fit this phase lag with a general bulk MFT $\tau_{bulk}^{-1} = D\omega^n$ by the least square fitting and find $D$=1.433×10$^{-19}$ s$^3$ and $m$=1.995. We expect $D$ and $m$ to be 1.528×10$^{-19}$ s$^3$ and 2, respectively, which the fitting agrees. The power m≈2 means umklapp scattering dominates for Si at 300 K. With this MFT, we obtain the heating frequency dependent thermal conductivity $k(f_H)$ by using Eq.(4.9), as shown by the void circles in Fig. 4.10(b) and (c).

## 4.4 Summary and Conclusions

An analytical solution to the BTE for the periodic plane-source heating problem has been obtained based on the gray MFT model. This model has been verified by our LBTE simulations and also the LBTE from recent literature[26]. The BTE solution has also been extended to non-gray MFT regime with the BvK dispersion. This model give a quantitatively derivation to construct accumulation function with respect to MTF from heating frequency dependent thermal conductivity. It is found that the time scale description is better than the length scale description to describe the frequency dependent thermal conductivity. The fundamental reason for this reduction is that phonons with MFT longer than characteristic time do not conduct heat. The time scale description is cleaner than length scale description because it does not introduce other macroscopic properties such as diffusivity. This theory has been applied to Si and SiGe and it agrees with experiments that SiGe is heating frequency dependent but Si is negligible dependent. This theory has also been applied to a virtual experiment which fitting the temperature and surface heat flux phase lag to obtain the general form of MFT, then reconstruct the characteristic time dependent thermal conductivity. It agrees very well with the accumulation function with respect to MFT in three to four order of magnitude range of time, which verified our approximation method in Eq.(4.16) for thermal accumulation function with respect to MFT.

## 4.5 Appendix A: Analytical Solutions to BTE in Forward and Backward Direction

This appendix describes the solution of the BTE, Eq. (4.1). Rather than directly solving for the distribution function, it is usually to make the analogy to thermal radiation and use phonon intensity[130]. Thus, the phonon intensity per unit time, per unit area, per phonon frequency, and per unit solid angle is

$$I_\omega = \sum_s \left| v_{\omega,s} \right| \hbar\omega D(\omega) f_\omega , \tag{4.19}$$

where $s$ represents the polarizations and $D(\omega)$ is the density of states of the $s$-th branch. To simplify the solution, we restrict the polarization to single-branch. The three acoustic branches are lumped into a single one. Good agreement with experiment for both bulk[85] and nanowire[45] in literature indicates this lumped approximation is a good

evaluation. The optical modes are neglected. They don't contribute much to the thermal conductivity due to their small group velocity. Thus, the BTE in Eq.(4.1) in the case of Fig. 4.3(a) is recast into the form of

$$\frac{\partial I_\omega}{\partial t} + v_{1D}\frac{\partial I_\omega}{\partial x} = \frac{I_\omega^0 - I_\omega}{\tau_\omega} \tag{4.20}$$

where $v_{1D} = \frac{v_\omega}{\sqrt{3}}$ is the effective group velocity in the *x*-direction and $I_\omega^0$ is the equilibrium phonon intensity. Strictly, this equilibrium flux includes all phonon frequencies and considers phonon interactions between different phonon frequencies[60, 131]. This is trivial for the gray MFT solution since there is only one $\omega$ to consider. However, in the general non-gray case the BTE can only be solved numerically, using techniques such as Monte Carlo[131], discrete ordinates[132], finite volumes[133], or the LBTE method[26]. On the other hand, analytical solutions have great advantages for understanding the essential physics and reducing computational time cost. To facilitate such an analytical solution for the general non-gray case, we assume that the true $I_\omega^0$ integral can be approximated adequately by a simpler form whereby phonons with the same frequency reach their own equilibrium. This approach has been used previously[60, 124], and the resulting "frequency-integrated gray-medium" treatment was found to yield surprisingly good agreement with a numerical solution of the full non-gray BTE for Si and PbSe.[124] With the governing equation in Eq.(4.20) and periodic heating boundary conditions described in the next subsection, the BTE is analytically solvable.

The above Eq.(4.20) can be solve by different approximation methods, such as two flux (or Schuster-Schwarzschild) model or Milne-Eddington model[134], that both assuming the phonon intensity is isotropic but different over the forward and backward directions[134] respectively (Their difference are discussed in Chapter 4.8.). We multiply Eq.(4.20) by angle dependent term $\mu$ and integrate it over forward or backward hemispheres of solid angle. Thus, the BTE in Eq.(4.20) separates into two coupled equations with respect to forward flux $q^+$ and backward flux $q^-$. In the one dimentional transport in Fig. 4.3(a), $\mu$ = 1. We will first study this case and discuss the general case of Fig. 4.3(b) in Chapter 4.8. In the forward direction, the Eq.(4.20) of gray model is expressed as

$$\frac{\partial q^+}{\partial t} + v_{1D}\frac{\partial q^+}{\partial x} = \frac{q^0 - q^+}{\tau_{gray}}. \tag{4.21}$$

where the equilibrium flux $q_\omega^0$ couples the forward and backward fluxes and is simplified as

$$q^0 = \tfrac{1}{2}\left(q^+ + q^-\right). \tag{4.22}$$

The counterpart equation in the backward direction has the same form except with $q^-$ instead of $q^+$. With the forward and backward heat flux, the net heat flux is convenient to be expressed as

$$q''_{net}\left(x,t\right) = q^+ - q^-. \tag{4.23}$$

Substituting Eq. (4.22) into Eq. (4.21), after some algebraic manipulation a pair of equations for the forward and backward direction are obtained,

$$\tau_{gray}\frac{\partial^2 q^+}{\partial t^2}+\frac{\partial q^+}{\partial t}-\tau_{gray}v_{1D}^2\frac{\partial^2 q^+}{\partial x^2}=0 \tag{4.24}$$

and

$$\tau_{gray}\frac{\partial^2 q^-}{\partial t^2}+\frac{\partial q^-}{\partial t}-\tau_{gray}v_{1D}^2\frac{\partial^2 q^-}{\partial x^2}=0\,. \tag{4.25}$$

For the boundary conditions, a sinusoidal temperature boundary condition is used in the positive direction at $x = 0$, as shown in Eq.(4.2). Since the domain is semi-infinite, deep inside the body the distribution must return to the equilibrium intensity corresponding to the ambient temperature, namely

$$T^+\left(x=\infty,t\right)=T^-\left(x=\infty,t\right)=T_\infty\,. \tag{4.26}$$

To transform these $T$ boundary conditions to corresponding constraints on $q^+$ and $q^-$, we linearize the response. The temperature oscillations of the heat source are limited to $\Delta T<<T_\infty$, which is typical in the measurements[20, 25, 28, 118]. In this case, the temperature variation is a linear response to the heat flux variation in the each direction, such as

$$dq^+\approx\tfrac{1}{2}v_{1D}CdT^+=\tfrac{1}{2}v_{1D}dU^+, \tag{4.27}$$

where $C$ is the volumetric specific heat and $U$ is the volumetric energy density. The factor of $\frac{1}{2}$ arises from only integrating over half of the hemisphere. Using Eq. (4.27), both temperature boundary conditions from Eqs.(4.2) and (4.26) are transformed to energy flux boundary conditions.

### 4.5.1 Dimensionless Analysis and Forward Direction Solution With Gray MFT

For convenience we non-dimensionalize the governing equations (4.24) and (4.25) and boundary conditions (4.2) and (4.26). We define the dimensionless time as $\gamma=\frac{t}{\tau_{gray}}$, location as $\chi=\frac{x}{v_{1D}\tau_{gray}}$, and forward energy flux as

$$Q^+\left(x,t\right)=\frac{q^+\left(x,t\right)-q^+\left(x=\infty\right)}{q^+\left(x=0,t=0\right)-q^+\left(x=\infty\right)}, \tag{4.28}$$

with a similar result for $Q^-_{gray}$ after substituting $q^+\rightarrow q^-$, except keep the denominator $q^+\left(x=0,t=0\right)$ term the same. At $x\rightarrow\infty$, from Eqs. (4.26) and (4.27) we have $q^+\left(x=\infty,t\right)=q^-\left(x=\infty,t\right)=q_\infty$, and governing Eq. (4.24) simplifies to

$$\frac{\partial^2 Q^+}{\partial\gamma^2}+\frac{\partial Q^+}{\partial\gamma}-\frac{\partial^2 Q^+}{\partial\chi^2}=0\,. \tag{4.29}$$

Applying Eqs. (4.27) and (4.28) to Eqs. (4.2) and (4.26), we obtain the boundary conditions

$$Q^+\left(\chi=0,\gamma\right)=\exp\left(i\omega_H\tau_{gray}\gamma\right) \tag{4.30}$$

and

$$Q^{+}\left(\chi=\infty,\gamma\right)=0. \tag{4.31}$$

Now the governing Eq. (4.29), which is hyperbolic telegraph type, can be solved by a standard Laplace transform method. After taking the Laplace transform of Eqs.(4.29)-(4.31) with respect to time, the resulting ordinary differential equation in $\chi$ is readily solved, and finally an inverse Laplace transform used to obtain the time domain solution. During the inverse transform, the singularity problem is overcome using the Cauchy integral theorem[135 ]. Finally, we obtain the dimensionless temperature in the forward direction as

$$Q^{+}_{gray}\left(\chi,\gamma\right)=\exp\left(-b\chi\right)\exp\left(i\omega_{H}\tau_{gray}\gamma-ia\chi\right), \tag{4.32}$$

where *a* and *b* are purely real and are given in Table 4-2.

### 4.5.2 Solution in the Backward Direction with Gray MFT

Beginning from Eq.(4.25), the backward-direction counterpart of Eq.(4.29) is

$$\frac{\partial^{2}Q^{-}}{\partial\gamma^{2}}+\frac{\partial Q^{-}}{\partial\gamma}-\frac{\partial^{2}Q^{-}}{\partial\chi^{2}}=0 \tag{4.33}$$

However, there is only one obvious boundary condition that

$$Q^{-}\left(x=\infty,t\right)=0. \tag{4.34}$$

At $x$=0, the heat flux in the negative direction is a depth-integrated response to the positive direction heat flux, which is not specified in advance (recall that for convenience our boundary condition at $x$=0 was defined purely in terms of $Q^{+}$). Without one more boundary condition it would appear that we cannot solve Eq.(4.33). However, since the form of the governing equations in the forward and backward directions are exactly the same, we seek a solution of Eq. (4.33) with the same form as Eq.(4.32) while allowing for different amplitude and phase,

$$Q^{-}\left(x,t\right)=d\exp\left(-b\chi\right)\exp\left(i\omega_{H}\tau_{gray}\gamma-ia\chi+\phi\right). \tag{4.35}$$

Here $d$ is the amplitude coefficient and $\phi$ is the phase shift, which are determined by energy conservation as follows. Since there is no heat generation in the material, it must always be true that

$$\nabla\cdot q''_{net}+\frac{\partial U}{\partial t}=0, \tag{4.36}$$

where the phonon energy density in one dimensional transport in Fig. 4.3(a) is

$$U=\frac{q^{+}+q^{-}}{v_{1D}}\quad. \tag{4.37}$$

Substituting the forward and backward solutions into Eq.(4.36), for the real part we obtain

$$\begin{aligned}&\left[-\left(a-\omega_{H}\tau_{gray}\right)+d\left(a+\omega_{H}\tau_{gray}\right)\cos\phi+db\sin\phi\right]\sin\left(\omega_{H}t\right)\\&+\left[b+d\left(a+\omega_{H}\tau_{gray}\right)\sin\phi-db\cos\phi\right]\cos\left(\omega_{H}t\right)=0\end{aligned}, \tag{4.38}$$

where the coefficients $a$, $b$, $\phi$, and $d$ are all only functions of $\omega_H \tau_{gray}$. Since Eq (4.38) is valid at any time, the coefficients of $\sin(\omega_H t)$ and $\cos(\omega_H t)$ must both be zero. Thus, we obtain

$$d = \frac{b}{a+\omega_H \tau_{gray}} \tag{4.39}$$

and

$$\cos\phi = \frac{b}{a}. \tag{4.40}$$

as given in Table 4-2.

## 4.6 Appendix B: Analytical Solution of Temperature and Heat Flux to Gray Model

Using the positive and negative solution of flux from the previous appendix, we now obtain the equilibrium temperature, penetration depth, net heat flux, phase lag on the surface, and apparent thermal conductivity.

**Table 4-2 Key coefficients of the analytical BTE solution, including simplified limiting forms in low- and high-frequency limits. These expressions are derived from gray $\tau_{gray}$, but they can also be extended to non-gray regime with $\tau_\omega$ as shown in Sec. IIB. For convenience to use it in the non-gray model, we express the MFT as $\tau_\omega$.**

| Coefficient | Low $\omega_H$ limit | High $\omega_H$ limit |
|---|---|---|
| $a = \sqrt{\frac{\omega_H\tau_\omega}{2}}\sqrt{\omega_H\tau_\omega + \sqrt{(\omega_H\tau_\omega)^2+1}}$ | $\sqrt{\frac{\omega_H\tau_\omega}{2}}\left(1+\frac{\omega_H\tau_\omega}{2}\right) \approx \sqrt{\frac{\omega_H\tau_\omega}{2}}$ | $\omega_H\tau_\omega + \frac{1}{8\omega_H\tau_\omega} \approx \omega_H\tau_\omega$ |
| $b = \sqrt{\frac{\omega_H\tau_\omega}{2}}\sqrt{-\omega_H\tau_\omega + \sqrt{(\omega_H\tau_\omega)^2+1}}$ | $\sqrt{\frac{\omega_H\tau_\omega}{2}}\left(1-\frac{\omega_H\tau_\omega}{2}\right) \approx \sqrt{\frac{\omega_H\tau_\omega}{2}}$ | $\frac{1}{2} - \frac{1}{16(\omega_H\tau_\omega)^2} \approx \frac{1}{2}$ |
| $\cos\phi = \frac{b}{a}$ | $1-\omega_H\tau_\omega \approx 1$ | $\frac{1}{4\omega_H\tau_\omega} \approx 0$ |
| $\sin\phi = -2b$ | $-\sqrt{2\omega_H\tau_\omega} \approx 0$ | $-1+\frac{1}{8(\omega_H\tau_\omega)^2} \approx -1$ |
| $d = \frac{b}{a+\omega_H\tau_\omega}$ | $1-\sqrt{2\omega_H\tau_\omega} \approx 1$ | $\frac{1}{4\omega_H\tau_\omega} \approx 0$ |

### 4.6.1 Temperature and Penetration Depth

The equilibrium temperature is obtained by conserving the total energy density[45]. From the linear response of Eq. (4.27) the equilibrium temperature is expressed as

$$U_{eq}(x,t) - U_\infty = C\left[T_{eq}(x,t) - T_\infty\right]. \tag{4.41}$$

Thus, the amplitude of the equilibrium temperature oscillation is

$$\left\| \frac{T_{eq}(x)-T_\infty}{\Delta T} \right\| = \frac{1}{2}\sqrt{1+d^2+2d\cos\phi}\exp\left(-x\frac{b}{v_{1D}\tau_{gray}}\right), \tag{4.42}$$

where the time dependent term $\exp\left(i\omega_H t - ix\frac{a}{v_{1D}\tau_{gray}}\right)$ goes to one when we calculate the amplitude. To facilitate comparisons with the Fourier limit, it is convenient to re-cast this result in terms of the thermal diffusivity $\alpha$ by using $\alpha = v_{1D}^2\tau_{gray} = \frac{1}{3}v_g^2\tau_{gray}$,

$$\left\|\frac{T_{eq}(x)-T_\infty}{\Delta T}\right\| = \frac{1}{2}\sqrt{1+d^2+2d\cos\phi}\exp\left(-x\sqrt{\frac{\omega_H}{2\alpha}}\frac{b}{\sqrt{\frac{\omega_H\tau_{gray}}{2}}}\right). \tag{4.43}$$

Equation (4.43) also directly gives the thermal penetration depth, $L_p$,

$$L_p = \sqrt{\frac{2\alpha}{\omega_H}}\frac{\sqrt{\frac{1}{2}\omega_H\tau_{gray}}}{b} = L_{p,F}\frac{\sqrt{\frac{1}{2}\omega_H\tau_{gray}}}{b}, \tag{4.44}$$

where $L_{p,F} = \sqrt{\frac{2\alpha}{\omega_H}}$ is the Fourier limit of penetration depth. Various limits of the BTE solution are shown in Table 4-3 and serve as useful checks, such as verifying that the low $\omega_H$ limit recovers the classical Fourier solution.

**Table 4-3 Low- and high-frequency limits for various key results of the gray BTE model.**

| | | Low $\omega_H\tau_\omega$ limit | High $\omega_H\tau_\omega$ limit |
|---|---|---|---|
| Temperature amplitude | $\left\|\frac{T_{eq,\omega}(x)-T_\infty}{\Delta T}\right\|$ | $\exp\left(-x\sqrt{\frac{\omega_H}{2\alpha}}\right)$ | $\frac{1}{2}\exp\left(-\frac{x}{2\sqrt{\alpha\tau_\omega}}\right)$ |
| Penetration depth | $L_p$ | $L_{p,F} = \sqrt{\frac{2\alpha}{\omega_H}}$ | $2\sqrt{\alpha\tau_\omega} = 2\Lambda_{gray}$ |
| Surface heat flux amplitude | $\left\|\frac{q''_{net}}{q''_{Fourier}}\right\|$ | 1 | $\frac{1}{2\sqrt{\omega_H\tau_\omega}}$ |
| Phase lag | $\psi_{gray}$ | $\frac{\pi}{4}$ | 0 |
| Apparent thermal conductivity | $k_{app,gray}$ | $k_{Fourier}$ | $\frac{k_{Fourier}}{\omega_H\tau_\omega}$ |

### 4.6.2 Heat Flux

The net heat flux is calculated by Eq. (4.23). At the surface, $x$=0, the heat flux amplitude is

$$\left\|q''_{net}\right\| = \frac{1}{2}v_{1D}C\Delta T\sqrt{1+d^2-2d\cos(\phi)}. \tag{4.45}$$

Normalized surface heat flux to its Fourier limit we find

$$\left\|\frac{q''_{net}}{q''_{Fourier}}\right\| = \frac{1}{2}\sqrt{\frac{1+d^2-2d\cos(\phi)}{\omega_H\tau_{gray}}}, \tag{4.46}$$

which correctly reduces to unity in the low $\omega_H\tau_{gray}$ limit, as shown in Table 4-3.

### 4.6.3 Phase Lag

For thermal conductivity experiments, measuring the phase lag between surface temperature and heat flux is more practical than measuring the temperature or heat flux

amplitude directly, because the phase lag is less sensitive than amplitude to intensity instabilities[28]. Thus, the phase lag between the surface temperature and heat flux can be measured with higher accuracy. To extract the phase lag, we express the ratio of Eqs.(acl) and (aci) as a complex function with the purely real amplitude $R$ and phase lag $\Psi_{gray}$,

$$\frac{q''_{net}(x,t)}{T_{eq}(x,t)-T_{\infty}} = R_{amp,gray}\exp\left(i\psi_{gray}\right). \tag{4.47}$$

The time $t$ and space $x$ related term are all cancelled. Substituting for $q''_{net}(x,t)$ and $T_{eq}(x,t)$, the phase lag is found to be

$$\tan\left(\psi_{gray}\right) = -\frac{2d\sin\phi}{1-d^2} \tag{4.48}$$

The Fourier result is again recovered in the low $\omega_H \tau_{gray}$ limit, as shown in Table 4-3.

## 4.7 Appendix C: Relationship Between 3D and 1D Group Velocity

We consider the relationship between the 1D velocity $v_{1D}$ and the actual group velocity $v_\omega$ in this Appendix. The present work uses a periodic heat source in the *y*-*z* plane. Due to the translational symmetry of the heating surface and the fact that the material's dispersion relation is isotropic, the net heat flow must propagate normal to the *y*-*z* plane (*i.e.*, along the *x*-axis), suggesting a 1D treatment. However, the constituent phonons still travel in all 4π steradians, so some care is required in converting their actual group velocities to an equivalent 1D velocity $v_{1D}$. In the 3D phonon dispersion, all phonons of frequency $\omega$ travel with a group velocity of magnitude $v_\omega$. It is well established that when scattering is dominated by momentum-conserving processes, the equivalent 1D velocity of an energy wave is simply $v_{1D} = \frac{1}{\sqrt{3}} v_\omega$.Ref.([136, 137]) In ideal gases this gives the relationship between the thermal velocity and sound velocity[136]. In solids and liquids at low temperature the phenomenon is known as second sound[138, 139], where it has been studied by theories[140-142] and experiments in helium[143], NaF[144, 145], NaI[145], $SiTiO_3$ (Ref. [146]), *etc*. More fundamentally, this $\frac{1}{\sqrt{3}}$ factor can also be understood as a consequence of collisions randomizing the directions of the velocity vectors[136], resulting in the effective 1D velocity $v_{1D}$ for energy propagation.

This velocity relation can also be verified by comparing the equilibrium temperature in Eq.(4.42) (or surface heat flux) at low heating frequency $\omega_H$ with the Fourier limit. The Fourier limit of temperature amplitude is $\left\| \frac{T_{eq}(x,t)-T_{\infty}}{\Delta T} \right\| = \exp\left(-x\sqrt{\frac{\omega_H}{2\alpha}}\right)$. Comparing with our 1D model in Eq.(4.42), we can obtain their relation that $v_{1D} = \sqrt{\frac{\alpha}{\tau_{gray}}} = \frac{1}{\sqrt{3}} v_\omega$.

## 4.8 Appendix D: Relationship Between General 3D and 1D Velocity Model

This appendix extends the BTE solution from 1D velocity $v_{1D}$ in Fig. 4.3(a) to a more general case in Fig. 4.3(b). The difference of several approximation methods, such Schuster-Schwarzschild method, Milne-Eddington method, and our method are also discussed.

Similarly to Chapter 4.5, we can also obtain the governing equation in the form of phonon intensity

$$\frac{\partial I_\omega}{\partial t} + v_\omega \mu \frac{\partial I_\omega}{\partial x} = \frac{I_\omega^0 - I_\omega}{\tau_\omega}. \tag{4.49}$$

The key difference to solve the Eq.(4.49) is to deal with the angle dependence velocity $v_\omega \mu$, which is usually treated by multiplying a moment term of $\mu$ of different orders and integrate the equation over the solid angle. We also use the same assumption that the radiative intensity is isotropic but different over the forward and backward directions[134]. With this assumption, the governing equation in Eq.(4.49) can be simplified. Here, we states a general method, by firstly multiply the Eq. (4.19) by *m*-th order of moments $\mu^m$, and then integrate over the half solid angles, which is expressed in the forward direction that

$$q_\omega^+ = 2\pi \int_0^1 I_\omega^+ \mu^m d\mu . \tag{4.50}$$

The $2\pi$ is from integrating over the azimuthal angle. If $m$=0 and separating the directions between forward and backward, it is the Schuster-Schwarzschild approximation[134]. If both the $m$=0 and $m$=1 are used and integrate over full solid angle, it is the Milne-Eddington approximation[126, 134]. Since we are more interested in the heat flux, it is convenient to obtain the heat flux by choosing $m$ = 1 and separating the forward and backward directions fluxes. The heat flux in the forward direction is the first order of moment ($m$ = 1) that

$$q_\omega^+ = 2\pi \int_0^1 I_\omega \mu d\mu . \tag{4.51}$$

Thus, the BTE in the forward direction is recast into the form that

$$\frac{\partial q_\omega^+}{\partial t} + \beta v_\omega \frac{\partial q_\omega^+}{\partial x} = \frac{q_\omega^0 - q_\omega^+}{\tau_\omega}, \tag{4.52}$$

where $\beta$ is a coefficient dependents on the order of moment used ($\beta$=2/3 here for $m$=1). If we replace the $\beta v_\omega$ by effect 3D group velocity $v_{3D} = \beta v_\omega$, the Eq.(4.52) is exact the same type as Eq.(4.21). Thus, the solution to Eq.(da5) would have the same form except a coefficient difference. In the backward direction, we also use the first law of thermodynamics in Eq.(4.36), which introduced a coefficient $\eta$ when considering the solid angle integration that

$$U_\omega = \eta \frac{Q_\omega^+(x,t) + Q_\omega^-(x,t)}{v_{x,\omega}}, \tag{4.53}$$

where $\eta = 2$. We can also solve the BTE in the negative direction using the same method in Chapter 4.5 and obtain the amplitude $d_{3D}$ and phase shift $\phi_{3D}$ that

$$\tan\phi_{3D} = \frac{2\beta\eta\omega_H\tau b}{\left(\beta\eta\omega_H\tau\right)^2 - a^2 - b^2} \tag{4.54}$$

and

$$d_{3D} = -\frac{b}{\left(2\beta\eta\omega_H\tau + a\right)\sin\phi - b\cos\phi} \tag{4.55}$$

These general expressions can also be applied to the 1D case as we discussed before. When $\beta$ = 1 and $\eta$ = 1, they can exactly recover the 1D solution as shown in the Chapter 4.5 and 4.6. The general expression for temperature in Eq.(4.42), surface heat flux in Eq.(4.45), phase lag in Eq.(4.48), and apparent thermal conductivity in Eq.(4.4) are all have the same forms except replace the 1D quantities $v_{1D}$, $\phi_{1D}$, and $d_{1D}$ with 3D quantities that $v_{3D} = \beta v_{\omega}$, $\phi_{3D}$, and $d_{3D}$. All the other parameters are the same.

# Chapter 5 Thermal Boundary Conductance Crossover at Cryogenic Temperature

## 5.1 Introduction

In thermoelectrics, high figure of merit requires low thermal conductivity $\kappa$. In kinetic theory, the thermal conductivity $\kappa = Cv\Lambda/3$, where $C$ is the heat capacity per unit volume, $v$ is the group velocity, and $\Lambda$ is the mean free path. At temperature comparable or higher than the Debye temperature, $C$ is a constant at Dulong-Petit limit. In nanostructure, such as nanowire or superlattice, $\Lambda$ can be treated as constant due to boundary scattering. Thus, it would lead to $\kappa \propto Cv \propto v$. Thus, the smaller $v$, the lower $\kappa$. That's why good thermoelectric materials usually have low group velocity, such as $Bi_2Te_3$ and PbTe *etc*. However, at cryogenic temperature, heat capacity is proportional to $v^{-3}$ due to phonon freeze out effect[30]. This would lead to an opposite trend, $\kappa \propto v^{-2}$ which means the higher $v$, the lower $\kappa$. Thus, higher group velocity materials are preferred for thermoelectrics at cryogenic temperature[147], which is opposite compared to the high temperature criteria. Thus, for nanostructure, there is a crossover for thermal conductivity.

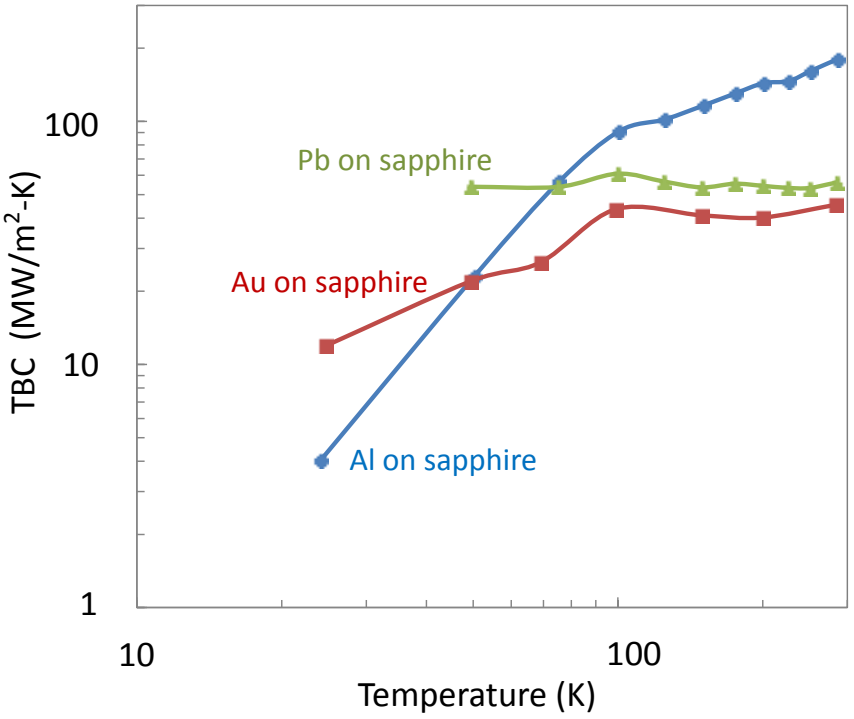


**Figure 5.1 The temperature dependence of thermal boundary conductance between different metals and sapphire, by pico-second optics technique. Data from Ref. [148].**

Since the thermal boundary conductance is also proportional to $Cv$,(Ref.[149]) the crossover phenomena also exists in thermal boundary conductance (TBC), as shown in

Fig. 5.1. Thus, the criteria of choosing higher group velocity materials at low temperature still holds. In the thin film or superlattice device, we only consider the TBC at cryogenic temperatures, because TBC dominates the total thermal resistance. For instance, at 10 K, the thermal resistance of 300nm GaAs is less than 0.02% of the resistance of the GaAs interface with Au.

To experimentally verify this criterion, considering the convenience of materials growth and resources we have, we use the $Al_xGa_{1-x}As$ thin film structure. In literature[148], this phenomenon can also be observed if we extract data of different materials from literatures and plot them in the same figure, as shown in Fig. 5.1. The TBC for Pb/sapphire (Pb: low sound velocity at 710 m/s) and Al/sapphire interface (Al: high sound velocity at 3130 m/s) has a crossover when temperature changes, which verified the criteria that high group velocity materials have lower TBC at cryogenic temperature.

## 5.2 Sample Design and Structure

The structure and dimensional parameters are shown in Fig. 5.2. The $Al_xGa_{1-x}As$ thin films, which are from our cooperators from Research Triangle Institute, are grown on GaAs substrate by metal organic chemical vapor deposition (MOCVD).

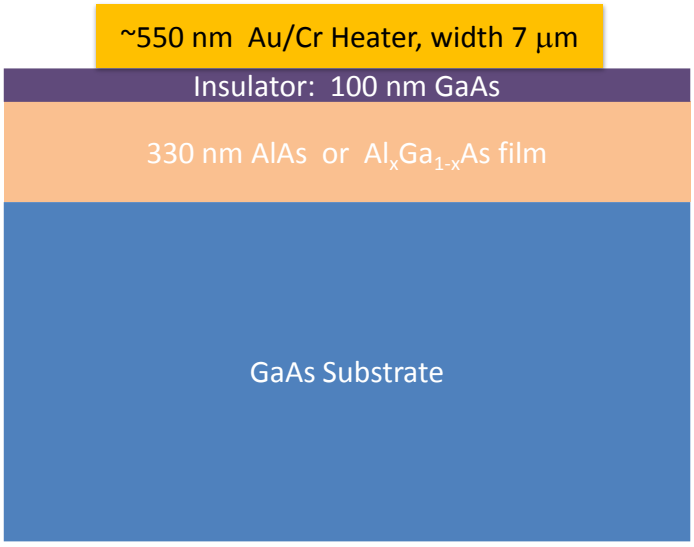


**Figure 5.2 Schematic of the film structure**

On top of the film, another layer of intrinsic GaAs with the thickness of 100 nm is also grown to provide electric insulation. We choose GaAs because we want the interfaces on top and underneath the film to be the same. Thus, if we measure the total thermal boundary resistance, it would be twice of single $GaAs/Al_xGa_{1-x}As$ interface (we assume $GaAs/Al_xGa_{1-x}As$ and $Al_xGa_{1-x}As/GaAs$ interfaces have the same TBC). Finally, a 6 mm×7 μm ×500 nm gold heater line is evaporated on the GaAs insulating layer and patterned by photolithography. The heater line width is about 16 times larger than the

sum of the film and insulating layer thickness, which makes sure that heat transfer is one dimensional inside the film. The length 6 mm is also longer than usual which make the voltage large enough for measurement at cryogenic temperature, because the resistance would decrease dramatically when temperature decreases. The copper wires are used to connect to Au pads and sockets. The Au pads side uses the silver conductive epoxy and sockets side uses soldering. The sample is mounted and connected to Gifford-McMahon closed helium cycle cryostat with the potential capability cool down to 1.7 K. However, due to some equipment problems and self-heating effects of the heater line, we only obtained a stable operation temperature at 33 K (minimum 16 K). The large current 45 mA is used to create a measurable temperature variation on the heater line due to high thermal conductivity of sample and low electrical resistivity of heater line. Thus, larger heat is generated inside the cryostat which increases the temperature.

## 5.3 Measurement Method

The thermal boundary conductance/thermal contact resistance is measured by a virtual differential 3ω method[150]. The contact resistance here can be measured by 3ω method because the contact resistance dominates the whole resistance, especially at cryogenic temperature. We firstly have a brief introduction of the 3ω method and setup of this measurement. Then, we discuss the design and structure of the samples. Finally, we discuss the measurement and follow up with a data analysis.

### 5.3.1 Introduction to 3ω Method

The 3ω method is one of the major thermal conductivity measurement methods in the frequency-domain, which can be applied to measure bulk materials[151] and thin films[150]. This method has great advantages comparing to other traditional methods, such as

- It is a small current measurement. And, the temperature variation is usually less than 1 K.
- It is a non-steady state method, with variable probe depth. Controlling the heating frequency can be used to probe different sample thickness.
- It is fast measurement method compared to steady state method which temperature stabilization is usually very long.
- It is a very accurate method. This is because the input Joule heat can be very accurately controlled by modern electronics. The thermal conductivity is determined by the slope of 3ω voltage, as shown in Fig. 5.3, and can be fitted very accurately.

Some drawbacks compared to other methods are that it needs microfabrication to obtain the heater sensor, as shown in Fig. 5.2, the 60 mm×7 μm ×500 nm gold heater line. This method also needs electrical insulation between the heater line to the sample. For electrically conductive samples, a electrical insulation layer is needed, such as the 100 nm intrinsic GaAs layer in Fig. 5.2.

### 5.3.2 Measurement System

In the system, we use a lock-in amplifier's internal sinusoidal voltage source to drive the circuit. To obtain the small $V_{3\omega}$ signal from large $V_{1\omega}$ signal (usually the $V_{3\omega}$ signal is about three orders of magnitude smaller than $V_{1\omega}$), we use a voltage subtraction circuit[152]. We add a precision resistance with the same resistance in series with the sample resistance. Then, we subtract the precision voltage from the sample voltage to cancel the 1ω voltage. Because the precision resistance has a much lower temperature coefficient of resistance, its 3rd harmonic voltage would be several orders of magnitude lower than the $V_{3\omega}$ of the sample. Thus, the leftover of the 3rd harmonic voltage $V_{3\omega}$ after subtraction is the 3rd harmonic voltage of the sample,

In this measurement, both the 1ω and 3ω voltages across the sample and the precision resistance are measured using a lock-in amplifier (Stanford Research Systems SR850). The voltage difference across the two ends of the sample is converted to a single output by AD524 amplifier chip (similarly for the precision resistor). The precision resistance uses the GenRad 1433 Series decade box, with resolution 0.01Ω. Its temperature coefficient of resistivity is about ±20 ppm/°C, much smaller than the sample's TCR of around 3000 ppm/°C. The time constant of 1 second is used for all the measurement (with frequency higher than 100 Hz). These settings were chosen to reduce the random noise and improve the signal to noise ratio. The data acquisition software is a home made LABVIEW program.

### 5.3.3 Data Analysis method

The main data processing uses the method from Ref. [150]. The total temperature difference across both the thin film and substrate $\Delta T_{total}$ is obtained by the calibrated heater line resistance, as shown in Fig. 5.4. With the heat capacity[153] at the same temperature, we can theoretically obtain the temperature difference $\Delta T_{sub}$ across the substrate (blue line in Fig. 5.3) which is the measurement of $Al_{0.84}Ga_{0.16}As$ film at 48 K. The temperature difference across the substrate $\Delta T_{sub}$ can be calculated from [150]

$$\Delta T_{sub} = \frac{P}{l\pi\kappa}\int_0^\infty \frac{\sin^2(xb)}{(xb)^2\sqrt{x^2+q^2}}dx \qquad (5.1)$$

where $P$ is the power per unit length generated by the heating line, $l$ is the length of the heater line and $b$ is its half width, $q = \sqrt{\frac{i2\omega}{\alpha}}$, and $\alpha$ is the thermal diffusivity. The slope of $\Delta T_{sub}$ can be used to measure the thermal conductivity of the substrate. Both the $\Delta T_{total}$ and $\Delta T_{sub}$ of a AlGaAs film is shown in Fig. 5.3. They are parallel to each other, which means the temperature difference between the heater line and the top of the substrate is heating frequency independent. If we only linear fit the $\Delta T_{total}$, from the slope, we can also obtain the thermal conductivity of the substrate GaAs[150].

With both the $\Delta T_{total}$ and $\Delta T_{sub}$, the temperature difference across the thin film $\Delta T_{film}$ is the subtraction of $\Delta T_{sub}$ from $\Delta T_{total}$. Because the total Joule heating power is

controlled by the heating current (which can be precisely controlled by the input current or voltage source) we can finally obtain the total thermal boundary conductance by $G = \dot{q} / \Delta T_{film}$, where $\dot{q}$ is the heat flux across heat line unit area.

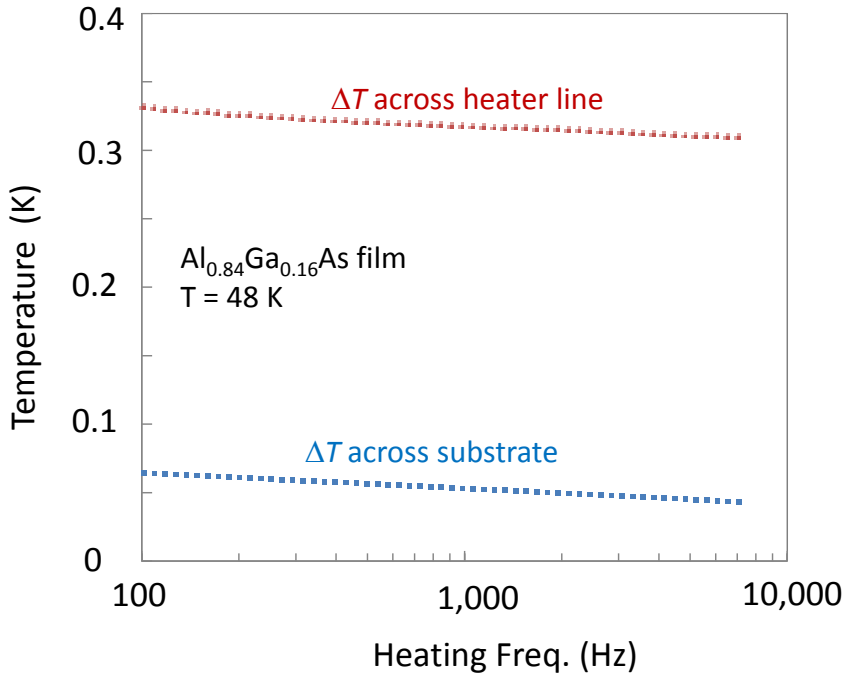


**Figure 5.3 Measured temperature difference between the Au heater line and environment (red) and calculated temperature difference across the GaAs substrate for $Al_{0.84}Ga_{0.16}As$ thin film at 48 K.**

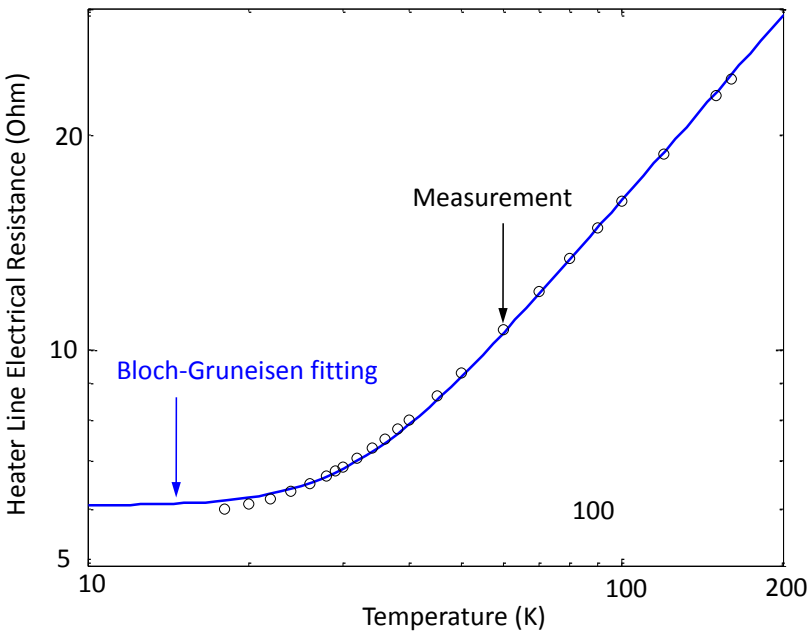


**Figure 5.4 Temperature coefficient of resistance calibration for gold heater line, and Bloch-Grüneisen fitting.**

The heating frequency is chosen between 500 to 10,000 Hz for testing to find the suitable frequency range. The penetration depth $L_p = \sqrt{\frac{\alpha}{\omega}}$ ,where $\alpha$ is the thermal diffusivity and $\omega$ is the heating frequency, is checked make sure it is smaller than the thickness of the sample. Even lower frequency (<500 Hz) is not used because the penetration depth is larger than the total sample thickness at the cryogenic temperatures. The current passed through the heater line is around 45 mA. The relationship between the $V_{3\omega}$ and $I_{1\omega}$ is checked by tuning the current. A relation of $V_{3\omega} \propto I_{1\omega}^3$ is obtained which means our measurement is in a proper range[152]. Since a voltage source is used, to improve the accuracy, a correction factor can be used to correct the error caused by the voltage source[152]. We did not apply this correction factor in the analysis because the resistance of the sample is much smaller than the resistance of the rest of the circuit.

In the measurement, one of the practical issues is the fact that heater line electrical resistance is not linear with respect to temperature any more when temperature is less than 50 K, because phonons are freezing out at these low temperatures. Thus, as shown in Fig.5.4 (blue line), we use the Bloch-Grüneisen fitting to fit the non-linear region, and obtain the new temperature coefficient of resistance. This method can be extended to temperature even close to 10 K or even lower for Au heater line[154].

## 5.4 Results and Discussion

We have measured thermal boundary conductance of three samples, with the film layer of AlAs, $Al_{0.84}Ga_{0.16}As$, and $Al_{0.72}Ga_{0.28}As$. A temperature dependent TBC has also been obtained.

### 5.4.1 Substrate thermal conductivity and setup verification

The temperature dependences of substrate GaAs thermal conductivity of all samples are shown in Fig. 5.5. The substrate thermal conductivity is obtained using Eq.(5.1). This measurement is also used as verification for the 3ω system. The measured substrate thermal conductivities of different samples agree with each other and also agree with the literature[155] within 9% at temperature greater than 50 K. For even lower temperature, since the 3ω voltage slope in Fig. 5.4 is smaller, the error bar would be larger and reaches 14%. However, since $\Delta T_{sub}$ takes less and less contribution to $\Delta T_{total}$ at lower temperature (for instance, at 48 K, $\Delta T_{sub}$ is only about 15% of $\Delta T_{total}$), the substrate thermal conductivity would affect the TBC measurement less at low temperature.

There is one practical issue on the actual temperature of the sample. It needs to be carefully considered, especially in the case of cryogenic temperature. The temperature on the cryostat temperature controller is not actual temperature of the heater line. The difference could be as large as more than 10 K at cryogenic temperature. This temperature difference is caused by the heater line self-heating. Thus, a temperature calibration process is needed. During the measurement, the cryostat temperature is controlled by the Lakeshore331 temperature controller. However, the temperature showing on the controller is the temperature of the Si diode sensor, but not the

temperature of the sample. There still has some space in distance between them. Thus, some temperature difference arises which cannot be neglected at very low temperature[71]. The temperature on Lakeshore331 is only used for temperature stabilization and controlling, but not the actual temperature of the sample. The actual sample's temperature is obtained by using the Au heater line as the thermometer. We first calibrate the resistance of the heater line, using a four probe method, by using very small current (0.5 mA) to make sure the Joule heat is small and would not cause measureable temperature rise. In the 3ω measurement with current in order of 45 mA, the electrical resistance is measured and the temperature is obtained by comparing with calibrated resistance data.

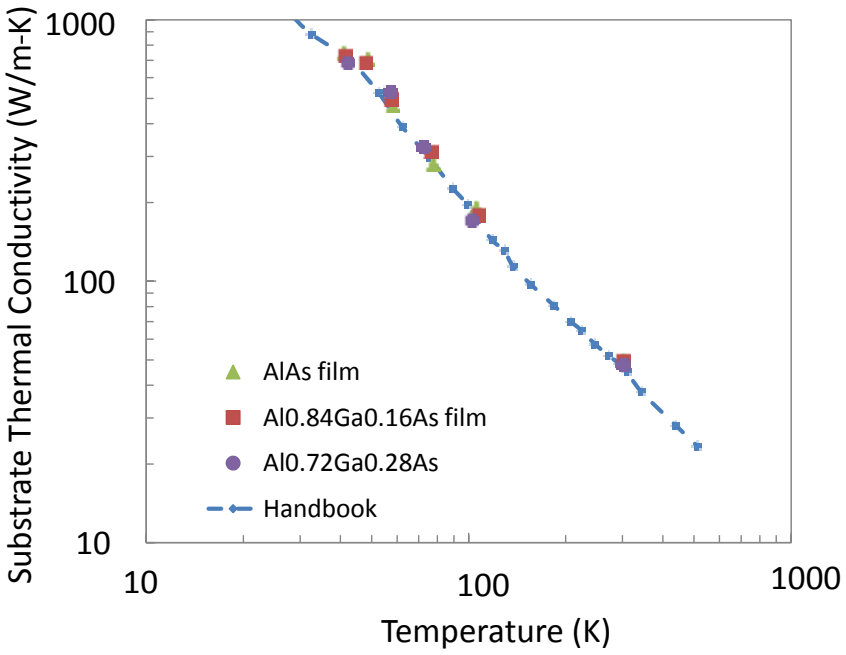


**Figure 5.5 Measured GaAs substrate thermal conductivity for samples with three different films, and the comparison with GaAs literature[156].**

### 5.4.2 Thermal boundary conductance crossover

The temperature dependence of total thermal boundary conductance is showing in Fig. 5.6. The measured thermal boundary conductance is actually all the contributions from the Au heater line to the substrate top surface. Comparing the width of heater line (7μm) to the thickness of the film (330 nm), the transport can be treated as one dimensional. The heat conduction can be treated as one dimensional. Considering thermal conductance of the 100nm GaAs insulator layer and 330nm film layer, they are orders of magnitude larger than the thermal boundary conductance at low temperature, the measured conductance is only the sum of GaAs/film and film/substrate conductance.

From Fig. 5.6, we can observe the trend of thermal boundary conductance crossover. The high group velocity material AlAs would have lower TBC at low temperature, but

higher TBC at higher temperature. Among different phonon modes, the transverse mode play more important role for TBC[149]. The transverse mode sound velocity of AlAs and GaAs in [100] direction are 3960 and 3340 m/s, respectively[157]. AlAs has higher group velocity than the $Al_{0.84}Ga_{0.16}As$ and $Al_{0.72}Ga_{0.28}As$, thus the high temperature region TBC of the AlAs/GaAs film would be highest as shown in Fig. 5.6. When the temperature decreases, decreasing slope of AlAs/GaAs film would be larger than the other two films due to AlAs's relatively high group velocity. We don't reach the crossover temperature yet since our cryostat could not achieve low enough temperature, such as 10 K. (We only reached stable measurements at a cryostat stage temperature of 33 K. Considering the self-heating, the sample's actual temperature is around 40 K) However, the trend toward the crossover is clear for all three of them. In addition, at lower temperature, the crossover trend would be stronger than we observed at higher temperature region. As it is shown in Fig. 5.1, for Al/sapphire interface with higher group velocity, it decreases much faster than other lower group velocity interfaces at low temperature. Thus, in our case, we believe the decreasing rate TBC of AlAs film at lower temperature would be faster than other film and there would be a crossover at around 10 K.

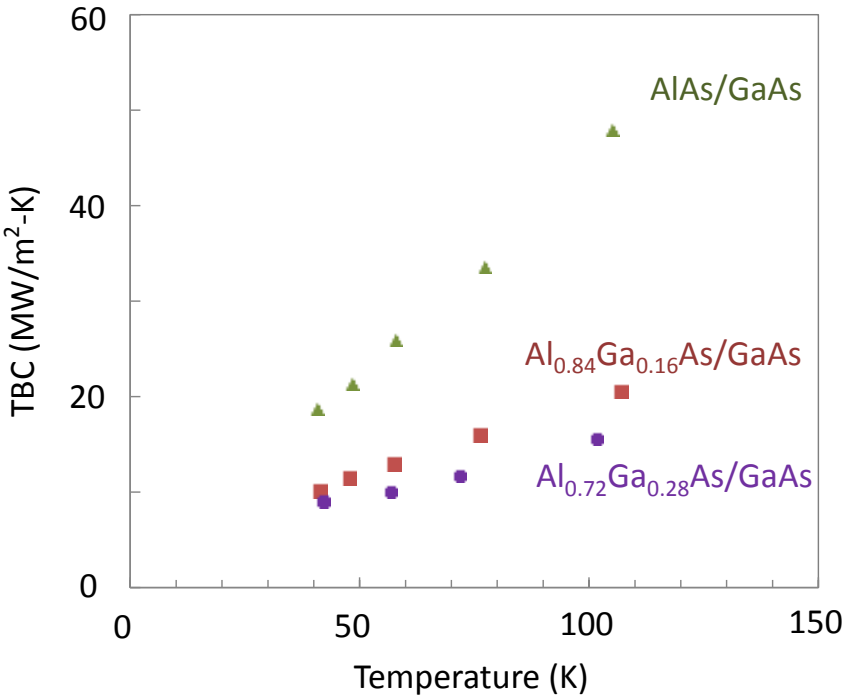


**Figure 5.6 Temperature dependence of total thermal boundary conductance for AsAs, $Al_{0.84}Ga_{0.16}As$, and $Al_{0.72}Ga_{0.28}As$ film.**

The other conclusion is the limited effect of alloy composition. Comparing the film of $Al_{0.84}Ga_{0.16}As$ and $Al_{0.72}Ga_{0.28}As$ in Fig. 5.6, even though the Ga concentration of $Al_{0.72}Ga_{0.28}As$ is almost doubled, its effect on the TBC is very limited. This is because change composition Ga from 16% to 28% only make limited change to group velocity.

## 5.5 Conclusion

We observed the thermal boundary conductance crossover trend at the AlAs/GaAs and AlGaAs/GaAs interfaces. The crossover temperature is lower than 40 K. The measurement system is verified by comparing the GaAs substrate thermal conductivity with literature. For the semiconductor alloy, it is found that the alloy effect is limited for the $Al_{0.84}Ga_{0.16}As$ and $Al_{0.72}Ga_{0.28}As$ system.

# Chapter 6 Summary and Future Work

## 6.1 Summary

This dissertation has made contributions toward better understanding of the nanoscale heat transfer in both theory and experiment. The major contributions of this work are summarized below:

Chapter 2 established a model for the effective thermal conductivity of polycrystalline materials made of randomly oriented $PbTe/Sb_2Te_3$ superlattices. The Boltzmann transport equation is used to evaluate the in plane and cross plane thermal conductivity. The gray model is first established and compared with literature method. By breaking the dispersion into small frequency bands and treating each band using gray model, the effective thermal conductivity in both in-plane and cross-plane can be obtained in the non-gray regime (phonon with different vibrational frequency would be considered.) The model has been used to investigate effects of thickness of superlattice period, specularity of the interface, and temperature. The results show the in-plane thermal conductivity is more influential than the cross-plane thermal conductivity. The modeling results are also compared with temperature dependent experimental measurements by our collaborators for superlattice period between 287 nm to 1590 nm. The temperature range is between 300 K to 500 K. The results also suggest with the increasing of annealing temperature, the surface turns to be more smooth and the specularity would be higher.

Chapter 3 dealt with thermal transport in the length scale. It gives a rigorous and systematic investigation of thermal conductivity accumulation function and mean free path spectrum of bulk materials. The changing of perspective from phonon vibrational frequency to phonon mean free path gave a more intuitive view of which phonons are important for heat conduction. This chapter also discussed how the heat conduction is affected by the boundary scattering, which is usually introduced by the size effect. Then, using the size dependent apparent thermal conductivity, it is possible to obtain the phonon accumulation function.

In Chapter 3 we also provide a general integral transform to obtain the effective thermal conductivity. In this integral transform, one input is the thermal conductivity per MFP (or accumulation function) which is only related the bulk properties; the other input is the boundary scattering term, which is related to the geometry, surface roughness *etc*.

Chapter 4 dealt with thermal transport in the time domain, especially at high heating frequency regime. We investigate the apparent thermal conductivity using the Boltzmann transport equation and obtain an analytical solution under gray assumption. Then, we extend the gray solution to non-gray regime using the similar method in Chapter 2. With this solution, we establish a framework for the experimental data analysis which covers both the diffusive and ballistic transport regime. Traditionally, all the thermal conductivity measurement data analysis uses the Fourier's law. However, at

high heating frequency in the ballistic regime, the Fourier law would not work anymore. This work provides a tool which can be used for data analysis in the ballistic regime. In addition, this work also discussed the difference between accumulation function with respect to mean free time and mean free path. We did a virtual experiment which showed that the perspective of mean free time is more suitable than mean free path to describe the distribution of phonons.

Chapter 5 investigated the thermal transport at the cryogenic low temperature. At high temperature, the larger group velocity materials tends to have high thermal conductivity and thermal conductance tends to be high. However, when the temperature decreases, the larger group velocity materials have lower thermal conductivity, which is opposite to the high temperature phenomenon. Its trend is verified by the experiment. The thermal contact resistance crossover is measured and discussed.

## 6.2 Future Work

In this section, this dissertation listed several possible research directions which may be worthy for future work.

(A) BTE solution considering the transducer layer
In this dissertation, the data analysis scheme in Chapter 4 does not include the transducer layer for the pump probe method. This layer is required for effective transfer of light to heat as the heating source. In addition, for metals such as Au or Al, their reflectivities are well studied and are easy for calibration. In this work, considering the goal of explaining the heating frequency dependent thermal conductivity and simplicity, we didn't include the transducer layer. In practice, this layer is necessary to be included.

In the future, more comprehensive models need to include this thin metal layer. Since the electron relaxation time of metal is much shorter than sample phonon relaxation time, the process in metal transducer layer can be treated as by the lumped model. The transfer matrix in the transducer layer can be obtained. Thus, combining it with the matrix of the sample, the practical BTE solution can be obtained.

(B) BTE solution with both the size and time confinement
This work discussed size (Chapter 3) and time confinement (Chapter 4), separately. In practical measurement using pump probe method, there are both confinement from modulation frequency and laser beam size. Developing the BTE based theory on both the size and time confinement are also needed.

(C) Mean free time accumulation function measurement
The mean free path accumulation function measurement has attracted great attention. As discussed in Chapter 4, the accumulation function with respect to mean free path and time are different. The later has no experimental investigation yet. Further investigation on the time domain would be important in the future. The experimental comparison of both accumulations would be interesting.

(D) 3 omega measurement at cryogenic temperature

At cryogenic temperature, the temperature coefficient of resistance (TCR) become small even approaching zero, which fails the slope method of traditional 3ω method. One method we already used in Chapter 5 to deal with this difficulty is using other fitting method to numerically obtain the TCR, such as the Bloch–Grüneisen formula for metal[154], which can be more accurate to include different types of scattering mechanisms, not only the phonon-electron Umklapp scattering at high temperature. Another method is to use heater line material with larger TCR at low temperature[158]. Some examples can be $ZrN_x$, Si doped with Nb, and doped Ge[158]. We can also use the Kondo effect of magnetic impurity scattering. The materials can be chosen as Rh-Fe alloy, which has observable but negative $dR/dT$. The selection of a appropriate TCR material is important at cryogenic temperature measurement.

# References


1. Lee, R., The Outlook for Population Growth. *Science*. **333**(6042): p. 569-573 (2011).
2. Chu, S. and A. Majumdar, Opportunities and challenges for a sustainable energy future. *Nature*. **488**(7411): p. 294-303 (2012).
3. Majumdar, A., Thermoelectric devices: Helping chips to keep their cool. *Nat Nano*. **4**(4): p. 214-215 (2009).
4. Chen, G., Nanoscale Energy Transport and Conversion. 2005, Oxford: Oxford University Press. p. 245.
5. Hicks, L.D. and M.S. Dresselhaus, Effect of quantum-well structures on the thermoelectric figure of merit. *Physical Review B*. **47**(19): p. 12727 (1993).
6. Hicks, L.D. and M.S. Dresselhaus, Thermoelectric figure of merit of a one-dimensional conductor. *Physical Review B*. **47**(24): p. 16631 (1993).
7. Hicks, L.D., T.C. Harman, X. Sun, and M.S. Dresselhaus, Experimental study of the effect of quantum-well structures on the thermoelectric figure of merit. *Physical Review B*. **53**(16): p. R10493 (1996).
8. Venkatasubramanian, R., E. Siivola, T. Colpitts, and B. O'Quinn, Thin-film thermoelectric devices with high room-temperature figures of merit. *Nature*. **413**(6856): p. 597-602 (2001).
9. Kim, W., J. Zide, A. Gossard, D. Klenov, S. Stemmer, A. Shakouri, and A. Majumdar, Thermal Conductivity Reduction and Thermoelectric Figure of Merit Increase by Embedding Nanoparticles in Crystalline Semiconductors. *Physical Review Letters*. **96**(4): p. 045901 (2006).
10. Li, D., Y. Wu, P. Kim, L. Shi, P. Yang, and A. Majumdar, Thermal conductivity of individual silicon nanowires. *Applied Physics Letters*. **83**(14): p. 2934-2936 (2003).
11. Li, D., Y. Wu, R. Fan, P. Yang, and A. Majumdar, Thermal conductivity of Si/SiGe superlattice nanowires. *Applied Physics Letters*. **83**(15): p. 3186-3188 (2003).
12. Hochbaum, A.I., R. Chen, R.D. Delgado, W. Liang, E.C. Garnett, M. Najarian, A. Majumdar, and P. Yang, Enhanced thermoelectric performance of rough silicon nanowires. *Nature*. **451**(7175): p. 163-167 (2008).
13. Boukai, A.I., Y. Bunimovich, J. Tahir-Kheli, J.-K. Yu, W.A. Goddard Iii, and J.R. Heath, Silicon nanowires as efficient thermoelectric materials. *Nature*. **451**(7175): p. 168-171 (2008).
14. Hippalgaonkar, K., B. Huang, R. Chen, K. Sawyer, P. Ercius, and A. Majumdar, Fabrication of Microdevices with Integrated Nanowires for Investigating Low-Dimensional Phonon Transport. *Nano Letters*. **10**(11): p. 4341-4348 (2010).
15. Lim, J., K. Hippalgaonkar, S.C. Andrews, A. Majumdar, and P. Yang, Quantifying Surface Roughness Effects on Phonon Transport in Silicon Nanowires. *Nano Letters*. **12**(5): p. 2475-2482 (2012).
16. Poudel, B., Q. Hao, Y. Ma, Y. Lan, A. Minnich, B. Yu, X. Yan, D. Wang, A. Muto, D. Vashaee, X. Chen, J. Liu, M.S. Dresselhaus, G. Chen, and Z. Ren, High-

Thermoelectric Performance of Nanostructured Bismuth Antimony Telluride Bulk Alloys. *Science*. **320**(5876): p. 634-638 (2008).
17. Zhao, L.-D., S.-H. Lo, Y. Zhang, H. Sun, G. Tan, C. Uher, C. Wolverton, V.P. Dravid, and M.G. Kanatzidis, Ultralow thermal conductivity and high thermoelectric figure of merit in SnSe crystals. *Nature*. **508**(7496): p. 373-377 (2014).
18. Dames, C. and G. Chen, Thermal Conductivity of Nanostructured Thermoelectric Materials, in *Thermoelectrics Handbook, Macro to Nano*, D.M. Rowe, Editor. 2006, Taylor & Francis: New York.
19. Siemens, M.E., Q. Li, R. Yang, K.A. Nelson, E.H. Anderson, M.M. Murnane, and H.C. Kapteyn, Quasi-ballistic thermal transport from nanoscale interfaces observed using ultrafast coherent soft X-ray beams. *Nat Mater*. **9**(1): p. 26-30 (2010).
20. Minnich, A.J., J.A. Johnson, A.J. Schmidt, K. Esfarjani, M.S. Dresselhaus, K.A. Nelson, and G. Chen, Thermal Conductivity Spectroscopy Technique to Measure Phonon Mean Free Paths. *Physical Review Letters*. **107**(9): p. 095901 (2011).
21. Cahill, D.G., Analysis of heat flow in layered structures for time-domain thermoreflectance. *Review of Scientific Instruments*. **75**(12): p. 5119-5122 (2004).
22. Johnson, J.A., A.A. Maznev, J. Cuffe, J.K. Eliason, A.J. Minnich, T. Kehoe, C.M.S. Torres, G. Chen, and K.A. Nelson, Direct Measurement of Room-Temperature Nondiffusive Thermal Transport Over Micron Distances in a Silicon Membrane. *Physical Review Letters*. **110**(2): p. 025901 (2013).
23. Yang, F., T. Ikeda, G.J. Snyder, and C. Dames, Effective thermal conductivity of polycrystalline materials with randomly oriented superlattice grains. *Journal of Applied Physics*. **108**(3): p. 034310-12 (2010).
24. Shum, C.K., F. Busaba, and C. Jacobi, IBM zEC12: The third-generation high-frequency mainframe microprocessor. *IEEE Micro*. **33**(2): p. 0038-47 (2013).
25. Koh, Y.K. and D.G. Cahill, Frequency dependence of the thermal conductivity of semiconductor alloys. *Physical Review B*. **76**(7): p. 075207 (2007).
26. Regner, K.T., D.P. Sellan, Z. Su, C.H. Amon, A.J.H. McGaughey, and J.A. Malen, Broadband phonon mean free path contributions to thermal conductivity measured using frequency domain thermoreflectance. *Nat Commun*. **4**: p. 1640 (2013).
27. Schmidt, A.J., X. Chen, and G. Chen, Pulse accumulation, radial heat conduction, and anisotropic thermal conductivity in pump-probe transient thermoreflectance. *Rev. Sci. Instrum.* **79**(11): p. 114902 (2008).
28. Malen, J.A., K. Baheti, T. Tong, Y. Zhao, J.A. Hudgings, and A. Majumdar, Optical Measurement of Thermal Conductivity Using Fiber Aligned Frequency Domain Thermoreflectance. *Journal of Heat Transfer*. **133**(8): p. 081601-7 (2011).
29. Snyder, G.J. and E.S. Toberer, Complex thermoelectric materials. *Nat Mater*. **7**(2): p. 105-114 (2008).
30. Kittel, C., Introduction to Solid State Physics. 7th ed. 1996: Wiley. 160.
31. Chen, G., Size and Interface Effects on Thermal Conductivity of Superlattices and Periodic Thin-Film Structures. *Journal of Heat Transfer*. **119**(2): p. 220-229 (1997).

32. Chen, G., Thermal conductivity and ballistic-phonon transport in the cross-plane direction of superlattices. *Physical Review B*. **57**(23): p. 14958 (1998).
33. Harman, T.C., P.J. Taylor, M.P. Walsh, and B.E. LaForge, Quantum Dot Superlattice Thermoelectric Materials and Devices. *Science*. **297**(5590): p. 2229-2232 (2002).
34. Chowdhury, I., R. Prasher, K. Lofgreen, G. Chrysler, S. Narasimhan, R. Mahajan, D. Koester, R. Alley, and R. Venkatasubramanian, On-chip cooling by superlattice-based thin-film thermoelectrics. *Nat Nano*. **4**(4): p. 235-238 (2009).
35. Medlin, D.L. and G.J. Snyder, Interfaces in bulk thermoelectric materials: A review for Current Opinion in Colloid and Interface Science. *Current Opinion in Colloid & Interface Science*. **14**(4): p. 226-235 (2009).
36. Ikeda, T., L.A. Collins, V.A. Ravi, F.S. Gascoin, S.M. Haile, and G.J. Snyder, Self-Assembled Nanometer Lamellae of Thermoelectric PbTe and Sb2Te3 with Epitaxy-like Interfaces. *Chemistry of Materials*. **19**(4): p. 763 (2007).
37. Lan, Y., A.J. Minnich, G. Chen, and Z. Ren, Enhancement of Thermoelectric Figure-of-Merit by a Bulk Nanostructuring Approach. *Advanced Functional Materials*. **20**(3): p. 357-376 (2010).
38. Hsu, K.F., S. Loo, F. Guo, W. Chen, J.S. Dyck, C. Uher, T. Hogan, E.K. Polychroniadis, and M.G. Kanatzidis, Cubic AgPbmSbTe2+m: Bulk thermoelectric materials with high figure of merit. *Science*. **303**(5659): p. 818-821 (2004).
39. Liu, C.-K., C.-K. Yu, H.-C. Chien, S.-L. Kuo, C.-Y. Hsu, M.-J. Dai, G.-L. Luo, S.-C. Huang, and M.-J. Huang, Thermal conductivity of Si/SiGe superlattice films. *Journal of Applied Physics*. **104**(11): p. 114301 (2008).
40. Mityushov, E.A., R.A. Adamesku, and P.V. Gel'd, Relation between kinetic properties of single crystals and of oriented polycrystalline materials. *Journal of Engineering Physics and Thermophysics*. **47**(3): p. 1052-1056 (1984).
41. Voigt, W., Lehrbuch der Krystallphysik. 1911, Berlin, Germany: Teubener.
42. Adams, B.L. and T. Olson, The mesostructure--properties linkage in polycrystals. *Progress in Materials Science*. **43**(1): p. 1-87 (1998).
43. Schulgasser, K., Bounds on the conductivity of statistically isotropic polycrystals. *Journal of Physics C: Solid State Physics*. **10**(3) (1977).
44. Press, W.H., S.A. Teukolsky, W.T. Vetterling, and B.P. Flannery, Numerical Recipes 3rd Edition: The Art of Scientific Computing 2007: Cambridge University Press. 986.
45. Dames, C. and G. Chen, Theoretical phonon thermal conductivity of Si/Ge superlattice nanowires. *Journal of Applied Physics*. **95**(2): p. 682-693 (2004).
46. Mingo, N., Calculation of Si nanowire thermal conductivity using complete phonon dispersion relations. *Physical Review B*. **68**(11): p. 113308 (2003).
47. Abeles, B., Lattice Thermal Conductivity of Disordered Semiconductor Alloys at High Temperatures. *Physical Review*. **131**(5): p. 1906 (1963).
48. Han, Y.-J., Intrinsic thermal-resistive process of crystals: Umklapp processes at low and high temperatures. *Physical Review B*. **54**(13): p. 8977 (1996).
49. Dyck, J.S., W. Chen, C. Uher, C. Drasar, and P. Lostak, Heat transport in Sb2-xVxTe3 single crystals. *Physical Review B*. **66**(12): p. 125206 (2002).
50. Madelung, O., Semiconductors: Data Handbook. 3rd Edition ed. 2004: Springer.

51. Greig, D., Thermoelectricity and Thermal Conductivity in the Lead Sulfide Group of Semiconductors. *Physical Review*. **120**(2): p. 358 (1960).
52. Devyatkova, E., I. Smirnov, and F.T. Tela, *Soviet Phys. Solid State*. **3**: p. 1675 (1962).
53. Goldsmid, H.J., The Thermal Conductivity of Bismuth Telluride. *Proceedings of the Physical Society. Section B*. **69**(2): p. 203 (1956).
54. Caillat, T., M. Carle, P. Pierrat, H. Scherrer, and S. Scherrer, Thermoelectric properties of (BixSb1-x)2Te3 single crystal solid solutions grown by the T.H.M. method. *Journal of Physics and Chemistry of Solids*. **53**(8): p. 1121-1129 (1992).
55. Scherrer, H. and S. Scherrer, Bismuth Telluride, Antimony Telluride, and Their Solid Solutions, in *CRC Handbook of Thermoelectrics*, D.M. Rowe, Editor. 1995, CRC Press.
56. Ziman, J.M., Electrons and Phonons: The Theory of Transport Phenomena in Solids. 1960: Oxford. 459.
57. Zhang, Z., Nano/Microscale Heat Transfer. 2007: McGraw-Hill. 274.
58. Lee, S.M., D.G. Cahill, and R. Venkatasubramanian, Thermal conductivity of Si--Ge superlattices. *Applied Physics Letters*. **70**(22): p. 2957-2959 (1997).
59. Dames, C., M.S. Dresselhaus, and G. Chen, Phonon Thermal Conductivity of Superlattice Nanowires for Thermoelectric Applications, in *Thermoelectric Materials 2003 Research and Applications*, G.S. Nolas, Editor. 2004, Materials Research Society: San Francisco. p. S1.2.
60. Majumdar, A., Microscale Heat Conduction in Dielectric Thin Films. *Journal of Heat Transfer*. **115**(1): p. 7-16 (1993).
61. Ikeda, T., V.A. Ravi, and G.J. Snyder, Evaluation of true interlamellar spacing from microstructural observations. *Journal of Materials Research*. **23**(9): p. 2538-2544 (2008).
62. Ikeda, T., E.S. Toberer, A.R. Vilupaur, S.M. Haile, and G.J. Snyder, Lattice thermal conductivity of self-assembled PbTe-Sb2Te3 composites with nanometer lamellae, in *26th International Conference on Thermoelectrics*, I.-H. Kim, Editor. 2007, IEEE: Jeju Korea. p. 1-4.
63. Nolas, G.S., Thermal Conducitivity of Semiconductors, in *Thermal Conductivity: Theory, Properties, and Applications*, T.M. Tritt, Editor. 2004, Kluwer Academic: New York. p. 110.
64. Simkin, M.V. and G.D. Mahan, Minimum Thermal Conductivity of Superlattices. *Physical Review Letters*. **84**(5): p. 927 (2000).
65. Yang, B. and G. Chen, Partially coherent phonon heat conduction in superlattices. *Physical Review B*. **67**(19): p. 195311 (2003).
66. Akgöz, Y.C., G.A. Saunders, and Z. Sümengen, Elastic wave propagation in Bi10.60Sb0.40Te3 and Bi2Te3. *Journal of Materials Science*. **7**(3): p. 279-288 (1972).
67. Yang, F. and C. Dames, Mean free path spectra as a tool to understand thermal conductivity in bulk and nanostructures. *Physical Review B*. **87**(3): p. 035437 (2013).
68. Asheghi, M., Y.K. Leung, S.S. Wong, and K.E. Goodson, Phonon-boundary scattering in thin silicon layers. *Applied Physics Letters*. **71**(13): p. 1798-1800 (1997).

69. Liu, W. and M. Asheghi, Thermal Conductivity Measurements of Ultra-Thin Single Crystal Silicon Layers. *Journal of Heat Transfer*. **128**(1): p. 75-83 (2006).
70. Song, D. and G. Chen, Thermal conductivity of periodic microporous silicon films. *Applied Physics Letters*. **84**(5): p. 687-689 (2004).
71. Wang, Z., J.E. Alaniz, W. Jang, J.E. Garay, and C. Dames, Thermal Conductivity of Nanocrystalline Silicon: Importance of Grain Size and Frequency-Dependent Mean Free Paths. *Nano Letters*. **11**(6): p. 2206 (2011).
72. Minnich, A.J., M.S. Dresselhaus, Z.F. Ren, and G. Chen, Bulk nanostructured thermoelectric materials: current research and future prospects. *Energy & Environmental Science*. **2**(5): p. 466-479 (2009).
73. Linan, J., W. Man, and Z. Yitshak, Micromachined polycrystalline thin film temperature sensors. *Measurement Science and Technology*. **10**(8): p. 653 (1999).
74. Cui, Y., Q. Wei, H. Park, and C.M. Lieber, Nanowire Nanosensors for Highly Sensitive and Selective Detection of Biological and Chemical Species. *Science*. **293**(5533): p. 1289-1292 (2001).
75. Schelling, P.K., L. Shi, and K.E. Goodson, Managing heat for electronics. *Materials Today*. **8**(6): p. 30-35 (2005).
76. Huang, M.H., S. Mao, H. Feick, H. Yan, Y. Wu, H. Kind, E. Weber, R. Russo, and P. Yang, Room-Temperature Ultraviolet Nanowire Nanolasers. *Science*. **292**(5523): p. 1897-1899 (2001).
77. Broido, D.A., M. Malorny, G. Birner, M. Natalio, and D.A. Stewart, Intrinsic lattice thermal conductivity of semiconductors from first principles. *Applied Physics Letters*. **91**(23): p. 231922 (2007).
78. Henry, A.S. and G. Chen, Spectral Phonon Transport Properties of Silicon Based on Molecular Dynamics Simulations and Lattice Dynamics. *Journal of Computational and Theoretical Nanoscience*. **5**: p. 141 (2008).
79. Bera, C., N. Mingo, and S. Volz, Marked Effects of Alloying on the Thermal Conductivity of Nanoporous Materials. *Physical Review Letters*. **104**(11): p. 115502 (2010).
80. Sellan, D.P., E.S. Landry, J.E. Turney, A.J.H. McGaughey, and C.H. Amon, Size effects in molecular dynamics thermal conductivity predictions. *Physical Review B*. **81**(21): p. 214305 (2010).
81. Garg, J., N. Bonini, B. Kozinsky, and N. Marzari, Role of Disorder and Anharmonicity in the Thermal Conductivity of Silicon-Germanium Alloys: A First-Principles Study. *Physical Review Letters*. **106**(4): p. 045901 (2011).
82. Esfarjani, K., G. Chen, and H.T. Stokes, Heat transport in silicon from first-principles calculations. *Physical Review B*. **84**(8): p. 085204 (2011).
83. Li, W., N. Mingo, L. Lindsay, D.A. Broido, D.A. Stewart, and N.A. Katcho, Thermal conductivity of diamond nanowires from first principles. *Physical Review B*. **85**(19): p. 195436 (2012).
84. Minnich, A.J., Determining Phonon Mean Free Paths from Observations of Quasiballistic Thermal Transport. *Physical Review Letters*. **109**(20): p. 205901 (2012).
85. Callaway, J., Model for Lattice Thermal Conductivity at Low Temperatures. *Physical Review*. **113**(4): p. 1046 (1959).

86. Holland, M.G., Analysis of Lattice Thermal Conductivity. *Physical Review*. **132**(6): p. 2461 (1963).
87. Hamilton, R.A.H. and J.E. Parrott, Variational Calculation of the Thermal Conductivity of Germanium. *Physical Review*. **178**(3): p. 1284-1292 (1969).
88. Asen-Palmer, M., K. Bartkowski, E. Gmelin, M. Cardona, A.P. Zhernov, A.V. Inyushkin, A. Taldenkov, V.I. Ozhogin, K.M. Itoh, and E.E. Haller, Thermal conductivity of germanium crystals with different isotopic compositions. *Physical Review B*. **56**(15): p. 9431 (1997).
89. Chung, J.D., A.J.H. McGaughey, and M. Kaviany, Role of Phonon Dispersion in Lattice Thermal Conductivity Modeling. *Journal of Heat Transfer*. **126**(3): p. 376-380 (2004).
90. Dames, C., A broad range of phonon mean free paths is important for heat conduction, in *Micro/Nanoscale Heat Transfer International Conference*. 2008, unpublished work: National Cheng Kung University, Taiwan.
91. Mingo, N. and L. Yang, Phonon transport in nanowires coated with an amorphous material: An atomistic Green's function approach. *Physical Review B*. **68**(24): p. 245406 (2003).
92. Prasher, R., T. Tong, and A. Majumdar, Approximate Analytical Models for Phonon Specific Heat and Ballistic Thermal Conductance of Nanowires. *Nano Letters*. **8**(1): p. 99-103 (2007).
93. Mingo, N., L. Yang, D. Li, and A. Majumdar, Predicting the Thermal Conductivity of Si and Ge Nanowires. *Nano Letters*. **3**(12): p. 1713-1716 (2003).
94. Casimir, H.B.G., Note on the conduction of heat in crystals. *Physica*. **5**(6): p. 495-500 (1938).
95. McCurdy, A.K., H.J. Maris, and C. Elbaum, Anisotropic Heat Conduction in Cubic Crystals in the Boundary Scattering Regime. *Physical Review B*. **2**(10): p. 4077-4083 (1970).
96. Dingle, R.B., THE ELECTRICAL CONDUCTIVITY OF THIN WIRES. *Proceedings of the Royal Society of London Series a-Mathematical and Physical Sciences*. **201**(1067): p. 545-560 (1950).
97. Fuchs, K., The conductivity of thin metallic films according to the electron theory of metals. *Mathematical Proceedings of the Cambridge Philosophical Society*. **34**(01): p. 100-108 (1938).
98. Sondheimer, E.H., The mean free path of electrons in metals. *Advances in Physics*. **1**(1): p. 1 - 42 (1952).
99. Flik, M.I. and C.L. Tien, Size Effect on the Thermal Conductivity of High-$T_c$ Thin-Film Superconductors. *Journal of Heat Transfer*. **112**(4): p. 872-881 (1990).
100. Richardson, R.A. and F. Nori, Transport and boundary scattering in confined geometries: Analytical results. *Physical Review B*. **48**(20): p. 15209 (1993).
101. Bux, S.K., R.G. Blair, P.K. Gogna, H. Lee, G. Chen, M.S. Dresselhaus, R.B. Kaner, and J.-P. Fleurial, Nanostructured Bulk Silicon as an Effective Thermoelectric Material. *Advanced Functional Materials*. **19**(15): p. 2445-2452 (2009).
102. Ziman, J.M., Electrons and Phonons: The Theory of Transport Phenomena in Solids. 1960, Oxford: Oxford University Press. 463.

103. Heron, J.S., T. Fournier, N. Mingo, and O. Bourgeois, Mesoscopic Size Effects on the Thermal Conductance of Silicon Nanowire. *Nano Letters*. **9**(5): p. 1861-1865 (2009).
104. Morelli, D.T., J.P. Heremans, and G.A. Slack, Estimation of the isotope effect on the lattice thermal conductivity of group IV and group III-V semiconductors. *Physical Review B*. **66**(19): p. 195304 (2002).
105. Glassbrenner, C.J. and G.A. Slack, Thermal Conductivity of Silicon and Germanium from 3K to the Melting Point. *Physical Review*. **134**(4A): p. A1058 (1964).
106. Esfarjani, K., *Personal Communication, for 300 K data using the same method as Ref. 20*. (2012).
107. Ju, Y.S. and K.E. Goodson, Phonon scattering in silicon films with thickness of order 100 nm. *Applied Physics Letters*. **74**(20): p. 3005-3007 (1999).
108. Asheghi, M., M.N. Touzelbaev, K.E. Goodson, Y.K. Leung, and S.S. Wong, Temperature-Dependent Thermal Conductivity of Single-Crystal Silicon Layers in SOI Substrates. *Journal of Heat Transfer*. **120**(1): p. 30-36 (1998).
109. Slack, G.A., Effect of Isotopes on Low-Temperature Thermal Conductivity. *Physical Review*. **105**(3): p. 829 (1957).
110. Slack, G.A. and S. Galginaitis, Thermal Conductivity and Phonon Scattering by Magnetic Impurities in CdTe. *Physical Review*. **133**(1A): p. A253 (1964).
111. Cahill, D.G., *Personal Communication, Mar,13* (2012).
112. Freedman, J.P. and J.A. Malen, Thermal Transport in Complex Semiconductor Nanostructures. *Personal Communication, Oct,12* (2012).
113. Daly, B.C., K. Kang, Y. Wang, and D.G. Cahill, Picosecond ultrasonic measurements of attenuation of longitudinal acoustic phonons in silicon. *Physical Review B*. **80**(17): p. 174112 (2009).
114. Volz, S.G., Thermal Insulating Behavior in Crystals at High Frequencies. *Physical Review Letters*. **87**(7): p. 074301 (2001).
115. Ezzahri, Y. and K. Joulain, Dynamical thermal conductivity of bulk semiconductor crystals. *Journal of Applied Physics*. **112**(8): p. 083515-14 (2012).
116. Hamad-Schifferli, K., J.J. Schwartz, A.T. Santos, S. Zhang, and J.M. Jacobson, Remote electronic control of DNA hybridization through inductive coupling to an attached metal nanocrystal antenna. *Nature*. **415**(6868): p. 152-155 (2002).
117. Pernot, G., H. Michel, B. Vermeersch, P. Burke, H. Lu, J.-M. Rampnoux, S. Dilhaire, Y. Ezzahri, A. Gossard, and A. Shakouri, Frequency-Dependent Thermal Conductivity in Time Domain Thermoreflectance Analysis of Thin Films. *MRS Online Proceedings*. **1347** (2011).
118. Minnich, A.J., G. Chen, S. Mansoor, and B.S. Yilbas, Quasiballistic heat transfer studied using the frequency-dependent Boltzmann transport equation. *Physical Review B*. **84**(23): p. 235207 (2011).
119. Minnich, A., Modeling the thermoelectric properties of bulk and nanocomposite thermoelectric materials, in *Mechanical Engineering*. 2011, MIT.
120. Chen, G., Nonlocal and Nonequilibrium Heat Conduction in the Vicinity of Nanoparticles. *Journal of Heat Transfer*. **118**(3): p. 539-545 (1996).

121. Wilson, R.B., J.P. Feser, G.T. Hohensee, and D.G. Cahill, Two-channel model for nonequilibrium thermal transport in pump-probe experiments. *Physical Review B*. **88**(14): p. 144305 (2013).
122. Wilson, R.B. and D.G. Cahill, Anisotropic failure of Fourier theory in time-domain thermoreflectance experiments. *Nat Commun*. **5** (2014).
123. Maznev, A.A., J.A. Johnson, and K.A. Nelson, Onset of nondiffusive phonon transport in transient thermal grating decay. *Physical Review B*. **84**(19): p. 195206 (2011).
124. Collins, K.C., A.A. Maznev, Z. Tian, K. Esfarjani, K.A. Nelson, and G. Chen, Non-diffusive relaxation of a transient thermal grating analyzed with the Boltzmann transport equation. *Journal of Applied Physics*. **114**(10): p. - (2013).
125. Hua, C. and A.J. Minnich, Transport regimes in quasiballistic heat conduction. *Physical Review B*. **89**(9): p. 094302 (2014).
126. Regner, K.T., A.J.H. McGaughey, and J.A. Malen, Analytical interpretation of nondiffusive phonon transport in thermoreflectance thermal conductivity measurements. *Physical Review B*. **90**(6): p. 064302 (2014).
127. Escobar, R.A., S.S. Ghai, M.S. Jhon, and C.H. Amon, Multi-length and time scale thermal transport using the lattice Boltzmann method with application to electronics cooling. *International Journal of Heat and Mass Transfer*. **49**(1-2): p. 97-107 (2006).
128. Bergman, T., A. Lavine, F.P. Incropera, and D.P. DeWitt, Fundamentals of heat and mass transfer. 2011: Wiely. 327.
129. Dismukes, J.P., L. Ekstrom, E.F. Steigmeier, I. Kudman, and D.S. Beers, Thermal and Electrical Properties of Heavily Doped Ge-Si Alloys up to 1300K. *Journal of Applied Physics*. **35**(10): p. 2899-2907 (1964).
130. Chen, G., Nanoscale Energy Transport and Conversion. 2005, Oxford: Oxford University Press. 241.
131. Hao, Q., G. Chen, and M.-S. Jeng, Frequency-dependent Monte Carlo simulations of phonon transport in two-dimensional porous silicon with aligned pores. *Journal of Applied Physics*. **106**(11): p. 114321-10 (2009).
132. Joshi, A.A. and A. Majumdar, Transient ballistic and diffusive phonon heat transport in thin films. *Journal of Applied Physics*. **74**(1): p. 31-39 (1993).
133. Murthy, J.Y., S.V.J. Narumanchi, J.A. Pascual-Gutierrez, T. Wang, C. Ni, and S.R. Mathur, Review of Multi-Scale Simulation in Sub-Micron Heat Transfer. *International Journal for Multiscale Computational Engineering*. **3**(1): p. 5-32 (2005).
134. Modest, M.F., Radiative Heat Transfer. 2003. p456.
135. Greenberg, M., Advanced Engineering Mathematics. 2nd ed. 1998: Prentice Hall. 981.
136. Cahill, D.G. and R.O. Pohl, Lattice Vibrations and Heat Transport in Crystals and Glasses. *Annual Review of Physical Chemistry*. **39**(1): p. 93-121 (1988).
137. Joseph, D.D. and L. Preziosi, Heat waves. *Reviews of Modern Physics*. **61**(1): p. 41-73 (1989).
138. Lifshitz, E., Radiation of sound in helium II. *Journal of Physics-Ussr*. **8**(1-6): p. 110-114 (1944).

139. Landau, L., The theory of superfluidity of helium II. *Journal of Physics-Ussr*. **5**(1-6): p. 71-90 (1941).
140. Ward, J.C. and J. Wilks, The velocity of second sound in liquid helium near the absolute zero. *Philosophical Magazine Series 7*. **42**(326): p. 314-316 (1951).
141. Ward, J.C. and J. Wilks, III. Second sound and the thermo-mechanical effect at very low temperatures. *Philosophical Magazine Series 7*. **43**(336): p. 48-50 (1952).
142. Dingle, R.B., Derivation of the Velocity of Second Sound from Maxwell's Equation of Transfer. *Proceedings of the Physical Society. Section A*. **65**(5): p. 374 (1952).
143. Ackerman, C.C., B. Bertman, H.A. Fairbank, and R.A. Guyer, Second Sound in Solid Helium. *Physical Review Letters*. **16**(18): p. 789-791 (1966).
144. Jackson, H.E. and C.T. Walker, Thermal Conductivity, Second Sound, and Phonon-Phonon Interactions in NaF. *Physical Review B*. **3**(4): p. 1428-1439 (1971).
145. Rogers, S.J., Transport of Heat and Approach to Second Sound in Some Isotopically Pure Alkali-Halide Crystals. *Physical Review B*. **3**(4): p. 1440-1457 (1971).
146. Koreeda, A., R. Takano, and S. Saikan, Second Sound in $SrTiO_3$. *Physical Review Letters*. **99**(26): p. 265502 (2007).
147. Toberer, E.S., L.L. Baranowski, and C. Dames, Advances in Thermal Conductivity. *Annual Review of Materials Research*. **42**(1): p. 179-209 (2012).
148. Stoner, R.J. and H.J. Maris, Kapitza conductance and heat flow between solids at temperatures from 50 to 300 K. *Physical Review B*. **48**(22): p. 16373 (1993).
149. Swartz, E.T. and R.O. Pohl, Thermal boundary resistance. *Reviews of Modern Physics*. **61**(3): p. 605 (1989).
150. Cahill, D.G., M. Katiyar, and J.R. Abelson, Thermal conductivity of a-Si:H thin films. *Physical Review B*. **50**(9): p. 6077-6081 (1994).
151. Cahill, D.G., Thermal conductivity measurement from 30 to 750 K: the 3 omega method. *Review of Scientific Instruments*. **61**(2): p. 802-808 (1990).
152. Dames, C. and G. Chen, 1 omega, 2 omega, and 3 omega methods for measurements of thermal properties. *Review of Scientific Instruments*. **76**(12): p. 124902-14 (2005).
153. Pässler, R., Non-Debye heat capacity formula refined and applied to GaP, GaAs, GaSb, InP, InAs, and InSb. *AIP Advances*. **3**(8): p. - (2013).
154. Chen, Z., W. Jang, W. Bao, C.N. Lau, and C. Dames, Thermal contact resistance between graphene and silicon dioxide. *Applied Physics Letters*. **95**(16): p. 161910-3 (2009).
155. O. Madelung, U.R., M. Schulz, Gallium arsenide (GaAs), intrinsic carrier concentration, electrical and thermal conductivity, in *Landolt-Börnstein - Group III Condensed Matter, Numerical Data and Functional Relationships in Science and Technology*, O. Madelung, U. Rössler, and M. Schulz, Editors.
156. Gallium nitride (GaN), electrical and thermal conductivity, electron concentration, in *Landolt-Börnstein - Group III Condensed Matter*, O. Madelung, U. Rössler, and M. Schulz, Editors.
157. http://www.ioffe.ru/SVA/NSM/.

158. Dames, C., Measuring the thermal conductivity of thin films: 3 omega and related electrothermal methods. *Annual Review of Heat Transfer*. **16**(16): p. 7-49 (2012).